Lappeenranta-Lahti University of Technology LUT
LUT School of Energy Systems
Energy Technology
2022

BOILING INSTABILITIES IN HELICAL COIL STEAM GENERATOR

Master's Thesis

Lappeenranta–Lahti University of Technology LUT

Master's Thesis

Chowdhury, Debasish

Examiner: Professor. Dr. Juhani Hyvärinen

Supervisors: Dr. Juhani Vihavainen

Professor. Dr. Iztok Tiselj

ABSTRACT

Lappeenranta–Lahti University of Technology LUT

LUT School of Energy Systems

Energy Technology

Chowdhury Debasish

BOILING INSTABILITIES IN HELICAL COIL STEAM GENERATOR

Master's thesis

2022

93 pages, 97 figures, 19 tables, and 01 appendix

Examiner: Professor. Dr. Juhani Hyvärinen

Supervisors: Dr. Juhani Vihavainen

Professor. Dr. Iztok Tiselj

Keywords: Helical Coil, Steam Generator, Small Modular Reactor, Instabilities

Helically coiled steam generator is an essential part of current generation small modular reactors like NuScale due to its compactness and high heat transfer area. Instabilities due to boiling water inside helically coiled tubes is an important research question due to its importance for the steady-state operation of the plant. This study presents an experimental investigation of two-phase boiling instabilities inside helically coiled tubes. Four experiments were carried out with different thermal power, mass flow rate, and pressure to understand flow behaviour under different system conditions. It is found that thermal oscillation inside the tube increases with the power step and tube length while decreasing with the mass flow rate. The thermal oscillation period also increases with a higher power step. A semi-empirical correlation based on experimental data is developed. The overall heat transfer coefficient is calculated theoretically using the Chen correlation and later compared with the experimental value. Both experimental and theoretical value of the heat transfer coefficient agrees well.

TIIVISTELMÄ

ACKNOWLEDGEMENTS

Foremost I would like to express my sincere gratitude to **Dr. Juhani Hyvärinen**, **Dr. Juhani Vihavainen**, and **Dr. Iztok Tiselj** for the valuable supervision, thought-provoking guidelines and suggestions they gave me throughout the different stages of research. Thermal Hydraulics research is an immensely challenging area, and I learned various aspects of thermal-hydraulics science under their supervision during my research. I believe the knowledge and learning I gathered working under him during research work is an invaluable experience and asset in my future life.

My special thanks go to my **parents and friends** for their continuous support and inspiration which motivated me to do good work.

SYMBOLS AND ABBREVIATIONS

Roman characters

p	pressure	[bar, Pa]
$\dot{m}$	mass flow rate	[kg/s]
T	temperature	[ºC, K]
V	velocity	[m/s]
x	vapour quality	
r	tube radius	[m]
R	coil radius	[m]
d	tube diameter	[m]
D	coil diameter	[m]
H	elevation height	[m]
L	coil length	[m]
h	enthalpy	[kJ/kg]
k	thermal conductivity	[W/m.K]
f	friction factor	
q	heat transfer rate	[kW]
S	Nucleate boiling suppression factor	
F	two phase multiplier correction factor	
K	Local Loss Coefficient	
G	mass flux	[kg/m^2.s]
A	tube area	[m^2]
ΔP	pressure difference	[bar, Pa]
ΔT	Temperature difference	[ºC]

C_p	Specific Heat Capacity	[$J \cdot kg^{-1} \cdot K^{-1}$]

Greek characters

α	void fraction	
λ	dimensionless curvature	
δ	dimensionless torsion	
ρ	density	[kg/m^3]
μ	viscosity	[Pa.s]
χ_{tt}	Lockhart–Martinelli parameter	

Constants

g	gravitational acceleration	9.81 m/s

Dimensionless quantities

Re	Reynolds number
Pr	Prandtl number
N_{pch}	Phase Change number
N_{sub}	Sub Cooling number
De	Dean number

Subscripts

b	bulk (with temperature)/bundle
p	primary
s	secondary
c	curvature
i	inlet
o	outlet
l	liquid

g	gas
lg	difference between liquid and gas properties
R	reference
pch	phase change
sub	sub cooling
m	mixture
n	tube number
calc	calculation
exp	experimental
sat	saturation
T	total

Superscripts

+	Dimensionless Pressure or Flux
*	Dimensionless Number

Abbreviations

FW	Feedwater
STM	Steam
SMR	Small Modular Reactor
PWR	Pressurized Water Reactor
LUT	Lappeenranta University of Technology
MOTEL	Modular Test Loop
GCR	Gas Cooled Reactor
LMBR	Liquid Metal Breeder Reactor

THTR	Thorium High Temperature Reactor
ALMR	Advanced Liquid Metal Reactor
VVER	Water Water Energy Reactor
BWR	Boiling Water Reactor

TABLE OF CONTENTS

1 INTRODUCTION

1.1 BACKGROUND AND MOTIVATION

This chapter will give an overview of nuclear energy's present status and role in the future energy mix due to the increasing importance of clean energy generation. It is evident that all sources of clean energy should be explored to achieve the future climate goal for keeping global temperature below 1.5ºC. Due to its high energy density and carbon neutral characteristics, nuclear energy is a good proponent as a clean energy source. More and more focus is now on small-scale nuclear energy sources like small modular reactors (SMR) due to their lower capital cost and easy deployable ability in the shortest possible time. This section will cover the global energy scenario, nuclear energy's present status, importance, and core feature of SMR, followed by the scope of study and outline.

1.1.1 Global energy scenario: present status and prospects

From the early age of human history, energy played an essential role as a commodity to drive perpetual growth. Consumption and production of energy scenarios kept changing throughout history due to socio-economic factors like economic growth, climate change, government rules, cultural mindset, and technological capacity. From the early 1970s, energy markets saw significant uncertainties due to the fluctuation of fossil fuel prices. Current energy demand is predominantly met by fossil fuel (84.7% of total consumption), followed by hydroelectric (6.8%), nuclear (4.4%), and renewable (4%)(Ghasemian *et al.*, 2020). The significant demand for global energy today is driven by economic growth, in which major emerging economies and developing markets play an essential role. While Global GDP is expected to increase at 3.55% per annum (Ghasemian *et al.*, 2020) and population growth of two billion people, the energy growth in future decades will increase only by 14% (McKinsey & Company, 2022 ‘McKinsey & Company.pdf,’ no date) Net zero emission pledges made by 130 countries in 26th Conference of the Parties (COP26) COP26 countries will require USD 4 trillion investment in clean energy by 2030. (International Energy Agency, 2021). The future the energy scenario will be dominated by energy and hydrogen with in

total contribution of 32% by 2030 and 50% by 2035.(McKinsey & Company, 2021 'McKinsey & Company.pdf', no date). Renewable energy continues to contribute more to total global energy production and it is predicted to produce 12000 TWh by end of 2030 in net zero emission scenario. While natural gas demand is expected to increase by 10% due to wide range of applications, oil demand is expected to slow down due to contribution from hydrogen production in transport sector (McKinsey & Company, 2021).

1.1.2 Nuclear energy's present status and contribution to world energy

After the development of sustained nuclear fission reaction by Enrico Fermi in the 1940s, it was not until the 1950s that commercial development of nuclear power plants began. Nowadays, Nuclear energy is responsible for providing 10% of total electricity generation in the world through four hundred and thirty-eight reactors, and it is the second largest carbon-neutral source of energy generation in the world. (World Nuclear Association 2022). Fifty-six nuclear reactors are under construction, and forty-eight are pressurized water reactors (PWR). The highest number of nuclear reactors (in total seventeen) construction is ongoing in China, followed by India (total of eight reactors). (*IAEA PRIS*, 2022). The United States of America is the world's largest nuclear energy provider, with a total of ninety-two nuclear reactors currently in service. (*IAEA PRIS*, 2022). Though France is in the second position in terms of the number of nuclear reactors, nuclear energy comprises about sixty-nine percent of total electricity generation, followed by Ukraine (fifty-five percent)(*IAEA PRIS*, 2022)

1.1.3 Prospects of small modular reactors (SMR) in future energy supply

Recently, Small Modular Reactors (SMR) have gained popularity worldwide due to their attractive features like easy build, simpler operation, and low carbon emission after the Fukushima accident. The small modular reactor is an attractive choice in limited grid capacity and power demand scenarios which can quickly provide small-scale stable baseload power in local communities of any country. Small modular reactor capacity is generally less than 300 MW_e in output and can be an affordable choice of energy generation considering the following facts (Kessides and Kuznetsov, 2012)

1. Small modular reactor size and power lead to less construction time, saving long-term costs for nuclear power plant construction. Easy modularization in factory sites can reduce on-site construction duration significantly.
2. The small reactor size can significantly reduce investment costs compared to larger nuclear power plants today. While constructing any sizeable nuclear power plant, investors cannot expect revenue generation until all investments are made. On the contrary, SMR can be deployed as a set of modules sequentially, which lower the burden of huge upfront cost for any investor.
3. As a rule of thumb, any constructed power plant should not exceed 10 percent of the grid size, as it can lead to grid instability. For countries with smaller and weak grids, SMR can be an attractive option to let countries take the facility of incremental capacity addition features of SMR without causing any major grid instability problems.
4. Production of SMR as a series of module factory help to reduce per-unit cost production. Fabricating components of several SMRs using the same assembly line can help optimize the production process and benefit from "economies of multiples."

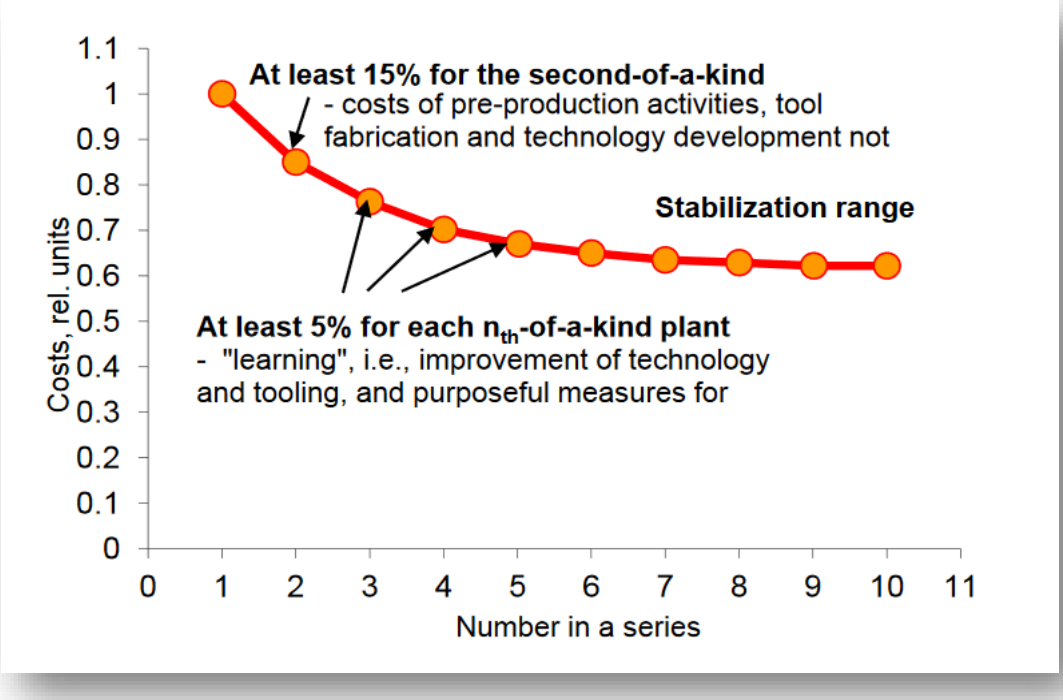

Figure 1: Reduction of fabrication and installation costs due to series deployment of SMR(Kessides and Kuznetsov, 2012)

5. With modular design, SMR can simplify design than large power plants. For example, most of the present SMRs at the development stage have in-vessel integrated

steam generators and no large-diameter piping system, which limits the likelihood of large-scale LOCA events.

More than seventy small modular reactors (SMR) are currently in the design and development phase. In December 2019, First SMR Akademik Lomonosov from Russian Federation connected to the grid, and commercial operation was initiated on May 22, 2020. All SMRS currently under development can be categorized under six categories as mentioned below(IAEA 2020)

1. Land-based water-cooled SMRs
2. Marine-based water-cooled SMRs
3. High-Temperature Gas-Cooled SMRs
4. Fast Neutron Spectrum SMRs
5. Micro-sized SMRs.

Light water-based SMRS are considered the most attractive choice regarding maturity, previous similar plant operation knowledge, and rapid technological development. Due to alignment with this thesis's scope, the following section will focus on the land-based water-cooled pressurized water reactor NuScale from NuScale Power LLC, United States of America.

1.1.4 Core features of NuScale small modular reactor (SMR)

NuScale reactor consists of a modular reactor core with 37 fuel rods and 16 control rod assemblies. The reactor pressure vessel (RPV), as shown in Figure-02, is a steel cylindrical vessel with a 2.7 m inside diameter and 17.7 m height and is designed to operate at 13.8 MPa pressure. The fuel ×assemblies contain a 17×17 array of zircalloy-clad, low-enriched (4.95%) uranium oxide (UO_2) with Gadolinium (III) oxide (Gd_2O3) as a burnable absorber. Because of non-proliferation issues, 4.95% enriched ^{235}U was used as fuel.

A central hot riser tube, a helical coil steam generator around the hot riser tube, and a pressurizer are located above the core. The helical coil steam generator comprises two sets of tube bundles, each having its own feedwater inlet and steam exit lines.

The helical coil steam generator comprises two sets of tube bundles, each having its own feedwater inlet and steam exit lines. Core inlet and outlet coolant temperatures are selected to be 265ºC and 321ºC. A helical coil steam generator provides higher heat transfer in a

relatively more minor volume, ensuring the system's compactness. Pressure vessel containment is designed to withstand high pressure, preventing rapid depressurization during the loss of coolant accident scenario (LOCA).

Primary reactor coolant takes heat from the reactor core and moves upward through the hot riser tube. The coolant reverses its direction at the pressurizer plate and flows over the steam generator shell side. Heat is transferred from the primary coolant to the secondary coolant via conduction. The direction of the primary coolant is reversed again at the lower head of the reactor pressure vessel and moves upward into the core. Coolant circulation is driven by natural circulation due to the density difference between heated and cooled primary coolants. At the secondary side of the steam generator, feedwater turns into superheated steam due to boiling and circulating to the turbine generator system.

Primary reactor coolant is circulated upward through the reactor core, and the heated water is transported upward through the hot riser tube. The coolant flow is turned downward at the pressurizer plate and flows over the shell side of the steam generator, where it is cooled by conduction of heat to the secondary coolant and continues to flow downward until its direction is again reversed at the lower reactor vessel head and turned upward back into the core. The coolant circulation is maintained entirely by natural buoyancy forces of the lower-density heated water exiting the reactor core and the higher-density cooled water exiting the steam generator. On the secondary side, feedwater is pumped into the tubes, which boil to generate superheated steam, which is circulated to a dedicated turbine-generator system. Low-pressure steam exiting the turbine is condensed and recirculated to the feedwater system.

Two trains connected with each steam generator loop can remove 100% decay heat through a passive condenser during non-LOCA events. The emergency core cooling system consists of three reactor vent valves and two reactor recirculation valves, ensuring system safety during emergencies. High-pressure steam generated during any emergency can be vented from the reactor vessel to high-pressure containment via a vent valve, ensuring steam condensation inside the containment. Liquid condensate is recirculated through the reactor recirculation valve inside the reactor vessel again. Heat transferred to containment ultimately discharges into the reactor pool surrounding the high-pressure containment (HPC).

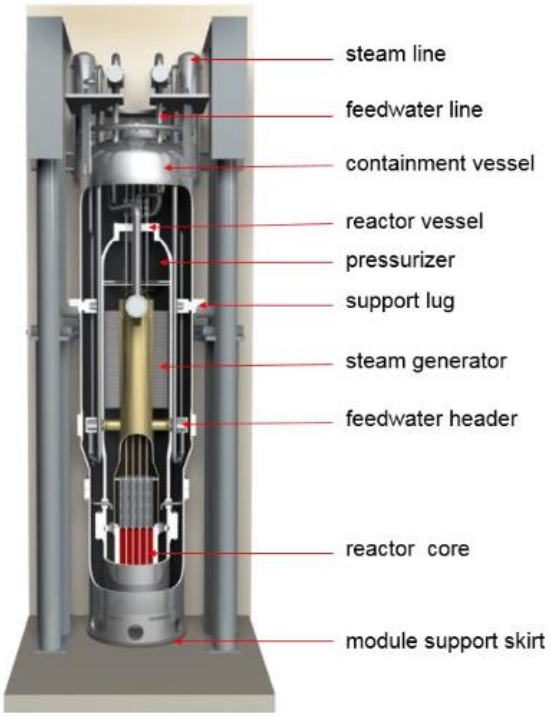

Figure 2: NuScale Reactor Containment System (Mikko Niemi 2017)

1.2 SCOPE OF STUDY

The scope of this study is to investigate boiling instability inside a helical coil steam generator. Helical coil steam generator has widely accepted application in nuclear and chemical plants. This type of study was performed by several authors earlier and had direct application to predict heat transfer phenomena inside a helical tube(Chung *et al.*, 2014a)

1.2.1 Goal & Objectives

This study investigates boiling instability inside a helical tube of the once-through steam generator. The specific goal associated with this research can be listed below

1. Experimental investigation of different flow parameters obtained from a MOTEL facility of LUT under the McSAFER Project.

2. Review existing literature about theory, model, experiments, and tests on stability map and propose stability map for the current facility.
3. Review literature about existing two-phase heat transfer and pressure drop correlations for helical tubes and calculate overall experimental heat transfer and pressure drop from experimental data.
4. Evaluate theoretical and experimental results obtained and suggest a possible future path for experimental works.

1.2.2 Approach & contribution

In this study following approximations are considered

1. **Scaled Test Facilities**: a MOTEL facility designed with a scale of 1:2 based on the available dimension of a naturally circulated pressurized water reactor (PWR). The time and velocity scale is adjusted according to the square root of the length scale ($1/\sqrt{2}$).
2. **Mode of heat transfer**: Only radial heat transfer is considered from primary fluid to the tube wall and from the wall's surface to the coolant.
3. **Fluid Properties**: Fluid properties inside the tube are evaluated at a bulk temperature, the average of the inlet and outlet temperature of coolant inside the tube.

1.2.3 Limitations

The empirical results reported here should be considered with certain limitations and interpreted with specific cautions while doing further work in this area.

1. Estimating fluid properties is based on temperature, and pressure readings are estimated qualitatively from different figures subjected to observational bias, hence the impact estimation of some parameters used in this study.
2. As there is no individual mass flow meter for each tube of the helically coiled steam generator, a simple methodology is applied to calculate the mass flow for each tube.
3. Heat loss calculation is not included while estimating the heat transfer coefficient.

1.3 OUTLINE

The thesis is organized into the following chapters

1. **Introduction**: Global energy scenario and the present status of energy are discussed. The potentiality of a small modular reactor (SMR) as a viable source of clean energy is presented later, followed by the scope and objectives of this study.
2. **Literature Review**: Boiling stability and heat transfer inside helical tubes related to earlier experimental studies were summarized and discussed.
3. **Description of MOTEL-SMR facility**: This chapter presents a detailed description of the MOTEL-SMR facility.
4. **Experiment & Data Analysis**: This chapter covers the detailed procedure of experimental analysis and data reduction method. Different equations and methods used to calculate several experimental parameters are discussed.
5. **Results & Discussion**: This chapter contains the presentation and discussion of experimental results. The evaluations and explanations of the results are based on physical phenomena.
6. **Conclusion**: A synopsis of the findings and their implications for the associated study is presented. A summary of the findings and implications from the accompanying study is provided. Many potential avenues for future investigation are mentioned.

2 LITERATURE REVIEW

This chapter discusses the literature review of different studies on flow inside helical coil steam generators. It covers different experimental studies, provides an overview of different test facilities, and develops associated correlations. Introductory theory about two-phase flow inside helical coil steam generator is presented, and associated dimensionless numbers are discussed. Previous correlations developed for two-phase pressure drop and heat transfer are reviewed, along with their associated parameters and application. Actual results and conclusions from previous stability prediction experiments are listed.

2.1 BACKGROUND & OUTLINE

Previously, helically coiled tubes were primarily used in Gas Cooled Reactors (GCR) and Liquid Metal Fast reactors (LMFR). Some of the earlier applications of the helically coiled tube for Gas Cooled Reactor (GCR) include 330 MWe HTGR from the USA and Thorium High-Temperature Reactor (THTR-300) from Germany. Among the Fast Reactors, the Super Phénix reactor (1200 MW_e) from France, Monju (280 MWe) from Japan, Enrico Fermi Fast Breeder Reactor from the USA, SNR-300 from Germany, and Advanced Liquid Metal Reactor (ALMR) from the USA used helical pipe (Ricotti, Cammi and Colombo, 2013). Recently, the helically coiled tube gained interest due to the recent proposal to make it part of Generation IV reactors.

Geometrical parameters involved in the helical tube are tube diameter (d) or tube radius r, coil diameter (D) or coil radius R, angle of inclination β, coil pitch P_s, coil pitch revolution of the coil h_s, dimensionless curvature λ and the dimensionless torsion δ (Ricotti, Cammi and Colombo, 2013).

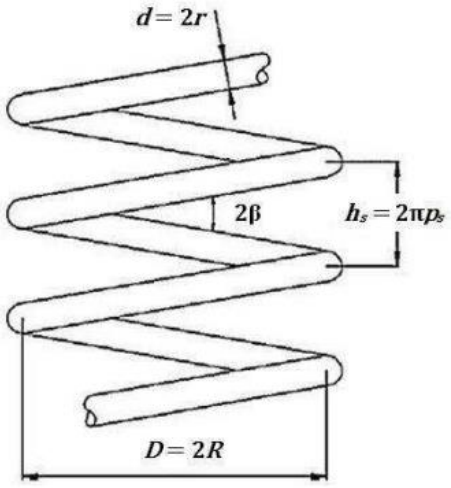

Figure 3: Schematic Diagram of Helical Pipe

Several definitions are available in earlier literature for estimating dimensionless curvature and dimensionless torsion. For example,

According to Germano,& Huttl, and Friedrich those two parameters can be expressed as(Ricotti, Cammi and Colombo, 2013)

$$\lambda = \frac{R^2}{\sqrt{R^2 + p_s^2}} \qquad (1)$$

$$\delta = \frac{p_s}{\sqrt{R^2 + p_s^2}}$$

Whereas according to Yamamoto et al.(Ricotti, Cammi and Colombo, 2013)

$$\lambda = \frac{rR}{R^2 + p_s^2} \qquad (2)$$

$$\delta = \frac{rp_s}{R^2 + p_s^2}$$

Di Piazza and Ciofalo listed those parameters (Ricotti, Cammi, and Colombo, 2013)

$$\lambda = \frac{r}{R} \qquad (3)$$

$$\delta = \frac{p_s}{R}$$

While dimensionless curvature gives an idea about centrifugal force, dimensionless torsion tells about the twisted path of the tube.

Some authors reported coil curvature ratio and modified curvature ratio as follows

$$\lambda_m = \frac{d}{2R_c} \qquad (4)$$

$$R_c = \frac{d}{2}\left[1 + \left(\frac{P_s}{\pi D}\right)\right]$$

Helical coil design parameters like the number of turns (N) and pitch (Ps) can be calculated using the following formulas

$$N = \frac{L}{\pi \times D} \qquad (5)$$

$$P_s = \frac{H}{N} - D$$

Where H is the elevation height of the helically coiled tube, L is the length of the spiral tube, and D is the coil diameter.

2.2 REVIEW OF EXPERIMENTAL STUDIES

2.2.1 Studies of flow inside the spiral tube

Flow inside a helical tube differs from a straight tube due to the presence of secondary flow. When fluid enters a curved surface due to centrifugal force, fluid in the core region experiences outward force, resulting in higher axial velocity in the core of the tube. To balance momentum, inside tube fluid of the core region moves to the outer surface region, and slower fluid from the outer wall moves to the inner region, creating secondary flow. This counter-rotating secondary flow is called Dean vortices, named after W. R. Dean.

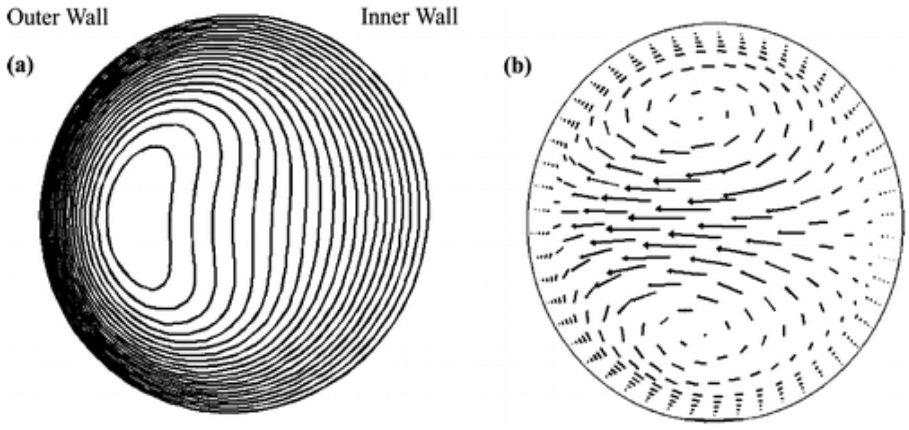

Figure 4: (a) Axial velocity on the outer surface (b) streamline of secondary flow in the inner wall

(Vashisth, Kumar, and Nigam, 2008)

Dean first reported that hydrodynamic instability inside curved surfaces like helical tubes could happen when the Reynolds number exceeds some critical value that can be predicted using a dimensionless number like Dean Number. It can be expressed below

$$De = \frac{\rho V d}{\mu}\left(\frac{d}{2R}\right)^{1/2} \quad (6)$$

Where,

ρ = Density of fluid

μ = Dynamic viscosity of a fluid

V = axial velocity scale

De= Dean Number

R = radius of curvature

At a low dean number (usually <45~60), the flow pattern inside the spiral and straight tubes are the same. With the increase of Dean number, some wavy perturbations start to be visible inside the tube, confirming the initiation of secondary flow. With further increase of Dean number, primary dynamic instability became stable. Flow becomes turbulent for Dean's number exceeding 400(Ligrani, 1994).

Over the years, several other authors studied flow inside the curved pipes and proposed other definitions of Dean number for a wide range of flow and geometrical ratios (curvature ratio, tube pitch). A different approach for the estimation of critical Reynolds number is listed below

Table 1: Several correlations for Critical Reynolds number estimation (Gou et al., 2017)

Ito(1959)	$Re_{crit} = 20{,}000(d/D)^{0.32}; 0.00116 < d/D < 0.0667$
Kubair and Kuloor (1966)	$Re_{crit} = 12730(d/D)^{0.2}; 0.0005 < d/D < 0.103$
Kutateladze and Borishanskii (1966)	$Re_{crit} = 2300 + 10500(d/D)^{0.3}; 0.0417 < d/D < 0.1667$
Schmidt (1967)	$Re_{crit} = 2300[1 + 8.6(d/D)^{0.45}]; d/D < 0.14$
Srinivasan et al. (1968)	$Re_{crit} = 2100[1 + 12(d/D)^{0.5}]; 0.004 < d/D < 0.1$
Mishra and Gupta(1979)	$Re_{crit} = 20{,}000\lambda_m^{0.32}; 10^{-13} < \lambda_m < 0.1$
El-Genk and Schriener (2017)	$Re_{crit} = 2300[1 + 5.164 \times 10^4 \lambda_m^{1.575}]^{0.2}$

Here D is helical diameter, d is tube diameter and λ_m is modified curvature ratio ($d/2R_c$) where R_c is coil curvature radius.

2.2.2 Review of two-phase pressure drop studies

Most earlier authors generally took two approaches to addressable. First, to adopt any existing correlation and model for pressure drop straight tube and later fine-tune it through proper adjustments and modifications to match with experimental conditions. Some authors produced their version of correlation through a multivariable fit of experimental data based on the most significant parameters. Some authors also took a mixed approach to study two-phase pressure drop inside the helical coil.

Most earlier work done in this area is based on the famous Lockhart-Martinelli multiplier (Chisholm, 1967). Pioneering work in this field was done by Owhadi et al. (Owhadi, Bell and Crain Jr, 1968), who studied forced convection boiling inside a helically coiled tube for a steam-water system and internal tube diameter 12.5 mm at atmospheric pressure with mass flux varied between 80 to 315 kg/m^{2}s. The proposed correlation showed ±15% mean error from experimental data. Later, Nariai et al. (NARIAI, KOBAYASHI, and MATSUOKA, 1982) developed a correlation based on Martinelli and Nelson (MARTINELLI, 1948), with a mean error of ± 30% when compared to data acquired from a marine reactor. Kozeki et al.(Kozeki *et al.* 1970) studied pressure drop inside the spiral tube at lower pressure and got a better correlation with a mean error of ±20% and showed pressure drop increases with both vapor quality and mass flux. Guo et al.(Guo, Feng, and Chen, 2001) developed a liquid-only multiplier-based correlation for two-phase pressure drop, including coil axial orientation of two helical tubes. They reported that experimental error is below ±40%. They found that the 45º downward inclined tube pressure drop is 70% higher than the pressure drop in the horizontal direction. They concluded the possible effect of increased pressure drop could be due to secondary flow inside a tube. They also concluded that the effect of vapor quality on frictional pressure drop is much more significant, below 0.3, compared to higher vapor quality(Fsadni and Whitty, 2016b). However, for the correlation created by Bi et al. (Bi et al., 1996), any impact of coil orientation on pressure drop is not visible at high pressure. Though some authors (Bi *et al.*, 1996; Zhao *et al.*, 2003a) did not find any effect of heat flux on pressure drop, the frictional pressure drop multiplier proposed by a recent study (Cioncolini and Santini, 2016) included the effect of heat flux. They found no effect of coil curvature on pressure drop and a mean error of 16.7%.

Ruffell developed a correlation for high-pressure (>3.5 MPa) systems from the electrically heated section of AGR (advanced gas reactors) and showed little effect of diameter ratio (d/D) on two-phase pressure drop.

2.2.3 Review of two-phase heat transfer studies

It is essential to know about appropriate experimental correlations developed for two-phase heat transfer to study the thermal hydraulics characteristics of the helical tube,. Previous studies reported various correlations based on system parameters like tube diameter, system pressure, mass flux, vapor quality, and heat flux. Some authors used well-known correlations for flow inside the straight pipe and agreed well with experimental data. The most popular correlations for heat transfer inside the straight pipe, as reported by earlier authors, are Chen correlation(Chen, 1966), Schrock and Grossman's vertical tube correlation (Schrock and Grossman, 1962), Steiner and Taborek Correlation (Steiner and Taborek, 1992) Crain and Bell correlations (Crain Jr, 1973). The first two correlations are particularly suited for large diameters (> 12 mm) and lower system pressure (<3.5 MPa). In contrast, Steiner and Taborek Correlation are suited for large tubes with pressure less than 7 MPa.

The first work on heat transfer inside helically coiled tubes was carried out by Owhadi et al. (Owhadi, Bell, and Crain, 1968). They reported forced convection boiling was predominant at higher steam quality while lower steam quality, usually below 0.1 nucleate boiling, also plays a role. They used Chen correlation to determine the heat transfer coefficient and found experimental data is within the 15 percent range of predicted data. Nariai et al.(Nariai, Kobayashi, and Matsuoka, 1982) studied thermal hydraulics inside helical tubes for integrated-type marine water reactors, and their proposed correlation based on Schrock and Grossman's correlation found well with experimental data for pressure less than 3.5 MPa. They also found that the average heat transfer coefficient decreased with an increased mass flow rate. Some other authors, like Hwang et al. and Chung et al., studied boiling heat transfer inside helically coiled tubes for pressure higher than 3.5 MPa and steam quality lower than 0.1.Hwang et al. (Hwang *et al.*, 2014) studied flow inside helical tubes for a wide range of pressure (1-6 MPa) and found higher heat flux increased heat transfer coefficient. Mass flux and coil curvature have a negligible effect on the heat transfer coefficient. For their experimental case Steiner-Taborek correlation predicted experimental data well (30%) in comparison to Chen correlation (40.2%) and Zhao correlation (145.3%)(Zhao *et al.*, 2003b). They

also included the dominance of nucleate boiling over convective boiling for their study. Chung et al. (Chung *et al.* 2014b) conducted a study at the same pressure as Zhao et al. but with lower mass and heat flux ranges. They found that higher pressure leads to a higher heat transfer coefficient though this effect was not prominent at low mass and heat flux ranges. Several other authors, like Kozeki et al., Campolunghi et al., and Guo et al., studied flow inside the helical tube for a wide range of system parameters(Fsadni and Whitty, 2016a). The most recent work by Santini et al. for a 24 m long helical tube facility showed the dependency of heat transfer coefficient on heat and mass flux and the role of both nucleate and convective boiling on heat transfer(Fsadni and Whitty, 2016a). Most authors who used linear tube correlation reported a negligible effect of coil curvature on heat transfer.

2.2.4 Review of stability studies

Instability in two-phase flow, like oscillation in flow rate or system pressure, can cause problems in terms of operational control and mechanical problems. Due to cyclic oscillatory behavior, flow wall temperature can go through periodic changes, which can cause failures due to thermal stress. To operate the plant safely and keep it in a stable region, it is important to know the threshold parameters of system flow rate, pressure, wall temperature, and steam quality. Commonly any system is said to be stable when it approaches the original operation conditions asymptotically, even after perturbation. Systems can be subjected to either static or dynamic instabilities. During static instability system approaches new conditions different from the then original one. Dynamic instability occurs due to boiling inside the channel, multiple feedbacks of system pressure flow rate, and temperature, or it can happen due to interaction and delayed feedback between inertia and compressibility of mixtures. Static instabilities can be categorized as (Kakac and Bon, 2008)

1. Ledinegg instability
2. Boiling crisis
3. Flow pattern transition instability
4. Bumping Geysering
5. Chugging

Dynamic Instabilities can be divided (Kakac and Bon, 2008)

1. Density-wave oscillations.
2. Pressure-drop oscillations

3. Acoustic oscillations
4. Thermal oscillations

Out of all the instabilities mentioned above, when considering thermal hydraulic instabilities, Density Wave Oscillations are the most prominent and studied, which usually happens as oscillatory behavior in the boiling system due to multiple feedback between mass flux, pressure drop, and a void fraction (Ugueto, 2013).

Density Wave Oscillation can be described using the following simple system. Suppose a boiling channel is connected to the inlet and outlet header and receives heat from the heat source. Inlet header pressure (Pi) and outlet header pressure (Po) is kept constant all the time, which means the pressure drop is constant. Suppose at time t=0, a perturbation happens, which increases inlet velocity. As inlet fluid enters the boiling channel, usually in a subcooled state

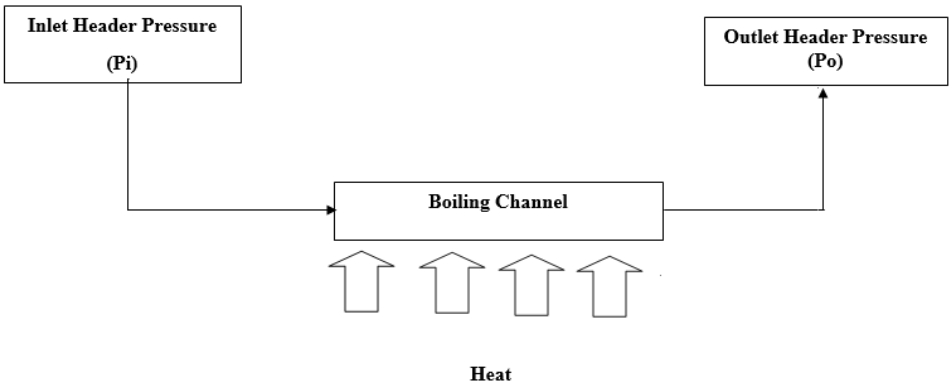

Figure 5: Simple system for density wave oscillation

An increase in liquid inlet velocity means a decrease in void fraction. As void fraction decreases, mixture density decreases. At the same time, t=0, this perturbation will send this high-density wave to the exit part of the channel. As this high-density wave has a higher mixture density and velocity, it will decrease the pressure drop at the channel's exit. Total system pressure drop is constant, so this reduction of exit pressure drop will instantaneously decrease pressure drop at the inlet. Reduction of inlet pressure drop will decrease void fraction at the inlet section, ultimately decreasing inlet velocity. This phenomenon will send a low-density wave to the exit section, resulting in a decrease of pressure drop at the exit section because lower density wave has lower Density and velocity. Hence, the inlet pressure drop increases again to keep the system pressure drop constant. This results in an increase in inlet velocity, and the whole oscillation cycle continues.

To understand and predict stability, better stability maps can be used. Most stability maps are represented as maps with the help of different dimensionless numbers. Most authors used either a homogenous or drift flux model to obtain a stability map.

According to Bourne and Mikaila, stability maps can be represented in terms of dimensionless velocity and enthalpy, as given below (Ugueto, 2013)

$$v^* = \frac{\dot{m}}{q} h_R \qquad (7)$$

$$h^* = \frac{h_l - h_i}{h_R}$$

v^*= dimensionless velocity, $\dot{m}$= mass flow rate (kg/s), q = added heat (kW), h_R = reference enthalpy(kJ/kg), h* = dimensionless enthalpy, h_l = saturated liquid enthalpy (J/kg), h_i = enthalpy at inlet section (J/kg).

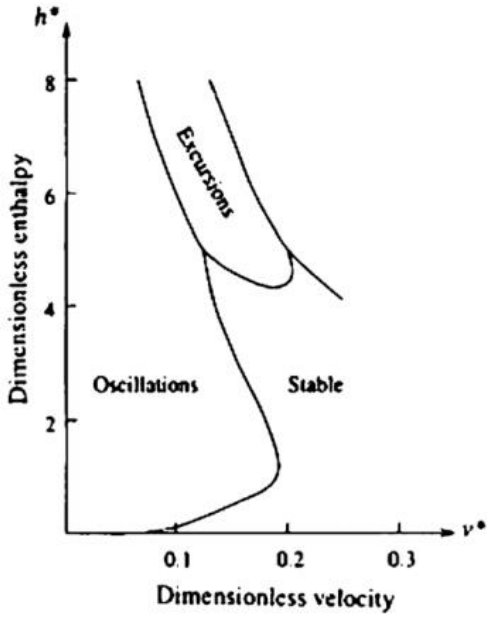

Figure 6: Boure and Mikaila Stability Map (Ugueto, 2013)

Ishii and Zuber proposed two dimensionless numbers (phase change number and subcooling number) for obtaining a stability map

$$N_{pch} = \frac{q}{\dot{m} h_{lg}} \frac{\rho_{lg}}{\rho_g} \qquad (8)$$

$$N_{sub} = \frac{h_l - h_i}{h_{lg}} \frac{\rho_{lg}}{\rho_g}$$

N_{pch} = dimensionless Phase Change number;

h_{lg} = Latent heat of vaporization (J/kg);

ρ_{lg} = density difference between saturated liquid and gas [kg/m^3];

ρ_g = saturated gas density[kg/m^3];

N_{sub} =Subcooling Number

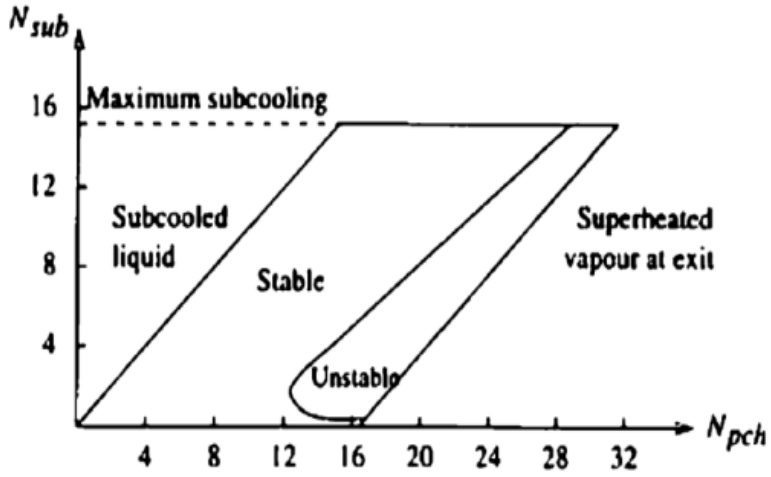

Figure 7: Ishii and Zuber Stability Map (Ugueto, 2013)

2.3 LIMITATIONS OF PREVIOUS STUDIES

1. No previous experiment has been carried out using integral-type test facilities to understand fluid behavior inside a helically coiled steam generator.
2. Most previous experiments used one or two helical coiled tubes to understand two-phase flow inside helical tubes.
3. MOTEL test facility used a tube bundle with the same tube diameter but a different length. It is also possible to use either one, two, three, or four tube bundles which provide a variety of choices to operate this steam generator at different levels. As MOTEL facility is unique in design, it is also possible to get test data replicating a wide range of scenarios which was not possible earlier with other facilities.
4. It is also possible in the MOTEL facility to exchange heater elements inside the core. As MOTEL facility has both core and steam generator, it is possible to study component level behavior alongside local behavior (heat, mass transfer). This unique experimental feature to check separate, mixed and integral tests using a single facility is not presently available in other regions. Using this kind of facility to study boiling instabilities is also not performed previously, as per the author's knowledge.

3 DESCRIPTION OF MOTEL-SMR FACILITY

This section details the MOTEL integrated test facility, located in LUT, Finland, and closely resembles the NuScale compact modular pressurized water reactor (PWR). With its modular structure, it can adopt multiple system configurations of currently existing nuclear power plants through interchangeable internal components. Though this facility currently lacks emergency cooling, decay heat removal and emergency cooling system can be integrated in the near future for further studies. It consists of four modules: an electrically heated core containing heating rods, an extension module, a helical coil steam generator, and a pressurizer.

3.1 BACKGROUND AND SECTION OUTLINE

Primary motivation for constructing the MOTEL facility is to provide a versatile experimental platform that can fulfill two objectives. First to represent any well-known existing system configuration of interest through modelling representative geometry (shape) in one single experimental platform. Second, the facility should allow for the investigation of single, mixed, and integrated effect tests.

One crucial aspect of MOTEL facility is its helical coil steam generator facility which is different than traditional horizontal or vertical U-Tube steam generator facilities. The majority of previous investigations on the intrinsic behavior of helical steam generators used standalone single coil (Andrzejczyk and Muszynski, 2017; Mirgolbabaei, 2018; Tuncer *et al.*, 2021) or multiple coil tubes (Genić *et al.*, 2012; Lu *et al.*, 2014; Lee and Hassan, 2022) with no reactor core facilities. Both primary and secondary water is heated with a preheater before entering the helical coil steam generator. Water is usually deionized to prevent scaling inside or outside the helical coil steam generator, which can impact heat transfer. Some facility also uses the throttling valve before the preheater for primary water flow to decrease inlet instability(Colombo *et al.*, 2011). However, for most studies, the shell side structure is relatively simple, hence not an actual representation of the heat transfer industrial scenario.

3.2 TEST FACILITY DESIGN OVERVIEW

The primary version of MOTEL Test facility is designed to represent SMR where both primary and secondary systems are inside vessels. Primary coolant water takes heat from the reactor core and rises at the top of the riser due to natural circulation. Primary water flows in annular downcomer space and exchanges heat with a steam generator through tube walls. Secondary water flowing inside the helical coil tube becomes superheated steam after heat exchange. Cooler primary water after heat exchange has higher Density which flows down to the bottom of the vessel due to gravity, and hence the whole cycle continues again. The design pressure of MOTEL Test facility is 4 MPa which is lower than the traditional pressurized water reactor due to cost issues, and the design temperature is 250ºC. The total height of MOTEL Test facility is 7.7 m with a diameter of 700 mm (Telkkä and Karppinen, 2018). The major components of facilities are described below

3.2.1 Core Design

The core height of MOTEL facility is chosen to be approximately 1.83 m which is half of the standard pressurized water reactor core (3.66 m). This is the same as the core height of NuScale SMR and almost the same as half of a typical pressurized water reactor like VVER-1200 and boiling water reactor (BWR). It makes it versatile to replicate any light water reactor core used today for study(Hyvärinen, Telkkä and Tielinen, 2022). The smaller core height of MOTEL-SMR than the traditional integral test facility makes it advantageous to study axial and radial heat transfer in the core region. In total, 293 rods are arranged in a square array inside the core, of which 132 are electrically heated rods, 145 are dummy rods, and 16 are instrumentation rods. Standard PWR core fuel bundle maintain about 1.2-1.3 pitch-to-diameter ratio. To keep approximately the same ratio for representative subchannel hydraulics, heater rods and dummy roads are arranged in a checkerboard array resulting in a 1.56 pitch-to-diameter ratio. Each heating rod has 1830 mm in length and 19.50 mm in diameter with 0.7 mm stainless steel cladding and magnesium oxide as a filler material (Hyvärinen, Telkkä, and Tielinen, 2022). Each heating rod can provide up to maximum7.5 kW of heating power, making the facility's total maximum heating power 990 kW(Telkkä

and Karppinen, 2018). The heating rod is designed to provide heat in a cosine shape like the current PWR reactor core. Dummy rods are simple steel bars with diameter of 18 mm.

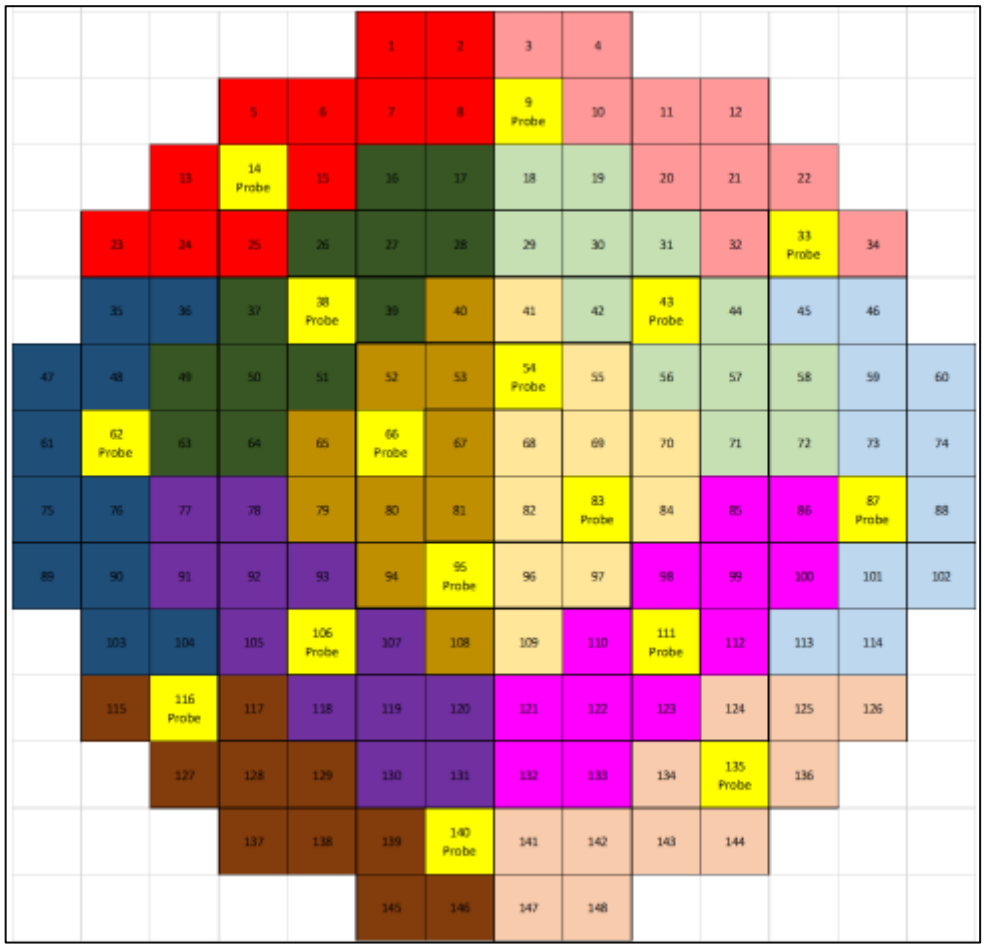

Figure 8: MOTEL basic rod configuration inside core (132 heating rods are divided into 12 individually controllable heating segments) (Hyvärinen, Telkkä and Tielinen, 2022)

3.2.2 Steam Generator

The steam generator used in this facility is a helical coil steam generator which has in total of 16 tubes with varying lengths (20 m to 25.1 m). Each tube has an outside diameter of 15 mm and a wall thickness of 1 mm(Hyvärinen, Telkkä and Tielinen, 2022). All tubes are divided into four bundles, half of them running clockwise and half of them running anti-clockwise. Each of these four bundles is connected with one feedwater collector to collect secondary feedwater and a steam connector to collect steam. The total heat transfer area of the steam generator (17 m^2) ensures that the average heat flux in the steam generator and reactor core is the same. The core and shell sides of the tube bundle are the loop friction source.

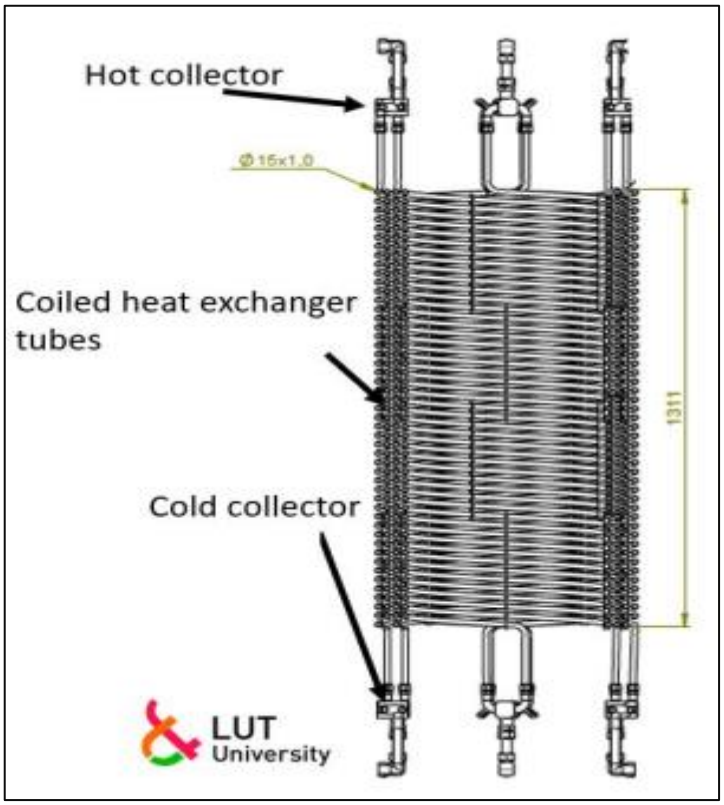

Figure 9: Helical Coil Steam Generator (Tielinen et al., 2021)

Diameter and length of tubes associated with different bundles are given below in tabular format

Table 1: Dimensions for different spiral groups

Spiral Group	Tube	Diameter of tube (mm)	Diameter of spiral (mm)	Length of spiral (m)
1	13-16	15	515	20.30
2	9-12		560	22.00
3	5-8		605	23.65
4	1-4		650	25.34

3.2.3 Riser Pipe

Riser pipe is made of two interconnected stainless-steel pipes and has 5.3 m height and 0.610 m diameter on one side and 0.485 m diameter on another side of the pipe. It separates annual downcomer space from the core, and it connects with the inner wall of the core-shell.

3.2.4 Pressurizer

Pressurizer is mounted on top of the pressure vessel and maintains 40 bar pressure through the rupture disk and safety valve, and there are two heater elements, each with 30 kW inside the pressurizer, and two additional valves (rotary quarter turn adjustment and shutoff ball) for pressure control.

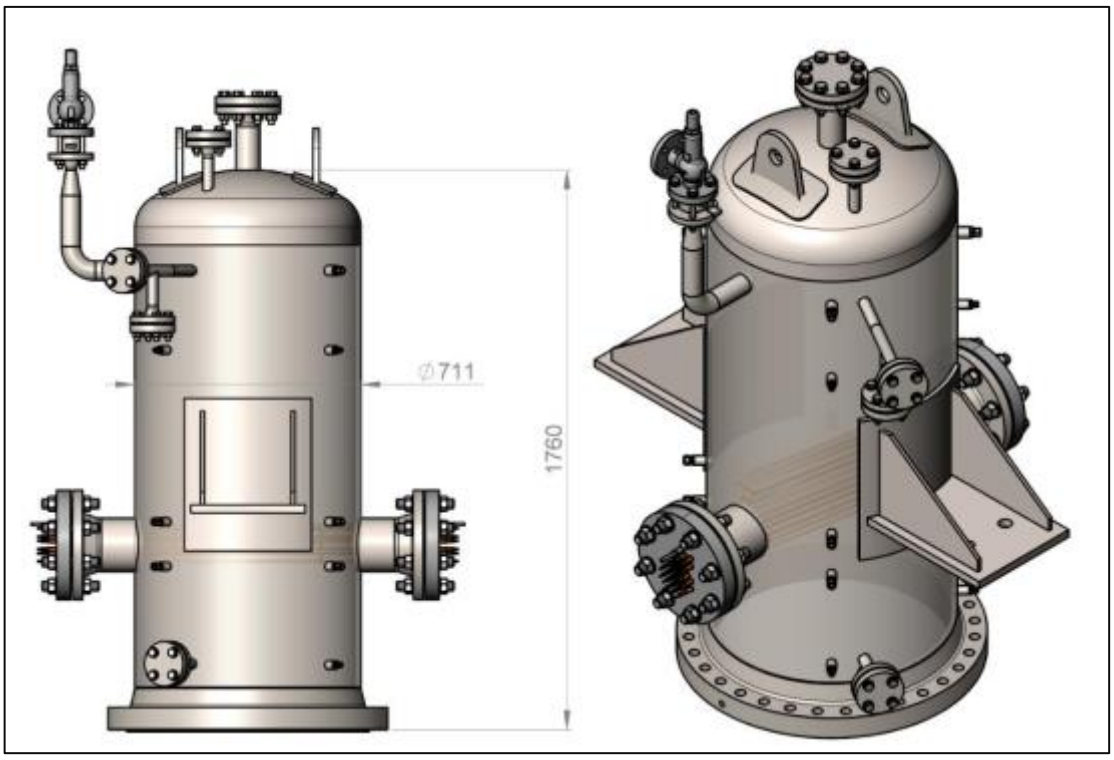

Figure 10: MOTEL Facility Pressurizer System (Telkkä and Karppinen, 2018)

3.2.5 Primary Water Level Control System

Primary water comes from the volume control tank, which stores excess water from the pressurizer during the heating period and can also provide water if the water level in the pressurizer needs to be increased. There is a heat exchanger and heater element inside the volume control tank. Excess water from the pressurizer can heat the feedwater, which goes into MOTEL pressure vessel. Feedwater is fed from the volume control tank to a facility through Speck triplex P30/43-1300 piston pump, and flow control is done with Varibell bell-shaped ball valve. Primary side water is demineralized and softened, and conductivity is adjusted to around (<10 μS/cm)(Tielinen *et al.*, 2021)

3.2.6 Secondary Water Level Control System

Secondary water is highly purified, which comes from a purified water supply system and is fed to the feedwater manifold. Water flow to the feedwater manifold can be controlled via a needle valve- Water from the feedwater manifold is then sprayed into steam generator tubes. A high-pressure piston pump (Spec triplex P21/32-130) is used for pumping feedwater.

3.2.7 Instrumentation & Measurement System Overview

Pressure Measurement

Pressure measurement is carried out in four different locations. Primary side pressure is measured at the top of the pressurizer (P6000), and secondary side pressure is measured at the steam manifold (P6001). Two other pressure measurements are done in the additional water pump at the primary side (P6002) and secondary feedwater pump (P6003).

In total, eight differential pressure measurement is used in the facility. Six differential pressure measurements are done at the pressure vessel's primary side. Two measure differential pressure from the bottom of the vessel to the top of the riser. The other four measure pressure from the bottom of the pressure vessel to the top of the pressurizer via the lower and top downcomer parts. One differential pressure measurement is done at cold collector four between the steam manifold and feedwater line (D6006), and another to measure the water level of the volume control tank (D6007).

Temperature Measurement

More than 340 thermocouples are used to measure temperature at different locations inside the facility. Most of them are K-type thermocouples, while those used inside heating rods are J-type. There are 212 thermocouples in the core region, of which 132 thermocouples are placed inside heater rods, and 80 thermocouples are placed inside measurement rods. Each heating rod accommodates one thermocouple, while each measurement rod has five thermocouples. In the steam generator, there are, in total, 79 thermocouples (T6280 to T6365) located inside each tube of four different bundles. Two of these thermocouples are placed near the hot and cold collectors, and the other three are placed at different elevations inside steam generator tubes.

In total, 13 thermocouples are located at the downcomer area to measure the primary water temperature at the annular downcomer area, and four are situated in the lower downcomer area (T6000...T6002), while ten thermocouples are located at the upper downcomer area (T6004...T6013). The pressurizer has 11 thermocouples, out of which five (T6014...T6018) measure temperature at the center of the pressurizer, and six thermocouples measure the surface temperature of heaters inside the pressurizer. There are 20 thermocouples (T6250...T6269) inside the hot riser. There are four additional thermocouples: three on the primary side of the system (T6026...T6028) and one on the secondary side of the system.

Flow Rate Measurement

In total, four flow rate meters are used in the facility. Two ultrasonic flow meters (F6000 & F6001) are used to measure the primary water flow rate at the annular downcomer, one magnetic flow meter (F6002) is used to measure the introductory side flow rate, and one Pelton wheel flow meter (F6005) is used to measure secondary side flow rate.

Other Additional Measurement Systems

The power of 12 core heating sections is controlled via 12 solid-state relays, while the power of pressurizer heaters is controlled via three solid-state relays. The cRIO data acquisition system from National Instruments measures all signals.

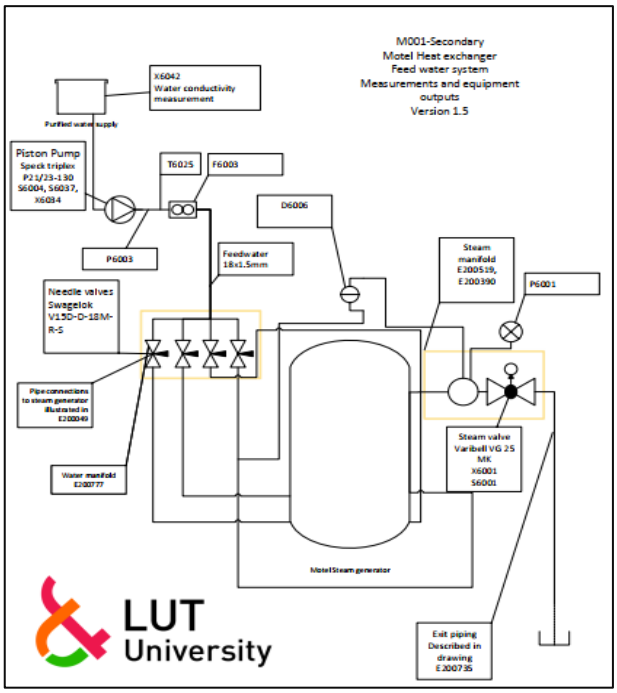

Figure 11: Diagram of secondary side system (Tielinen et al., 2021)

4 EXPERIMENT & DATA ANALYSIS

This chapter deals with the experimental procedure followed during different experiments and describe the methods and equations used for data analysis. The estimation procedure for different parameters like mass flow rate in different channels, dimensionless heat flux, heat transfer coefficient, pressure drop, and selection justification are summarized in different sections.

4.1 BACKGROUND AND OUTLINE

Before proceeding to the data analysis section, it is essential to know the physics phenomena behind steam generation inside the helical tube. Figure 12 illustrates steam generation inside the helical tube while heat transfer from primary fluid on the annular side. Primary fluid flows downward due to gravitational force, while water flows upward, representing a counter-current heat exchanger. Secondary feedwater enters the tube with temperature T_{FW} and mass flow rate $\dot{m}_s$ and after heat exchanging with primary fluid exits with temperature T_{STM} and secondary pressure P_{STM}. Primary fluid has $\dot{m}_p$ flow rate and temperature T_p before heat transfer. Tube wall characteristics like thermal conductivity, tube thickness, and surface properties can affect heat transfer. Due to the no-slip condition, the secondary water inlet velocity at the tube's inner wall surface is zero. It is assumed that the thickness of the heating wall does not affect wall temperature; hence, the inner and outer wall temperature (Tw) is the same. A film with temperature T_f is assumed at the inner wall surface, which is used to evaluate mixture properties inside the helical tube. The overall heat transfer coefficient depends on the tube heat transfer coefficient (h_s) and shell side heat transfer coefficient (h_p). It is assumed that both primary and secondary feed water is free from non-condensable gas; hence, non-condensable gas cannot act in overall heat transfer.

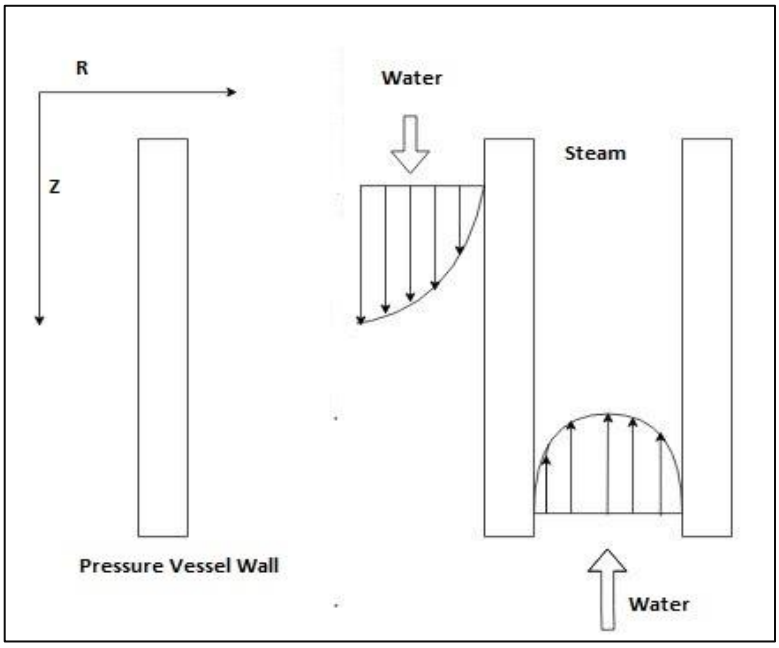

Figure 12: Steam generation through water boiling inside the tube

4.2 EXPERIMENTAL PROCEDURE

In total, five experiments were carried out to test the behaviour of the steam generator during operation. For all tests, primary pressure is set to 35 bar while secondary pressure is set to 10 bar. A summary of all tests and experimental procedures followed are listed below in the tabular format

Table 2: Test name and Test Duration

Name of Test	Total Test Duration (s)	
	Start	End
MS-SG02	0	18400
MS-SG01R	0	8700
MS-SG01A	0	3700
MS-SG01B	0	4000
MS-SG03	300	16000

4.3 METHOD OF DATA ANALYSIS

Different methods used to estimate other parameters to understand better flow inside the helical tube are summarized below in separate sections.

4.3.1 Estimation of flow parameters for helical tube

To understand flow inside the helical tube, it is essential to estimate different flow parameters to establish a flow map for boiling flow inside the helical tube.

average superficial velocities for liquid (j_l) and gas (j_g) flow can be written as,

$$j_g = \frac{\langle x_e \rangle \dot{m}_s}{\rho_g a_t} \text{ and } j_l = \frac{[1 - \langle x_e \rangle]\dot{m}_s}{\rho_l a_t} \quad (9)$$

Where $\langle x_e \rangle$ Is spatial average equilibrium vapor quality which can be estimated (Reyes, 2019)

$$\langle x_e \rangle = \frac{x_e}{2} = \frac{h_{exit} - h_i}{2h_{lg}} \quad (10)$$

h_{exit} = enthalpy of steam at outlet pressure (kJ/kg)

h_i = enthalpy of secondary feedwater at the inlet pressure (kJ/kg)

h_{lg} = enthalpy of evaporation (kJ/kg).

Inlet feedwater pressure is not measured during the experiment. However, as mentioned before SPECK TRIPLEX 21/23-130 high-pressure plunger pump is used to circulate secondary feedwater, which can deliver a maximum of 130 bar pressure at 23.1 l/min flow. Intermediate working pressure can be interpolated from the measured flow rate ('SPECK TRIPLEX', 2022).

Dimensionless volumetric flux for gas ($j_{g)}^+$ and liquid (j_l^+) can be defined as,

$$j_g^+ = \frac{j_g}{\sqrt{gd(\Delta\rho/\rho_g)}}; j_l^+ = \frac{j_l}{\sqrt{gd(\Delta\rho/\rho_l)}} \quad (11)$$

Void fraction α can be written as,

$$\alpha \equiv \frac{A_g}{A_g + A_l} \quad (12)$$

A_g = cross-sectional area occupied by gas phase

A_l = cross-sectional area occupied by liquid phase

In this equation, d = tube inside diameter, $\Delta\rho$ = density difference (ρ_l - ρ_g) and g = gravitational acceleration.

It can be written in a different way, as below

$$\alpha = \frac{1}{1 + \frac{1 - \langle x_e \rangle}{\langle x_e \rangle} \cdot \frac{\rho_g}{\rho_l} \cdot S_R} \quad (13)$$

Where S_R is called slip ratio, which is the ratio of vapor and liquid velocity and is dimensionless in nature, different correlations are used for calculating slip ratio. Some of the most important correlations are mentioned below in increasing accuracy order.

Homogenous Equation Model,

$$S_R = 1 \quad (14)$$

Zivi's slip correlation,

$$S_R = \sqrt[3]{\frac{\rho_l}{\rho_g}} \quad (15)$$

Chisholm's slip correlation,

$$S_R = \sqrt{1 - \langle x_e \rangle \cdot \left(1 - \frac{\rho_l}{\rho_g}\right)} \quad (16)$$

For simplification of the study, the slip ratio is taken as one as the Homogenous Equilibrium Model.

Dimensionless pressure drop (ΔP^+) can be written as (Reyes, 2019)

$$\Delta P^+ = \left[\frac{\left(j_g^+\right)^2}{\alpha^{3/2}} + \frac{(j_l^+)^2}{(1-\alpha)^{3/2}}\right] \quad (17)$$

4.3.2 Estimation of mass flow rate in the parallel helical tube

As mentioned before, each bundle has four tubes with different lengths and diameters in a helically coiled steam generator. Each of these bundles connects with a common inlet and steam header through cold and hot collectors, as described before. So those helically coiled tubes can be treated as a parallel heated channel with a common plenum and the same pressure drop.

When all tubes are vertically oriented with the same common plenum pressure drop (Δp_n) can be written as (Todreas and Kazimi, 2001)

$$\Delta p_n \equiv p_n(\text{ lower }) - p_n(\text{ upper }) \quad (18)$$

Any tube n pressure drop can be rewritten as (Todreas and Kazimi, 2001)

$$\Delta p_n = \int_0^H \rho_{mn} g dz + \int_0^L \frac{f_n G_{mn}|G_{mn}|}{2D\rho_{mn}} dz + \sum_i \frac{K_{in} G_{mn}|G_{mn}|}{2\rho_{mn}} + G_{mn}^2 \left[\frac{1}{\rho_{mn}^+(H)} - \frac{1}{\rho_{mn}^+(0)}\right] \quad (19)$$

The first term denotes the gravity term; the second term represents the frictional loss term; the third term indicates the local pressure loss term, and the fourth term means the acceleration term. Several conditions and approximations are applied to the above (17) equation.

1. For the same elevation height (H) gravity term will be the same for each tube.
2. Acceleration pressure drop (fourth term in equation (19)) contribution in total pressure drop can be neglected for low mass flow rate and one-dimensional problems.
3. Any loss of local pressure like exit, entrance, and form along the channel is negligible.
4. All tubes are in the same region (laminar or turbulent).

For all tubes, acceleration and gravity terms will be the same. The only difference will be frictional terms due to different length (L). Equation (17) can be rewritten as

$$\Delta p_n = f_n \frac{L_n}{d_n} \frac{G_n^2}{2 \cdot \rho} \quad (20)$$

Where f_n is friction factor, L_n is tube length, d_n is tube diameter, G_n is tube mass flow rate, ρ is mixture density.

Friction factor can be written as (Todreas and Kazimi, 2001)

$$f_n = 0{,}184 \cdot Re^{-0,2} \quad (21)$$

Where Re is Reynolds Number

$$Re = \frac{\rho \cdot d \cdot v}{\mu} = \frac{d \cdot \dot{m}}{A \cdot \mu} \quad (22)$$

Combining equations (18), (19), and (20) results in

$$\Delta p_n = 0{,}184 \cdot \left(\frac{d \cdot \dot{m}}{A \cdot \mu}\right)^{-0,2} \frac{L_n}{d_n} \frac{\dot{m}_n^2}{2 \cdot \rho \cdot A^2} \quad (23)$$

Pressure drop is the same; hence $\Delta P_1 = \Delta P_2 = \Delta P_3 = \Delta P_4$. So, equation (21) can be written as

$$0{,}184 \cdot \left(\frac{d \cdot \dot{m}_1}{A \cdot \mu}\right)^{-0,2} \frac{L_1}{d} \frac{\dot{m}_1^2}{2 \cdot \rho \cdot A^2} = 0{,}184 \cdot \left(\frac{d \cdot \dot{m}_2}{A \cdot \mu}\right)^{-0,2} \frac{L_2}{d} \frac{\dot{m}_2^2}{2 \cdot \rho \cdot A^2} = 0{,}184 \cdot \left(\frac{d \cdot \dot{m}_3}{A \cdot \mu}\right)^{-0,2} \frac{L_3}{d} \frac{\dot{m}_3^2}{2 \cdot \rho \cdot A^2} = 0{,}184 \cdot \left(\frac{d \cdot \dot{m}_4}{A \cdot \mu}\right)^{-0,2} \frac{L_3}{d} \frac{\dot{m}_4^2}{2 \cdot \rho \cdot A^2} \quad (24)$$

From the above equations, it can be written

$$\frac{\dot{m}_1}{\dot{m}_2} = \left(\frac{L_2}{L_1}\right)^{\frac{1}{1.8}} \quad (25)$$

$$\frac{\dot{m}_1}{\dot{m}_3} = \left(\frac{L_3}{L_1}\right)^{\frac{1}{1.8}}$$

$$\frac{\dot{m}_1}{\dot{m}_4} = \left(\frac{L_4}{L_1}\right)^{\frac{1}{1.8}}$$

From equation (25), it is evident that the mass flow rate is inverse to tube length. So, a tube with a higher length has a lower mass flow rate.

The mass flow rate entering each bundle and each tube can be written as

$$\dot{m}_T = \dot{m}_{b_1} + \dot{m}_{b_2} + \dot{m}_{b_3} + \dot{m}_{b_4} \quad (26)$$
$$\dot{m}_b = \dot{m}_1 + \dot{m}_2 + \dot{m}_3 + \dot{m}_4$$

Where, $\dot{m}_T$ = total mass flow rate from feedwater pump

$\dot{m}_b$ = mass flow rate in each bundle (subscript 1,2,3 & 4 represents bundle 1,2,3 & 4)

$\dot{m}_1$, $\dot{m}_2$, $\dot{m}_3$, $\dot{m}_4$ = flow rate in each tube (subscript 1,2,3 & 4 represents spiral group 1,2,3 & 4)

4.3.3 Estimation of heat transfer coefficient

According to some earlier studies (Fsadni and Whitty, 2016a), the helical coil tube's curvature does not significantly affect the heat transfer coefficient. Currently, existing correlations for estimating the heat transfer coefficient inside a straight tube can usually be applied to a helical tube without any significant discrepancy for sizeable inner diameter (>12 mm) and system pressure lower than 7 MPa. The most famous correlation for estimating two-phase heat transfer inside a straight tube is Chen, Scrock, and Grossman correlation which was first used by Owhadi et al. (Owhadi, Bell and Crain, 1968).

$$h_s = 0.00122 \frac{k_l^{0.79} c_{p_l}^{0.45} \rho_l^{0.49}}{\sigma^{0.5} \mu_l^{0.29} h_{lg}^{0.24} \rho_g^{0.24}} \cdot \Delta T_{sat}^{0.24} \cdot \Delta P_{sat}^{0.75} S + 0.023 Re_l^{0.8} Pr_l^{0.4} \frac{k_l}{d} F \quad (27)$$

Where,

$$S = \frac{1}{1 + 2.53 \times 10^{-6} F^{1.25} R_{e_l}}$$

$$F = 1.0 \text{ for } \frac{1}{\chi_{tt}} \leqslant 0.1$$

$$F = 2.35 \left(\frac{1}{\chi_{tt}} + 0.213 \right)^{0.736} \text{ for } \frac{1}{\chi_{tt}} > 0.1$$

Heat transfer to water inside the tube can be written as

$$\dot{q} = \dot{m}_s (h_{exit} - h_i) \quad (28)$$

To calculate ΔT_{sat} and ΔP_{sat} It important to know the wall temperature (T_w), which is not measured. So iterative procedure is needed. After estimation of the tube heat transfer coefficient (h_t) wall temperature (T_w) can be estimated again using the following equation,

$$T_w = \frac{q}{A_i h_i} + T_b \quad (29)$$

Where A_i is tube inlet area (m^2), h_i is tube heat transfer coefficient (kJ/kg.k), q is heat transfer rate to the tube (kJ/sec), T_b is the bulk temperature which is computed as the Average of inlet and outlet temperature of the water inside the tube. When calculated, wall temperature (T_w) is reasonably close to the assumed wall temperature (T_w) outside heat transfer coefficient (h_p) can be calculated using the following equation

$$h_p = \frac{q}{A_o (T_p - T_w)} \quad (30)$$

T_p = Average of ten temperature recordings (T6004….T6013) at different locations indicating primary fluid temperature.

The overall heat transfer coefficient can be calculated using tube and shell side heat transfer coefficient as below (Vishvakarma, Kumbhare, and Thakur, 2016)

$$U_{calc} = \frac{1}{\left[\frac{1}{h_p} + \frac{r_0 \ln \left(\frac{r_o}{r_i} \right)}{k} + \frac{r_0}{r_i h_s} \right]} \quad (31)$$

The experimental overall heat transfer coefficient can be calculated using the following equation

$$U_{exp}=\frac{q}{A_0\left(T_p-T_b\right)} \quad (32)$$

4.3.4 Estimation of two-phase pressure drop inside the tube

Several correlations are reported by earlier researchers for estimating two-phase pressure drop inside the helical tube for a wide range of system parameters like pressure, heat flux, mass flow rate, and mass flux. The total two-phase pressure drop consists of three components frictional, gravitational, and momentum pressure drop. Most earlier researchers reported two-phase pressure drop as a function of single-phase liquid pressure drop using a liquid-only multiplier. It can be expressed as below (Fsadni and Whitty, 2016b)

$$\Delta P_{total,TP}=\Delta P_{f,TP}+\Delta P_{grav}+\Delta P_{acc} \quad (33)$$

$$\Delta P_{f,TP}=\Delta P_l \emptyset_l^2$$

$$\Delta P_{grav}=\left[\frac{gH}{x_{exit}-x_{inlet}}\right]\left[\frac{\ln\left(1+x\left(\frac{\rho_l}{\rho_g}-1\right)\right)}{\left(\frac{1}{\rho_g}-\frac{1}{\rho_l}\right)}\right]_{exit}-\left[\frac{gH}{x_{exit}-x_{inlet}}\right]\left[\frac{\ln\left(1+x\left(\frac{\rho_l}{\rho_g}-1\right)\right)}{\left(\frac{1}{\rho_g}-\frac{1}{\rho_l}\right)}\right]_{in}$$

$$\Delta P_{acc,TP}=G^2\left\{\left[\frac{1-x}{\rho_l}+\frac{x}{\rho_g}\right]_{exit}^{-\left[\frac{1-x}{\rho_l}+\frac{x}{\rho_v}\right]_{in}}\right\}$$

Φ_l^2 is the only liquid friction multiplier that can be expressed in terms of so Martinelli parameter χ, which is the ratio of the single-phase liquid pressure drop to the single-phase vapor pressure drop and constant C whose value can be taken as 20 for turbulent flow.

$$\Phi_l^2=1+\frac{C}{\chi}+\frac{1}{\chi^2} \quad (34)$$

Where Martinelli Parameter

$$\chi^2=\frac{\left(\frac{\Delta p}{L}\right)_l}{\left(\frac{\Delta p}{L}\right)_v}=\left[\frac{(1-x)}{x}\right]^{1.8}\frac{\rho_v}{\rho_l}\left(\frac{\mu_l}{\mu_v}\right)^{0.2} \quad (35)$$

Now single-phase liquid-only pressure drop depends on Darcy friction coefficient

$$\Delta P_l = \left(\frac{\Delta p_{fr}}{L}\right)_l = \frac{f_D}{2}\frac{G^2}{\rho_l d} \quad (36)$$

There are several ways to calculate Darcy friction coefficient, as mentioned in earlier works of literature.

Table 3:Darcy Friction Coefficient for Turbulent Flow (Ricotti, Cammi and Colombo, 2013)

	Turbulent regime	
Correlation	**Validity range**	**Reference**
$f_D = 0.32Re^{-0.25} + 0.048(d/D)^{0.5}$	$15000 < Re < 100000$	White (1932)
$f_D = 0.304Re^{-0.25} + 0.029(d/D)^{0.5}$	$0.034 < Re(d/D)^2 < 300$	Ito (1959)
$f_D = 0.3164Re^{-0.25} + 0.03(d/D)^{0.5}$	$4500 < Re < 100000$	Mishra e Gupta (1979)

Among above mentioned three correlations, as proposed by Ito, seem to have better agreement with experimental data as studied by Ricotti et al. (Ricotti, Cammi, and Colombo, 2013). So, this correlation is selected for comparison with experimental facility data.

5 RESULTS AND DISCUSSION

This section provides a detailed discussion of results obtained from different experiments using the MOTEL facility. How system parameters like steam generator tube temperature, feedwater temperature, and primary fluid temperature change concerning changes in core power are discussed in the following sections.

5.1 EXPERIMENTAL INVESTIGATION OF SYSTEM PARAMETERS FOR DIFFERENT TESTS

In total, five experiments (MS-SG01A, MS-SG01B, MS-SG01R, MS-SG02, MS-SG03) are carried out to test the behavior of the MOTEL facility. For each test, primary and secondary side pressure (P6000 & P6001) are kept constant. All experimental results are categorized into bundle and spiral groups for better comparison of results. Each bundle has four tubes with different lengths but the same tube diameter. For each spiral group, the length and diameter are both the same. The main parameter for the experimental study is the temperature of the fluid inside the tube during boiling at different locations (3.423m, 3.983m, 4.323 m, 4.663 m, and 5.228 m). After MS-SG01R test was carried out instrumentation piping was changed, which affected the secondary side pressure drop measurement (D6006). For MS-SG01R experiment, pressure drop data (D6006) indicates the average pressure drop in all bundles, while for other tests, it indicates a pressure drop in bundle-04. This results in extending of range for pressure drop measurement.

5.1.1 Study of MS-SG01A test results

There are four bundles in the steam generator. For simplicity, only data for one bundle is mentioned and shown here unless some significant deviations are observed for other bundles. Experimental data is analyzed for 100 seconds after the change in power step.

Tube temperature at different locations for all bundles

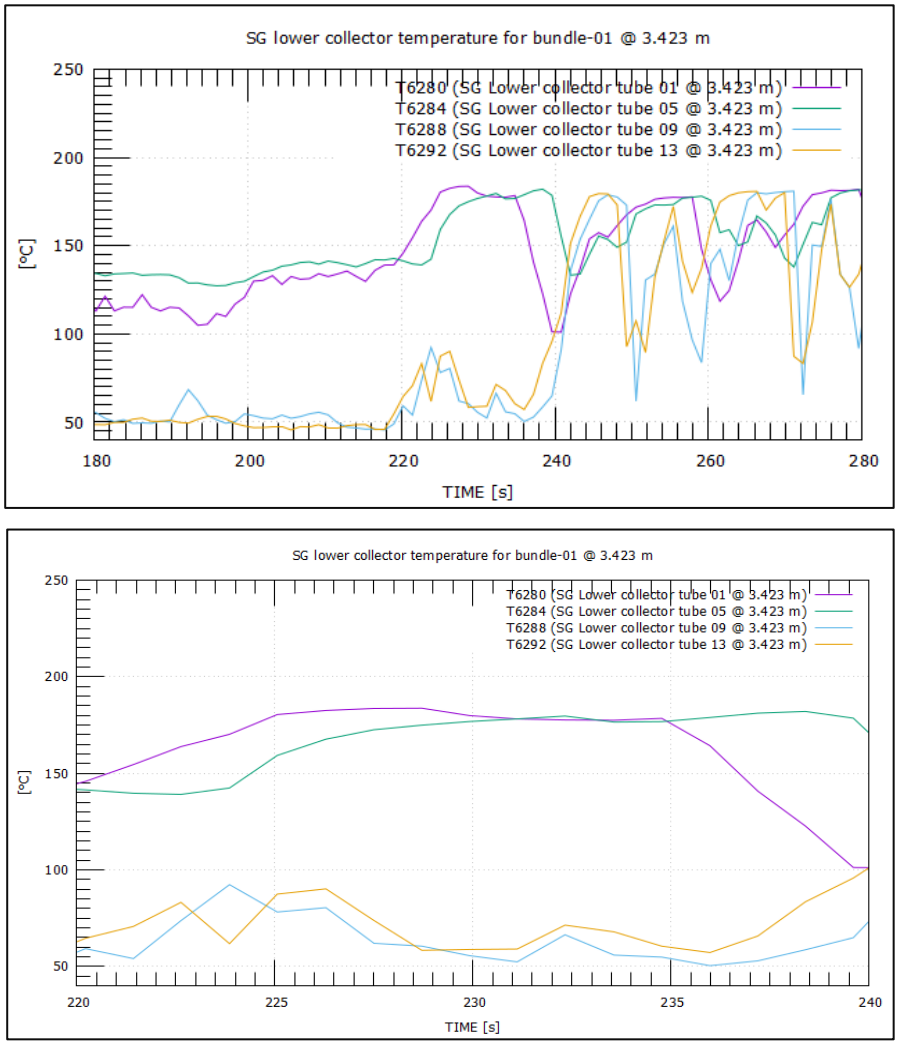

Figure 13: (a) Tube temperature for Bundle-01 at 3.423 m for 180-280 sec (b) Tube temperature for Bundle-01 at 3.423 m for 220-240 sec (MS-SG01A)

At 100 seconds 750 kW power step was applied, and the temperature inside the tubes started to increase. Though all tubes have the same diameter, tube 01 has the highest length, followed by tubes 05, 09 & 13. So, tube 01 and tube 05 experienced high superheating due to high heat surface area (πdL) compared to the other two tubes. Moreover, tubes 01 and 05 have lower mass flow due to the long length. Hence, the initial temperature for tubes 01 and 05 is much higher than for tubes 09 and 13. Then at around 220 seconds, the temperature started to oscillate for all tubes. This thermal oscillation can be attributed to pressure drop

oscillation due to frictional loss, which is a common phenomenon for density wave oscillation as it has a relatively high amplitude and low frequency. The graph shows that the oscillation period is higher for tubes 01 & 05 (approximately 20 seconds) compared to tubes 09 and 13 (approximately 10 seconds).

Moreover, for any oscillation, lower mass flow results in oscillation with high frequency but low amplitude due to less turbulence and less friction which is evident for tubes 01 & 05 (amplitude-80ºC) compared to tubes 09 & 13 has higher mass flow rate (amplitude-130ºC). As it takes some time to reach flow from the entry point to the top of the tube for other locations, the plot is presented for 600-700 seconds instead of 180-280 seconds. For higher elevation (at 3.983 m), there are some periodic oscillations that are on the reverse side compared to oscillation observed for the temperature at 3.423 m. The thermometer at 3.423 m is located around the cold collector region, while the thermometer at 3.983 m is the first thermometer located around the helically coiled tube. It can experience turbulences due to the entrance effect and the secondary flow inside the helical tube, which can result in occasional temperature drops. The tube temperature at 4.323 m again showed some oscillation on the positive side with a lower amplitude than the temperature at 3.423 m. As the flow becomes steady inside tubes, oscillation shows small amplitude and frequency. Both oscillation amplitude and period increased for the temperature at 4.663 m and 5.228 m.

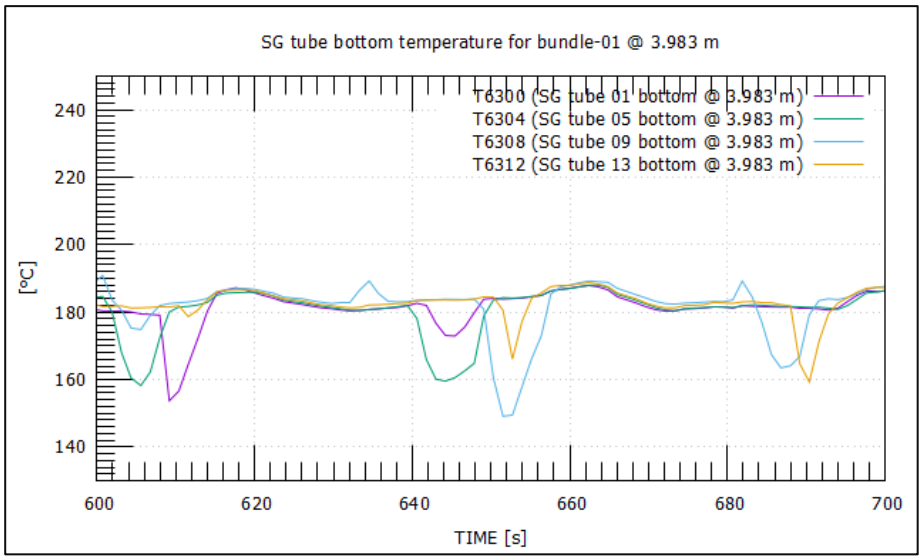

Figure 14:Tube temperature for Bundle-01 at 3.983 m for 600-700 sec (MS-SG01A)

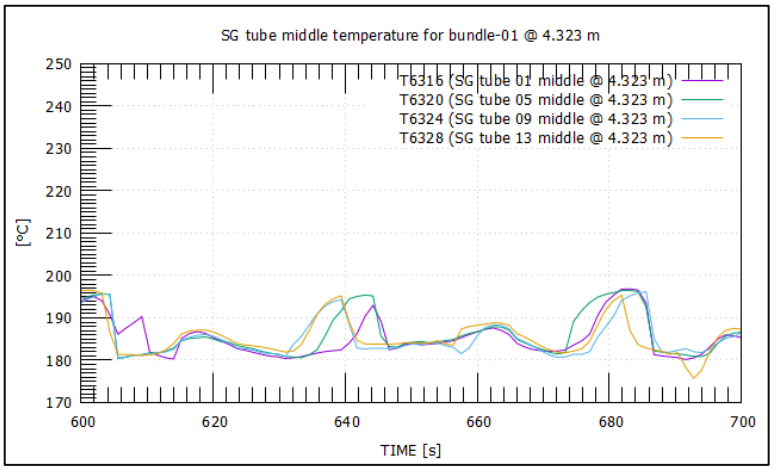

Figure 15:Tube temperature for Bundle-01 at 4.323 m for 600-700 sec (MS-SG01A)

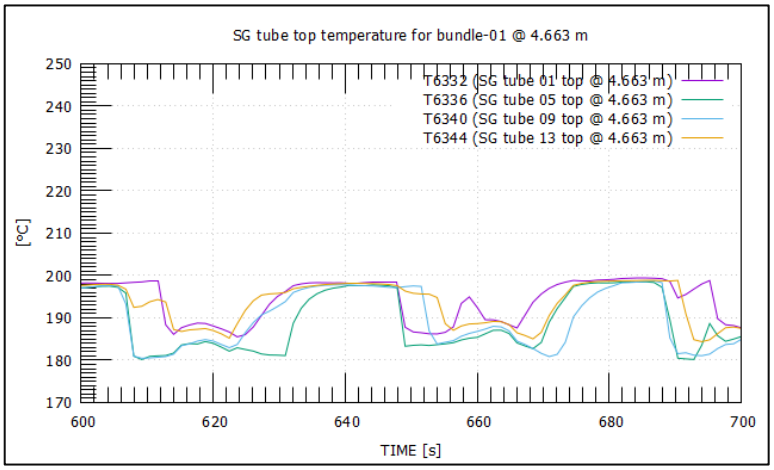

Figure 16:Tube temperature for Bundle-01 at 4.663 m for 600-700 sec (MS-SG01A)

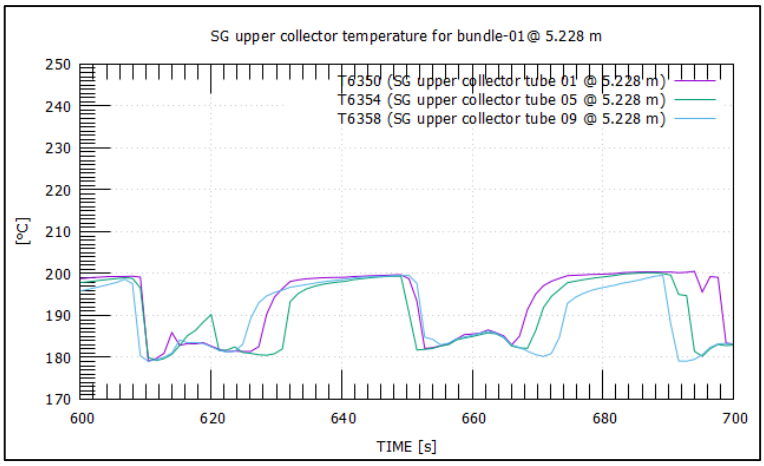

Figure 17:Tube temperature for Bundle-01 at 5.228 m for 600-700 sec (MS-SG01A)

Same Spiral Group (Same length & diameter)

Except for tube-14, the other three tubes in Figure 18 follow the same temperature pattern until 220 seconds. After that, as pressure drop increase inside tubes, temperature oscillation happens. For tube temperature at all other locations, tube amplitude and period are the same though not all temperature oscillations are synchronized for the same tube type under spiral group 01. This can be due to the time difference that exists between the flow inside the tube in different bundles.

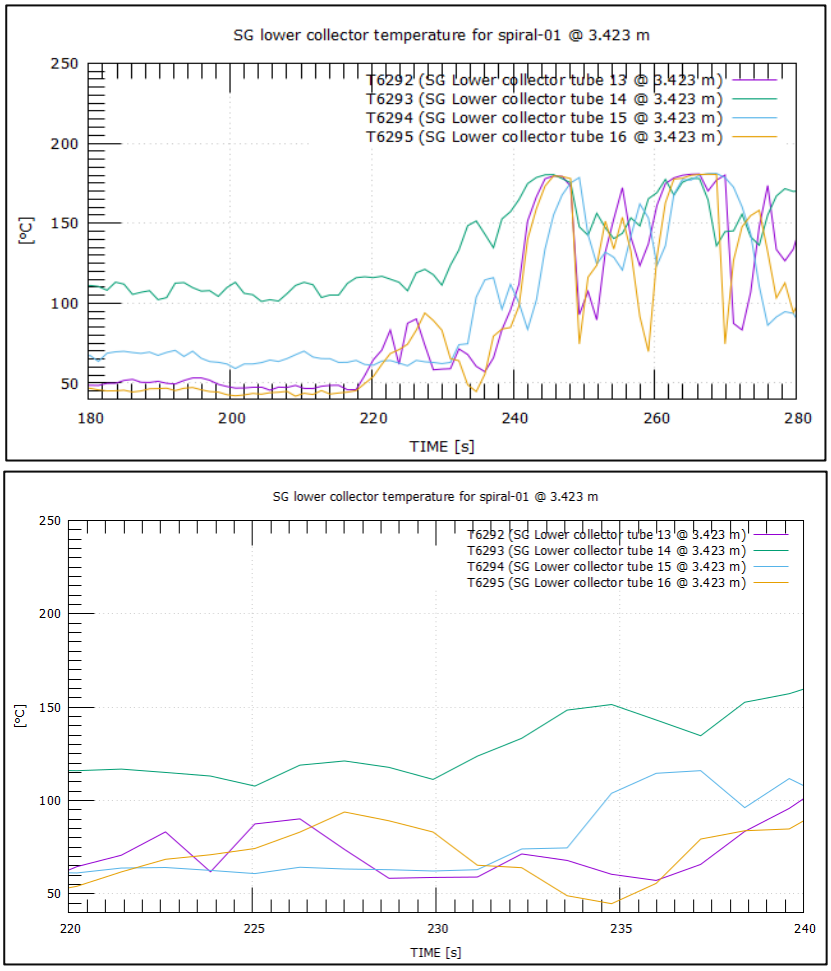

Figure 18:Tube temperature for Spiral-01 at 3.423 m for 180-280 sec (b) Tube temperature for Spiral-01 at 3.423 m for 220-240 sec (MS-SG01A)

The graph shows that both amplitude and period of oscillations vary at 3.423 m and 3.983 m. However, as elevation height increases, amplitude and period tend to be the same for all tubes under the same spiral group.

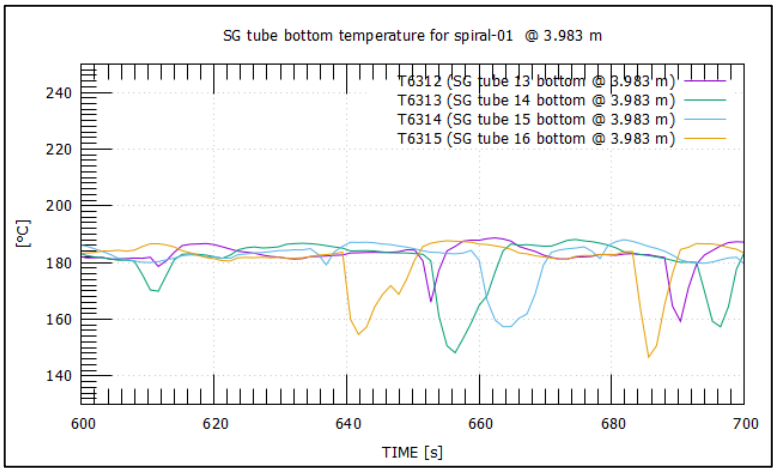

Figure 19:Tube temperature for Spiral-01 at 3.983 m for 600-700 sec (MS-SG01A)

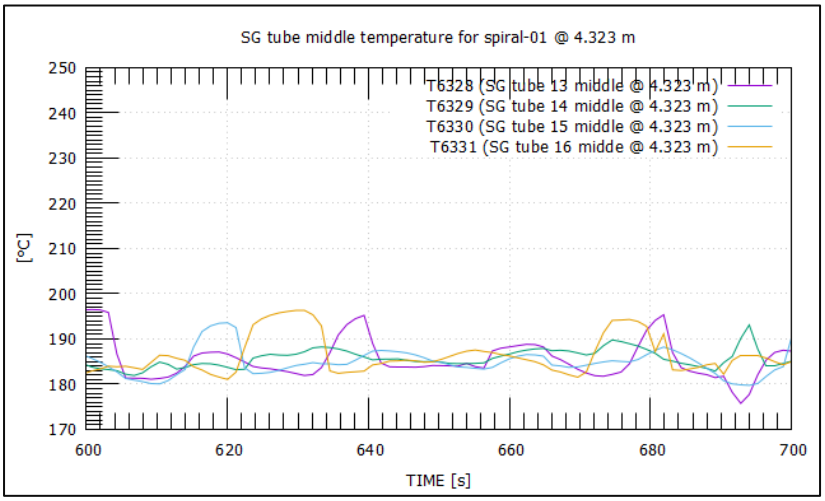

Figure 20:Tube temperature for Spiral-01 at 4.323 m for 600-700 sec (MS-SG01A)

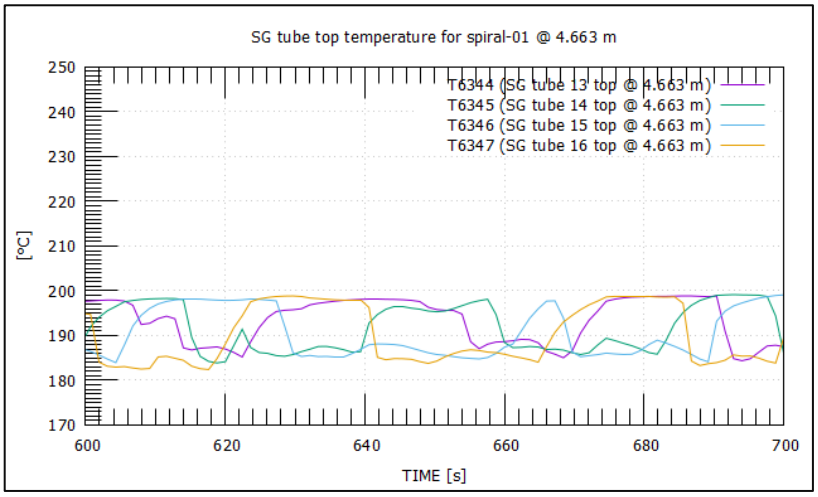

Figure 21: Tube temperature for Spiral-01 at 4.663 m for 600-700 sec (MS-SG01A)

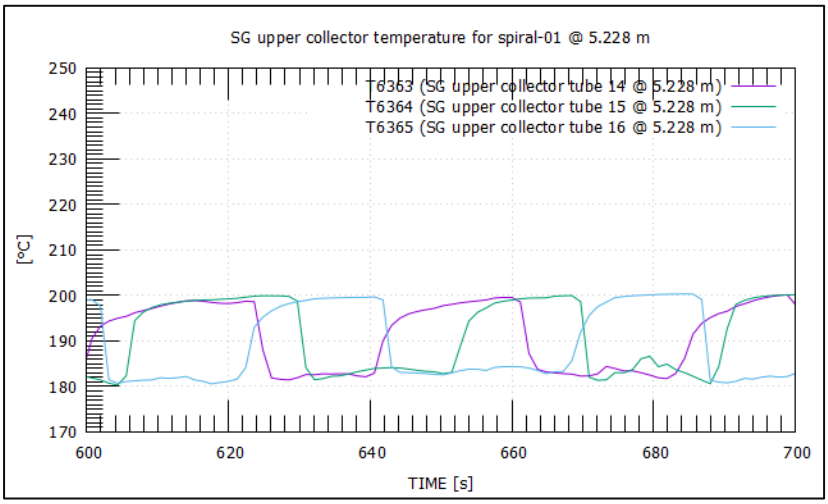

Figure 22:Tube temperature for Spiral-01 at 5.228 m for 600-700 seconds (MS-SG01A)

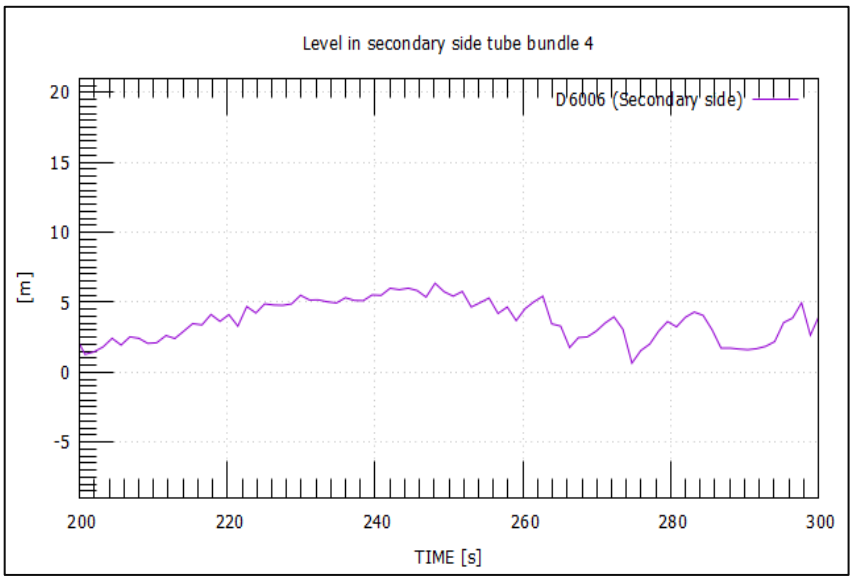

Figure 23: Level in secondary side tube bundle-04 for 200-300 seconds (MS-SG01A)

The increase in level inside bundle-04 can be attributed to increasing in core power. This level change pattern also introduced oscillations in tube temperature at the entry of the cold collector (3.423 m).

5.1.2 Study of MS-SG01B test results

For MS-SG01B experiment, during the start of 400, tube temperature at 3.323 m started to oscillate, and tubes 09 & 13 showed the highest amplitude compared to tubes 01 & 05. It showed the same pattern as MS-SG01A experiments, as tube 01 & 05 has lower mass flow rate and experience high superheating, which results in higher oscillatory behaviour. After some time, around 3000-3100 seconds oscillatory pattern became stable for tube temperature at 3.423 m. While the amplitude of the oscillations for tubes 01 & 05 is 100ºC, the amplitude for tubes 09 & 13 is around 150ºC. The period is the same for all tubes for tube temperature at 3.423 m ranging from 3000-3100 seconds.

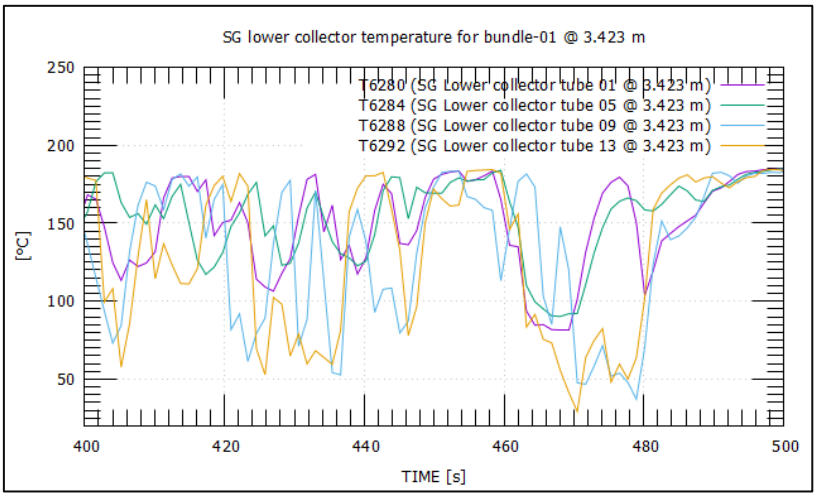

Figure 24: Tube temperature for Bundle-01 at 3.423 m for 400-500 sec (MS-SG01B)

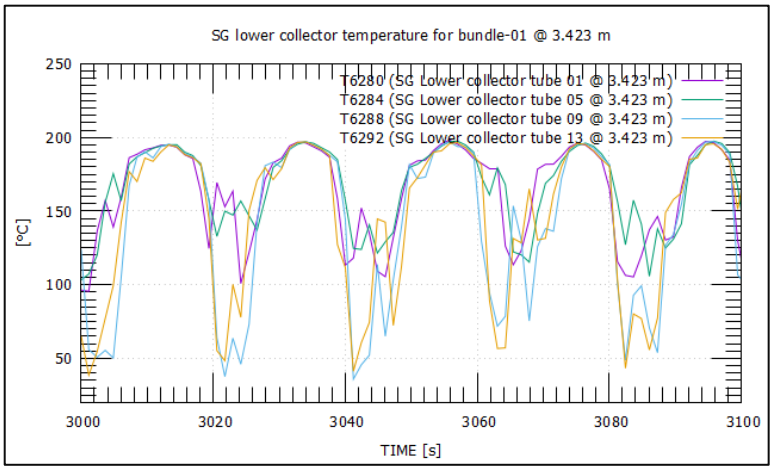

Figure 25:Tube temperature for Bundle-01 at 3.423 m for 3000-3100 sec (MS-SG01B)

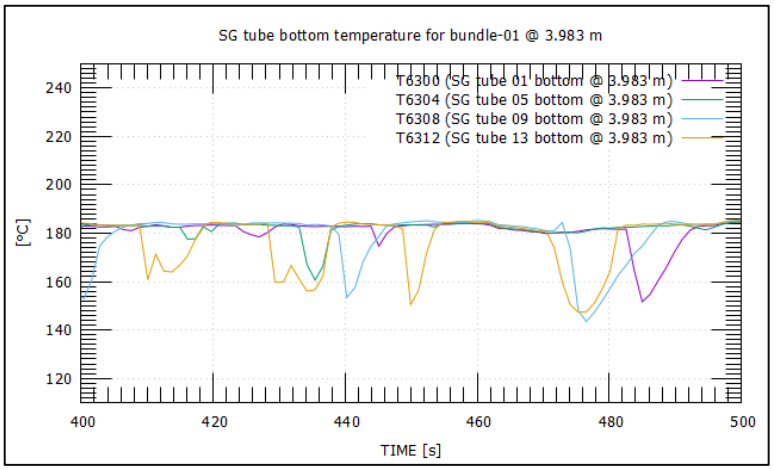

Figure 26: Tube temperature for Bundle-01 at 3.983 m for 400-500 sec (MS-SG01B)

Tube temperature at 3.983 m showed a maximum negative amplitude of around 40ºC for tubes 09 & 13 for the time range of 400-500 seconds which gets reversed at 3000-3100 seconds. At 3000-3100 seconds, tube temperature at 3.423 m showed high frequency and low amplitude, which is typical behaviour for density wave-type oscillations. As thermal oscillations typically happen due to pressure drop inside the tube, which also shows the same oscillatory behaviour, higher oscillations commonly result from higher frictional pressure drop, which is a strong function of mass flow rate. Hence, a tube with less mass flow rate (tubes -01 & 05) typically results in oscillatory behaviour with higher amplitude than the tube with a higher mass flow rate (tube-09 & 13). Oscillations amplitude also depends on heat or power input. So as a 1 MW power step was applied during MS-SG01B experiment oscillations amplitude of tube temperature at 3.423 m is higher in comparison to the MS-SG01A experiment, where a 750 kW power step was applied. Tube temperatures at 4.323 m, 4.663 m & 5.228 m for the time range of 400-500 seconds are almost the same (182ºC) with some oscillations with small amplitude. For the time range 3000-3100 seconds maximum temperature reaches up to 222ºC compared to the MS-SG01A experiment. Thermal oscillations amplitude is also higher (36~38ºC) compared to the previous MS-SG01A experiment (20ºC).

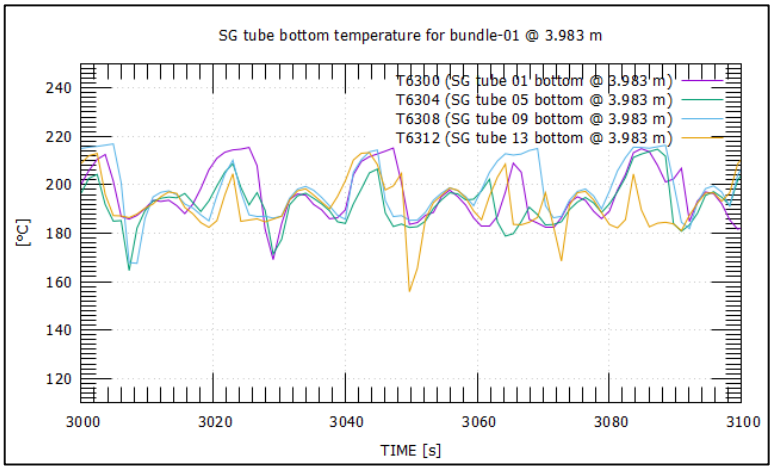

Figure 27: Tube temperature for Bundle-01 at 3.983 m for 3000-3100 sec (MS-SG01B)

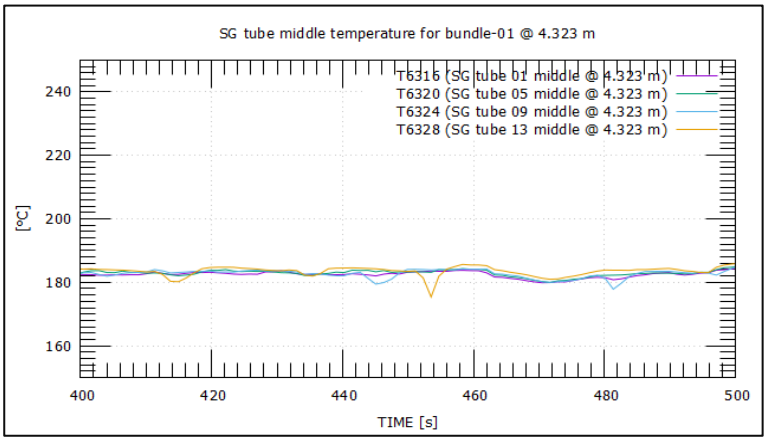

Figure 28:Tube temperature for Bundle-01 at 4.323 m for 400-500 sec (MS-SG01B)

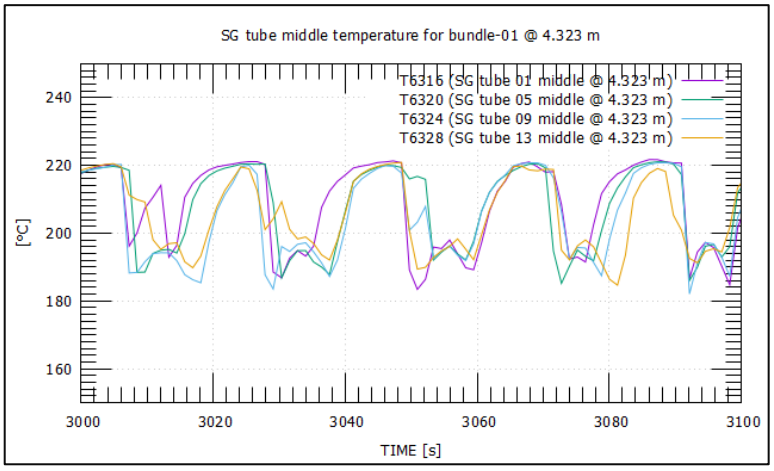

Figure 29:Tube temperature for Bundle-01 at 4.323 m for 3000-3100 sec (MS-SG01B)

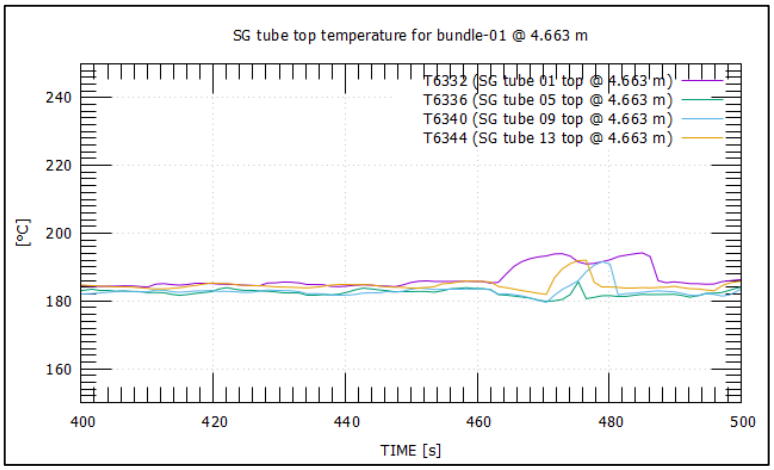

Figure 30: Tube temperature for Bundle-01 at 4.663 m for 400-500 sec (MS-SG01B)

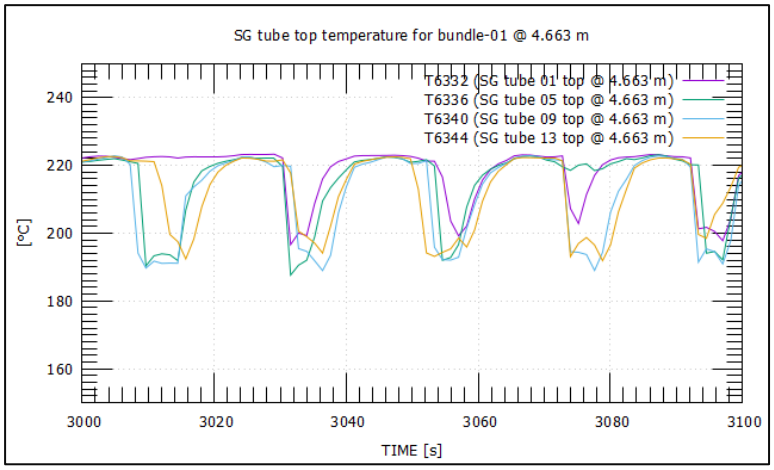

Figure 31:Tube temperature for Bundle-01 at 4.663 m for 3000-3100 sec (MS-SG01B)

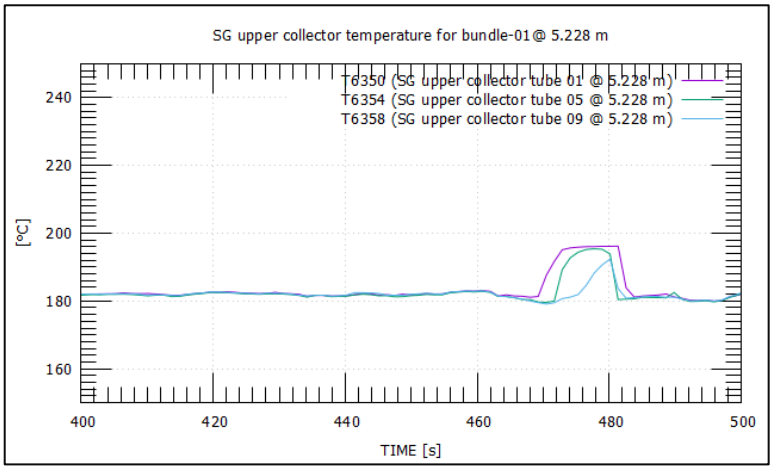

Figure 32:Tube temperature for Bundle-01 at 5.228 m for 400-500 sec (MS-SG01B)

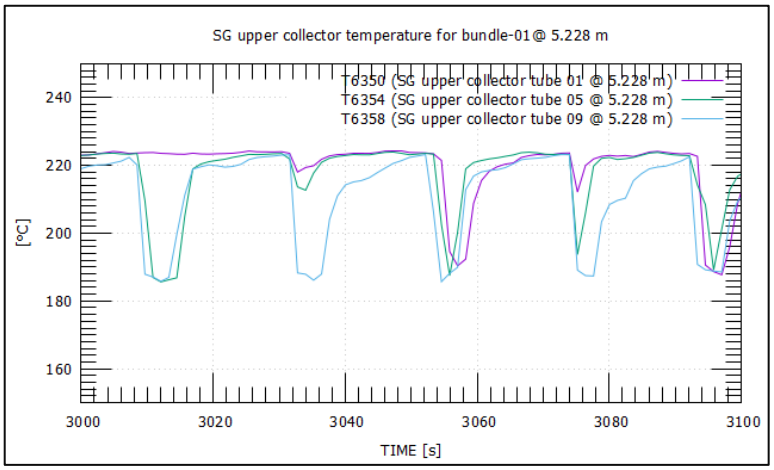

Figure 33: Tube temperature for Bundle-01 at 5.228 m for 3000-3100 sec (MS-SG01B)

Spiral Group-01 (same length & diameter)

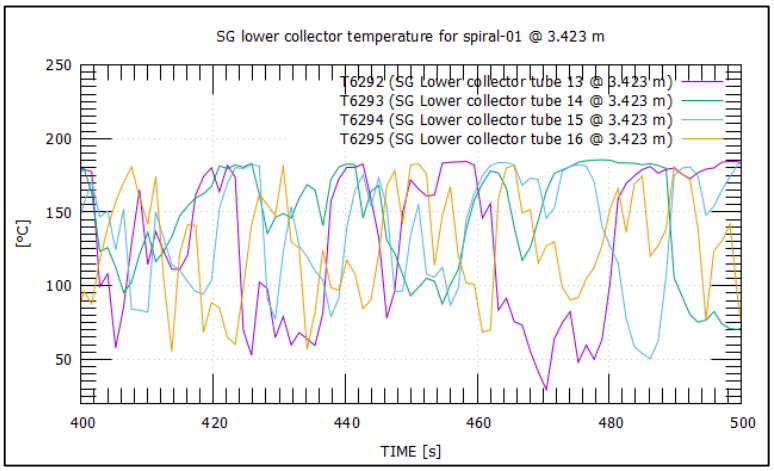

Figure 34: Tube temperature for Spiral-01 at 3.423 m for 400-500 sec (MS-SG01B)

The same spiral group tube temperature at 3.423 m showed an irregular pattern for oscillations during 400-500 seconds. For the time range of 3000-3100 seconds, tubes 13 & 14 showed an upward trend of oscillations at the same time (3000 seconds), while tubes 15 & 16 showed a downward pattern. While tube temperature at 3.983 m showed a regular oscillatory pattern for 400-500 seconds, tube temperature showed an irregular pattern for 3000-3100 seconds. For the other three locations, oscillations amplitude tends to increase with elevation height. While tube temperature at 4.323 m showed an oscillations amplitude of 24ºC, tube temperature at 4.663 m & 5.228 m showed an oscillations amplitude of approximately 28ºc and 38ºC. The oscillation period for tube temperature also increases with elevation height.

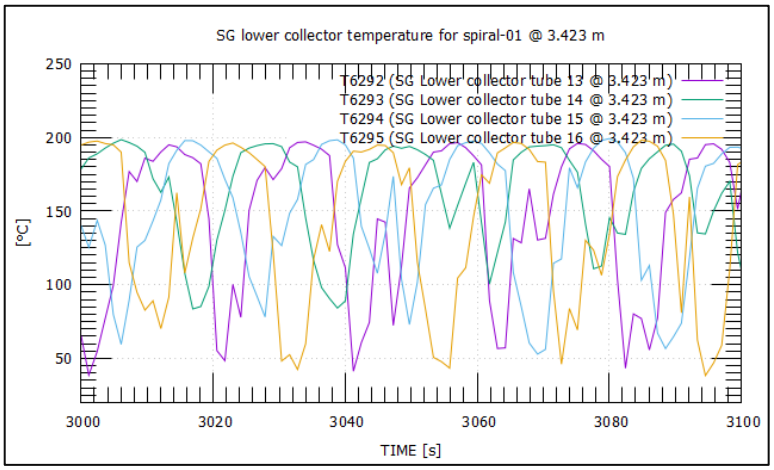

Figure 35: Tube temperature for Spiral-01 at 3.423 m for 3000-3100 sec (MS-SG01B)

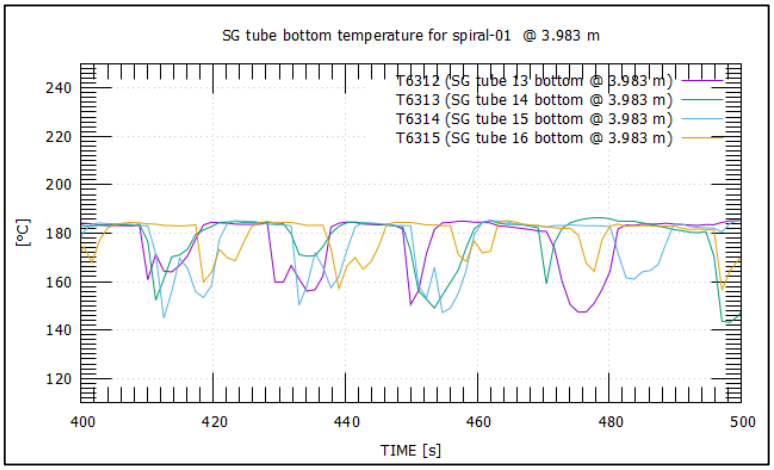

Figure 36: Tube temperature for Spiral-01 at 3.983 m for 400-500 sec (MS-SG01B)

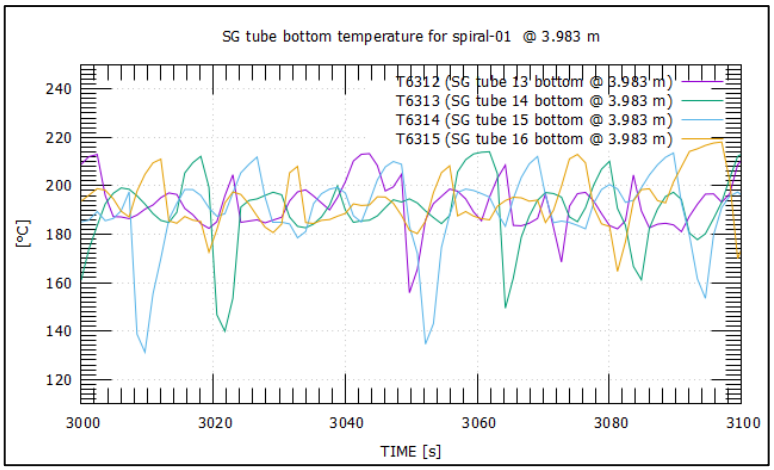

Figure 37:Tube temperature for Spiral-01 at 3.983 m for 3000-3100 sec (MS-SG01B)

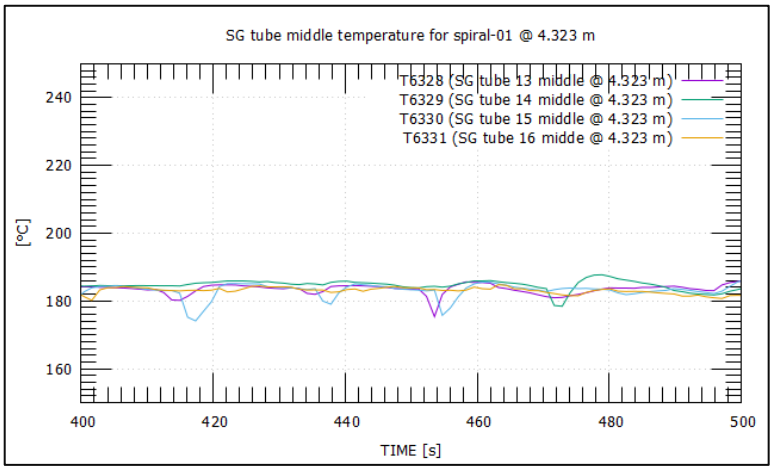

Figure 38: Tube temperature for Spiral-01 at 4.323 m for 400-500 sec (MS-SG01B)

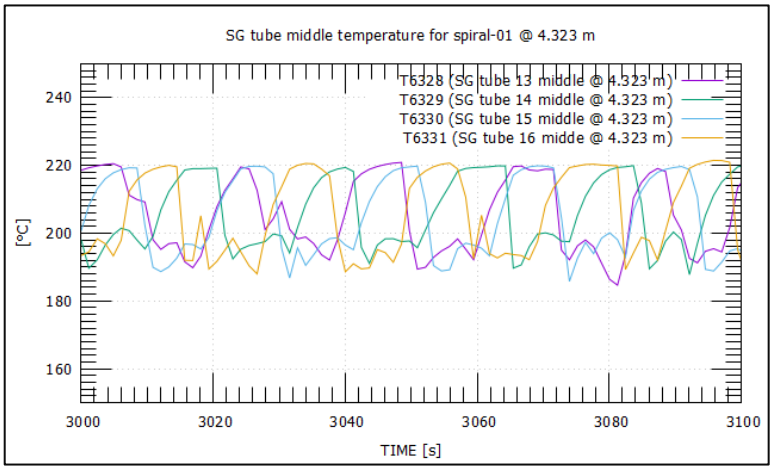

Figure 39: Tube temperature for Spiral-01 at 4.323 m for 3000-3100 sec (MS-SG01B)

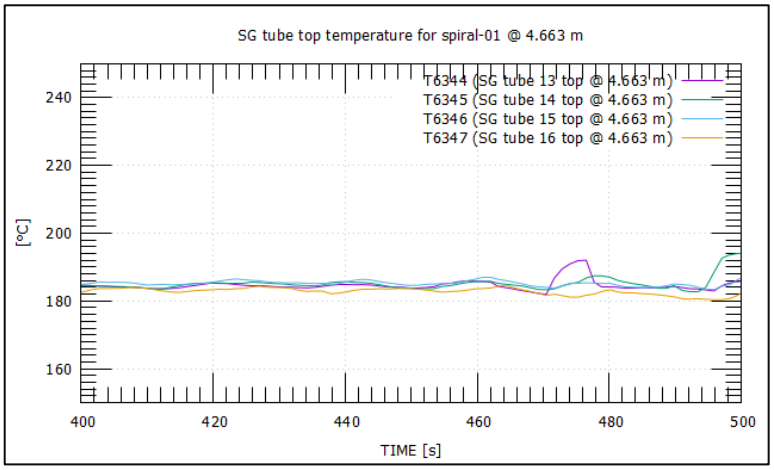

Figure 40: Tube temperature for Spiral-01 at 4.663 m for 400-500 sec (MS-SG01B)

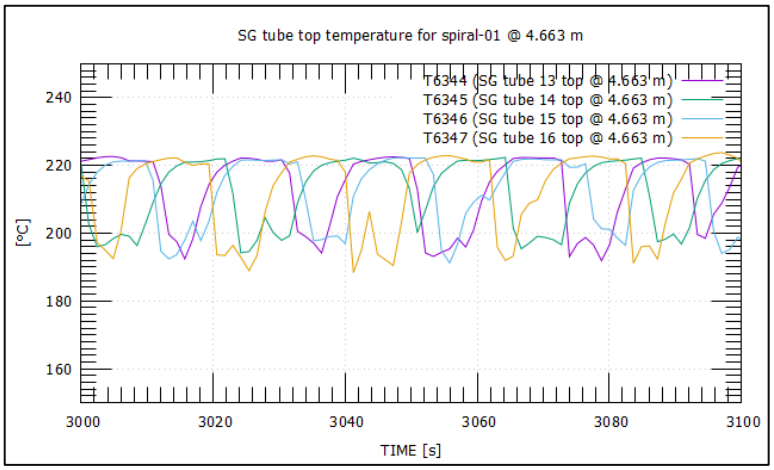

Figure 41: Tube temperature for Spiral-01 at 4.663 m for 3000-3100 sec (MS-SG01B)

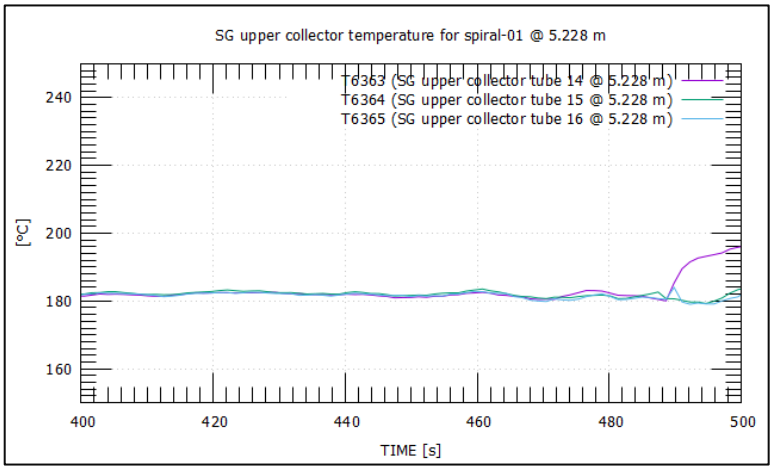

Figure 42: Tube temperature for Spiral-01 at 5.228 m for 400-500 sec (MS-SG01B)

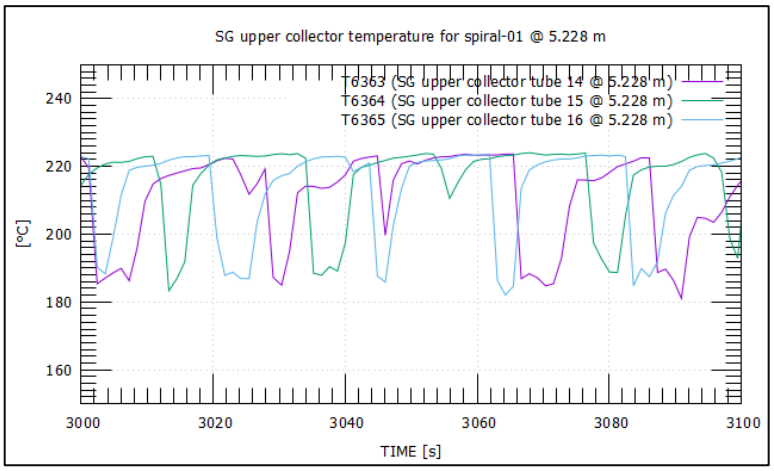

Figure 43: Tube temperature for Spiral-01 at 5.228 m for 3000-3100 sec (MS-SG01B)

5.1.3 Study of MS-SG01R test results

Bundle-01

Because of the 250 kW power step at 1500 seconds, bundle-01 tube temperature started to oscillate. Though all oscillation has a maximum temperature of 180ºC, each tube has a different amplitude for oscillations. While tube-01 has an amplitude of approximately 30ºC, tube-05, tube-09, and tube-13 have an amplitude of 40ºC, 105ºc, and 120ºc. The as long tube has low mass flow, and the high superheating amplitude is higher than the shorter tube, as expected and shown in earlier graphs also. However, when a higher power step of 500 kW was applied for 5100 seconds, tube-01 & 05 started to oscillate in the same manner with the same amplitude, and the oscillations period increased. The same trend was also observed for tubes 09 & 13. Temperature for tube-01 & 05 did not drop below 100ºC, while for tubes 09 & 13 it occasionally dropped below 100ºC. After some time, at around 6000-6100 seconds oscillation period increase to 20 seconds. The maximum temperature of oscillations is 180ºC, and the amplitude of oscillations is 130ºC for tubes 09 & 13, and for tubes 01 & 05 it is 80ºC. Tube temperature at 3.983 m did not show a significant oscillatory pattern even though sufficient time (1800-2000 seconds and 6000-6100 seconds) passed after the power step. A possible reason can be turbulence and secondary motion after entry inside the tube, which increased stability. The same temperature was observed at 4.323 m, 4.663 m, and 5.228 m for 1800-2000 seconds when 250 kW power step was applied. On the contrary to that, when 500 kW power step was applied, oscillations started to be visible at those locations. It was observed that both oscillations maximum temperature and period increase with elevation height. Oscillation maximum temperature increases by approximately 2ºc with elevation height.

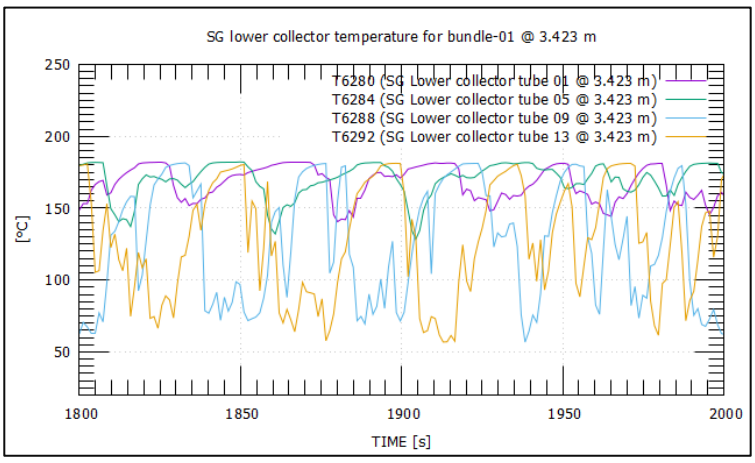

Figure 44: Tube temperature for Bundle-01 at 3.423 m for 1800-2000 sec (MS-SG01R)

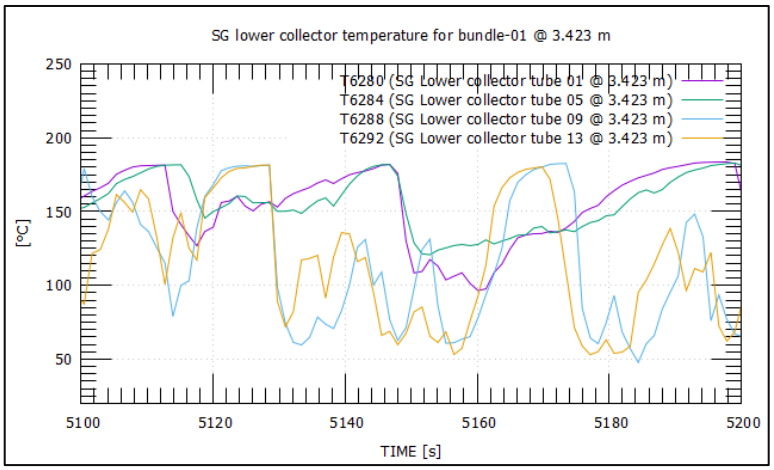

Figure 45: Tube temperature for Bundle-01 at 3.423 m for 5100-5200 sec (MS-SG01R)

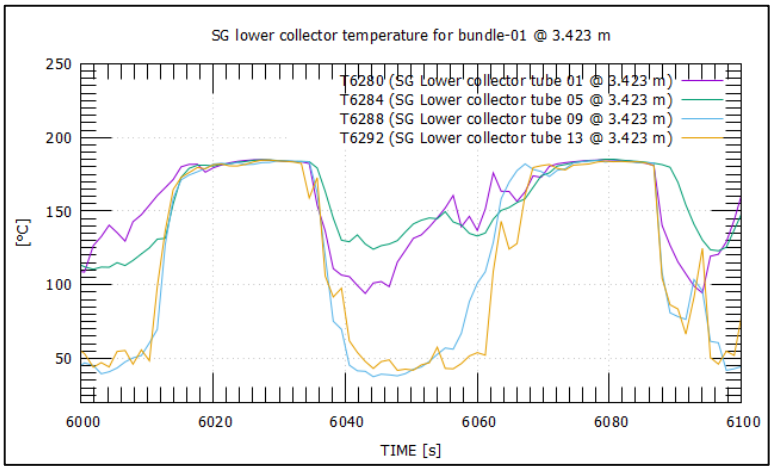

Figure 46: Tube temperature for Bundle-01 at 3.423 m for 6000-6100 sec (MS-SG01R)

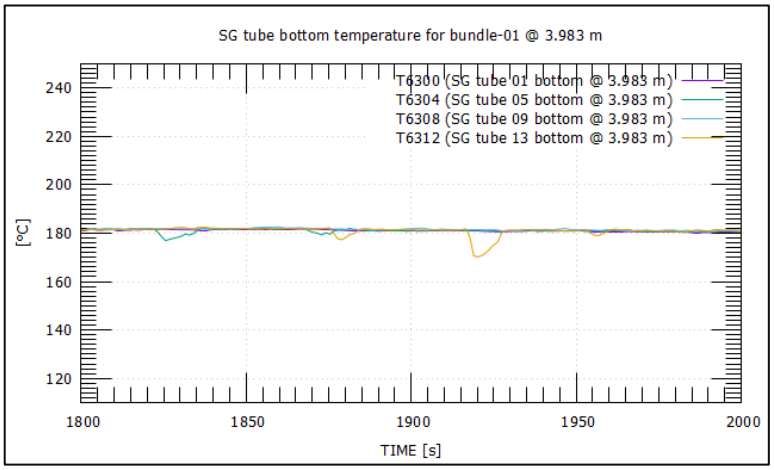

Figure 47: Tube temperature for Bundle-01 at 3.983 m for 1800-2000 sec (MS-SG01R)

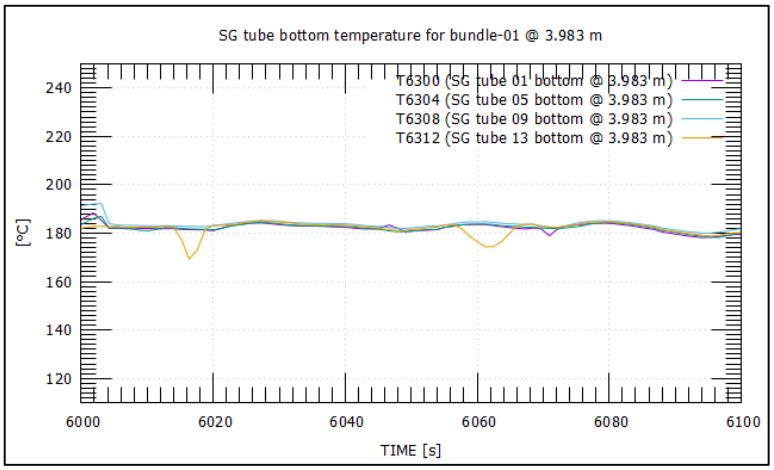

Figure 48: Tube temperature for Bundle-01 at 3.983 m for 6000-6100 sec (MS-SG01R)

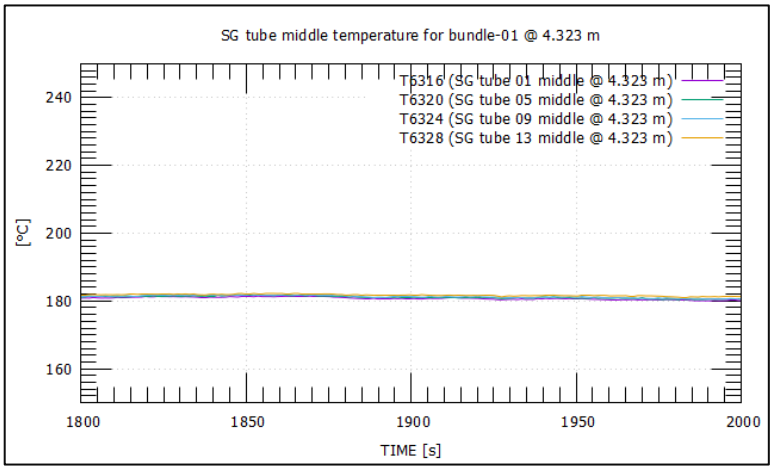

Figure 49: Tube temperature for Bundle-01 at 4.323 m for 1800-2000 sec (MS-SG01R)

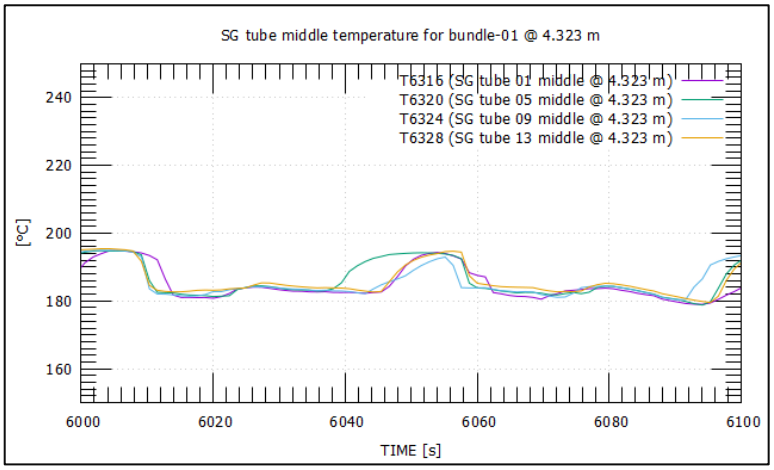

Figure 50: Tube temperature for Bundle-01 at 3.983 m for 6000-6100 sec (MS-SG01R)

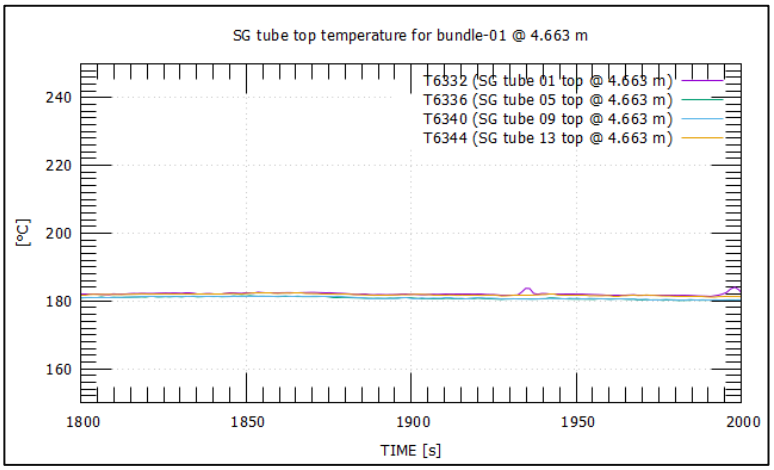

Figure 51: Tube temperature for Bundle-01 at 4.663 m for 1800-2000 sec (MS-SG01R)

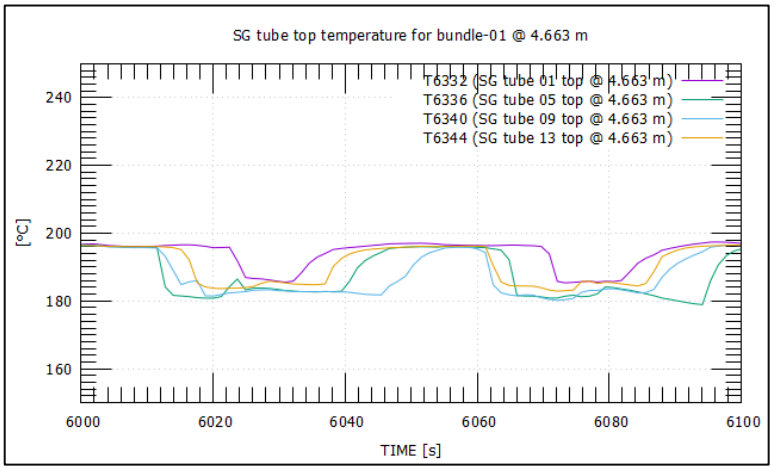

Figure 52: Tube temperature for Bundle-01 at 4.663 m for 6000-6100 sec (MS-SG01R)

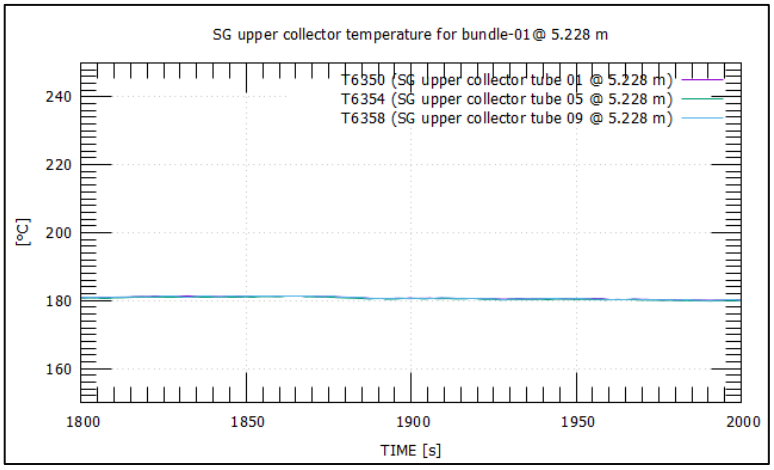

Figure 53: Tube temperature for Bundle-01 at 5.228 m for 1800-2000 sec (MS-SG01R)

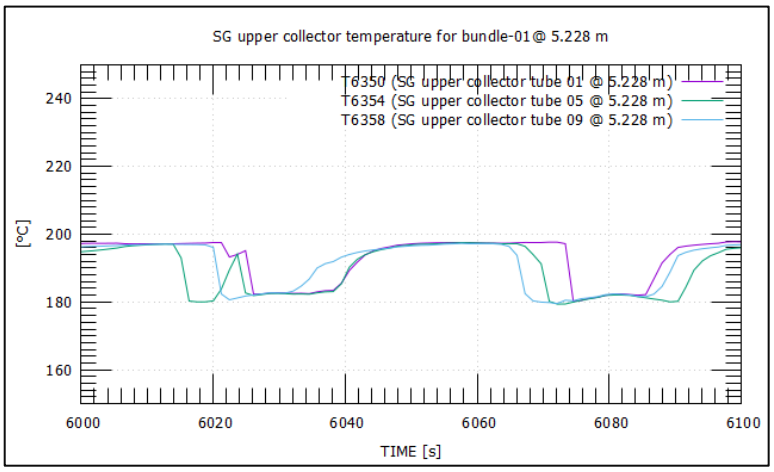

Figure 54: Tube temperature for Bundle-01 at 5.228 m for 6000-6100 sec (MS-SG01R)

Spiral-01

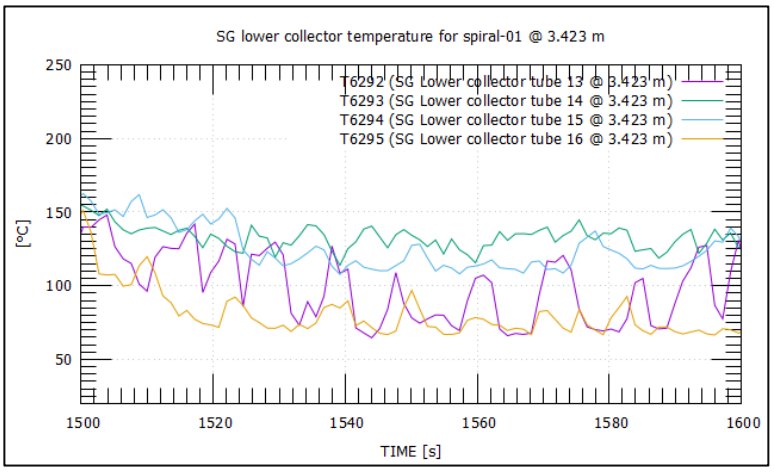

Figure 55: Tube temperature for Spiral-01 at 3.423 m for 1500-1600 sec (MS-SG01R)

The spiral group-01 tube-13 temperature oscillates more than the other three tube temperatures at a 3.423 m location. For the 4.323 m & 4.663 m locations, tube-15 temperature oscillations were followed by tube-14, 13 & 16. But for the 5.228 m location, this oscillations sequence changed, and tube-16 temperature oscillations were followed by tube-15 & tube-14.

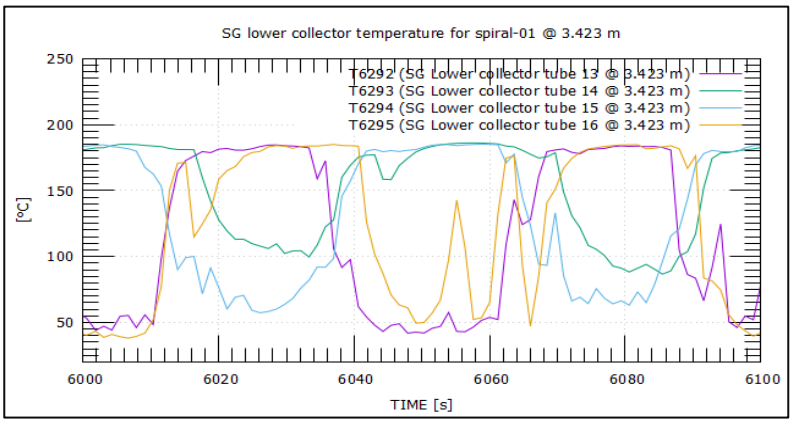

Figure 56: Tube temperature for Spiral-01 at 3.423 m for 6000-6100 sec (MS-SG01R)

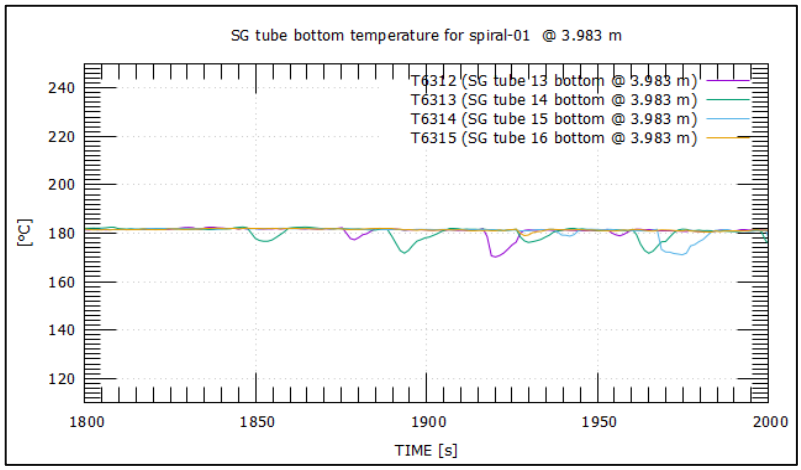

Figure 57: Tube temperature for Spiral-01 at 3.983 m for 1800-2000 sec (MS-SG01R)

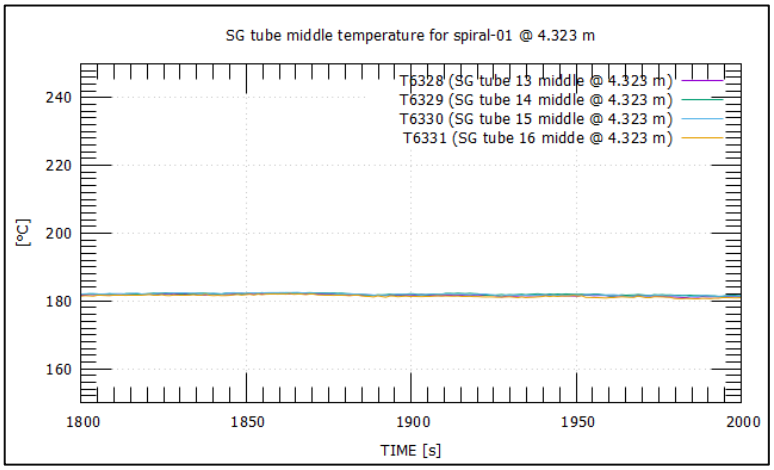

Figure 58: Tube temperature for Spiral-01 at 4.423 m for 1500-1600 sec (MS-SG01R)

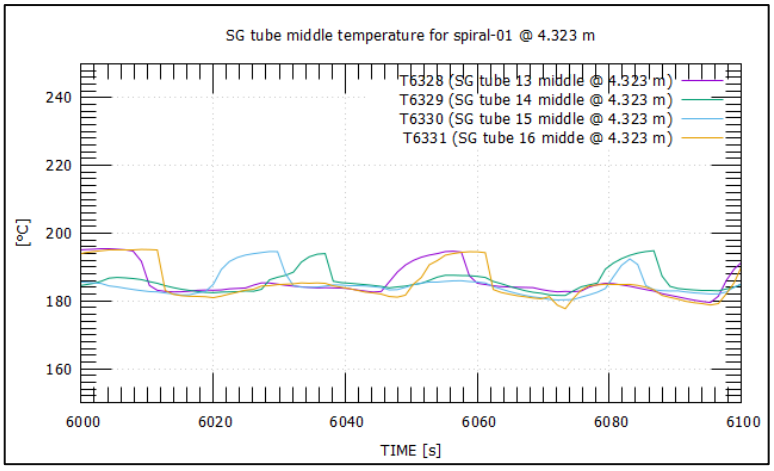

Figure 59: Tube temperature for Spiral-01 at 4.423 m for 6000-6100 sec (MS-SG01R)

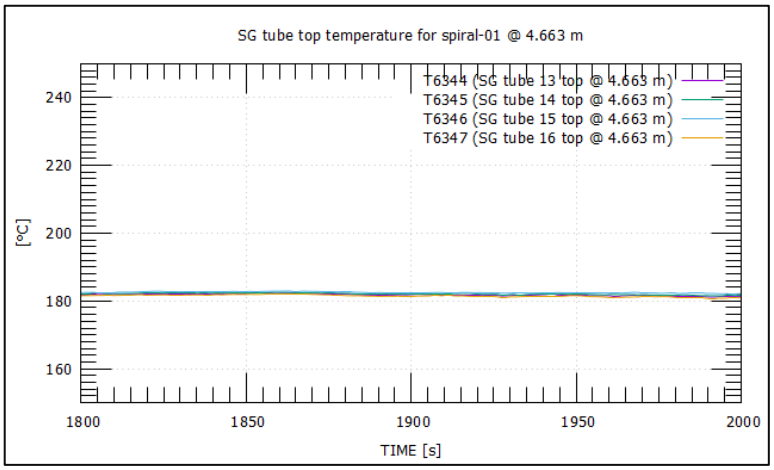

Figure 60: Tube temperature for Spiral-01 at 4.663 m for 1800-2000 sec (MS-SG01R)

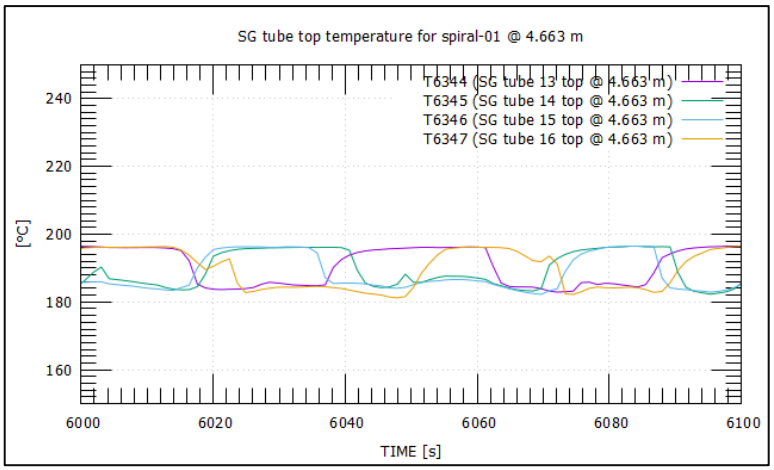

Figure 61: Tube temperature for Spiral-01 at 4.663 m for 6000-6100 sec (MS-SG01R)

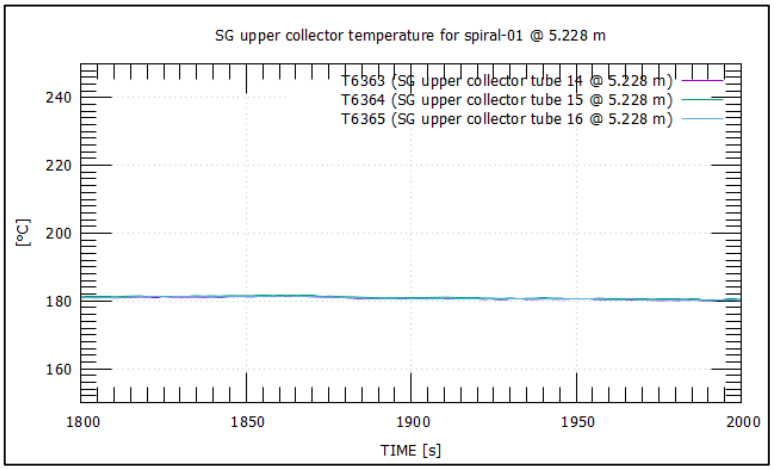

Figure 62: Tube temperature for Spiral-01 at 5.228 m for 1800-2000 sec (MS-SG01R)

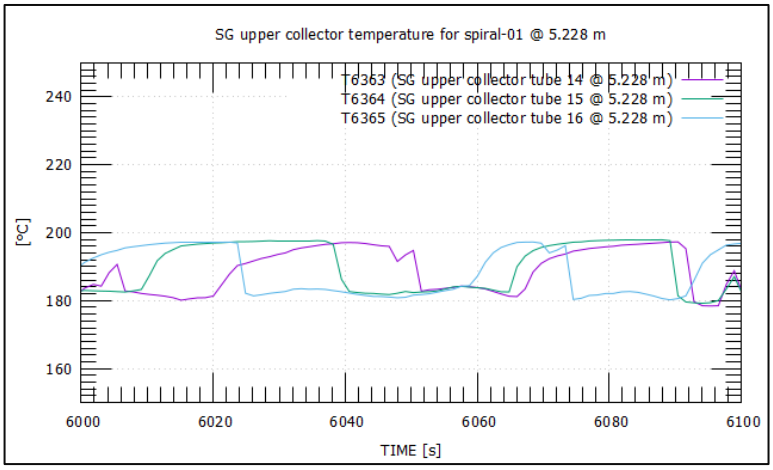

Figure 63: Tube temperature for Spiral-01 at 3.423 m for 6000-6100 sec (MS-SG01R)

5.1.4 Study of MS-SG02 test results

Normal Heating

Bundle-01

Power step of 100 kW, 125 kW & 150 kW was applied at 3600-3700 seconds, 7200-7300 seconds, and 10800-10900 seconds accordingly. Tube-09 & 13 showed higher oscillations than tubes-01 & 05 as in the previous experiment. Oscillations amplitude also increased with the power step, as shown in the graph. Another critical observation is that the temperature did not go below 100ºC for all power steps, and for tubes 09 &13, the temperature was consistently above 150ºC. For all power steps, tube temperature at 3.983 m, 4.323 m, 4.983 m & 5.228 m is almost fixed (180ºC) even after sufficient time is passed. Only one graph (Figure 68) is shown here to avoid the repetitiveness of results. The reason for the stability of tube temperature at 3.983 m and upper location is low power and reasonably high mass flow rate. Any oscillation is a strong function of the power step and mass flow rate. When increasement of mass flow rate is proportional to the power, step tube temperature becomes stable and almost constant.

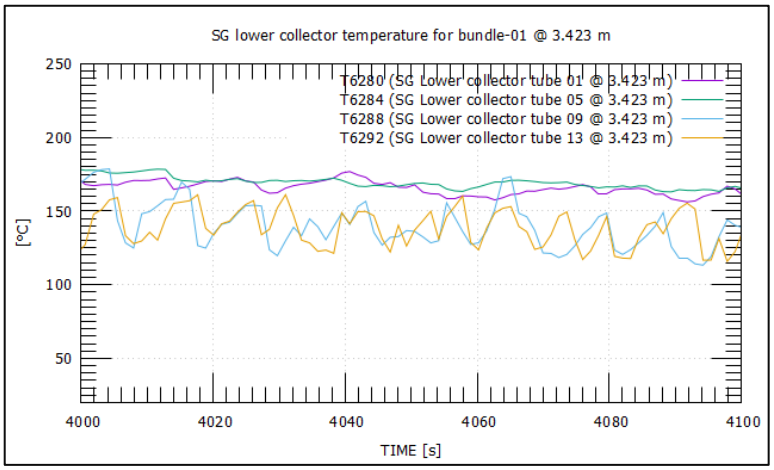

Figure 64: Tube temperature for bundle-01 at 3.423 m for 4000-4100 sec (MS-SG02)

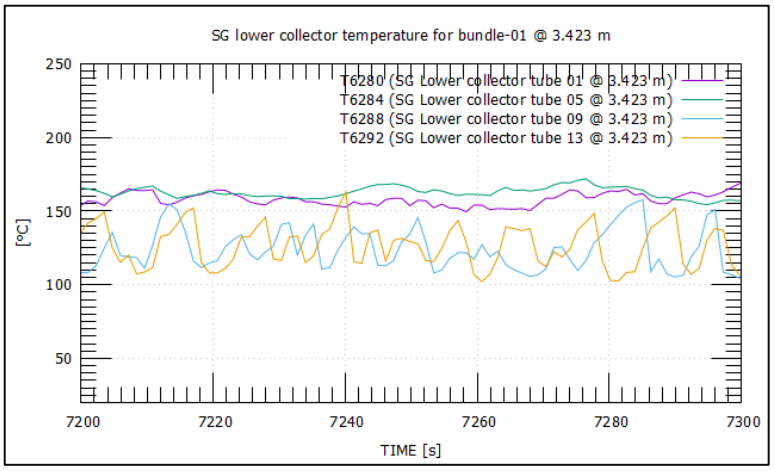

Figure 65: Tube temperature for bundle-01 at 3.423 m for 7200-7300 sec (MS-SG02)

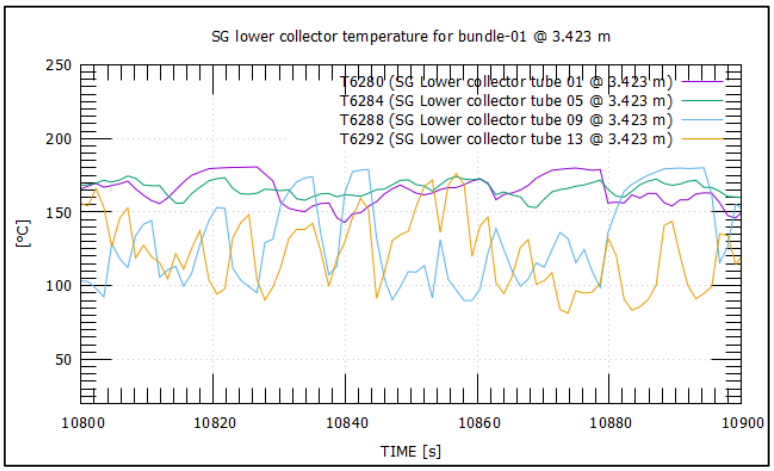

Figure 66: Tube temperature for bundle-01 at 3.423 m for 10800-10900 sec (MS-SG02)

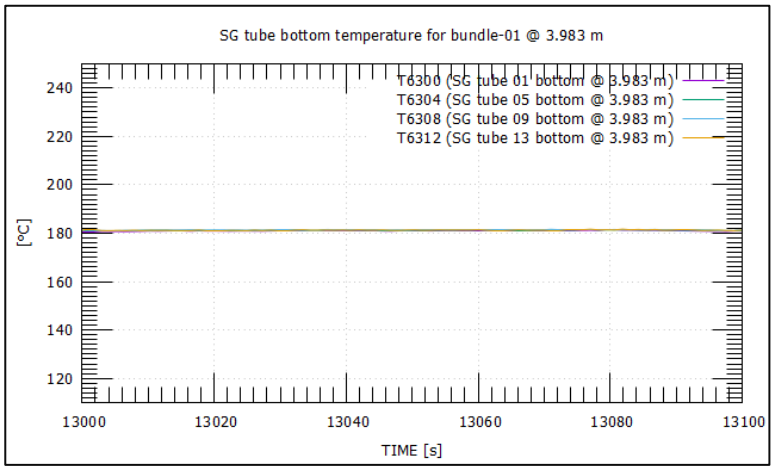

Figure 67: Tube temperature for bundle-01 at 3.983 m for 13000-13100 sec (MS-SG02)

Spiral-01

For the same spiral group, all tube temperature at 3.423 m oscillates unevenly. For 3.983 m, 4.323 m, 4.983 m & 5.228 m, the tube temperature is the same for all power steps.

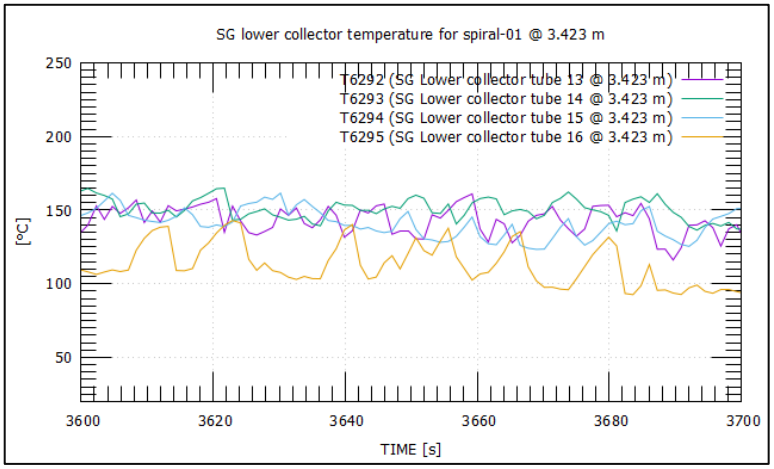

Figure 68: Tube temperature for Spiral-01 at 3.423 m for 3600-3700 sec (MS-SG02)

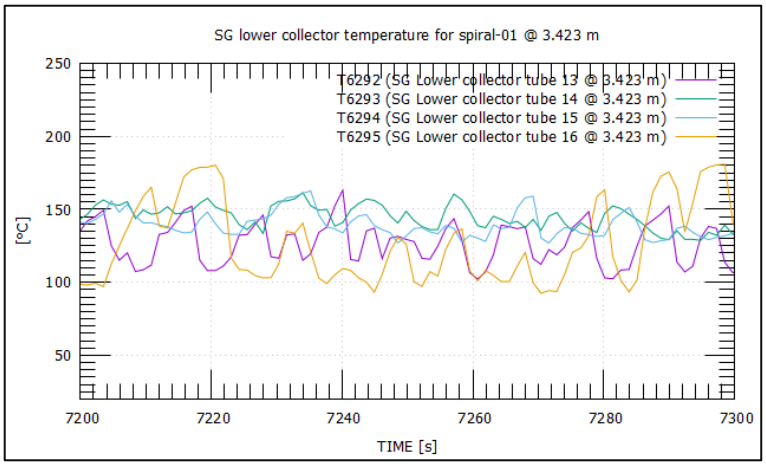

Figure 69: Tube temperature for Spiral-01 at 3.423 m for 7200-7300 sec (MS-SG02)

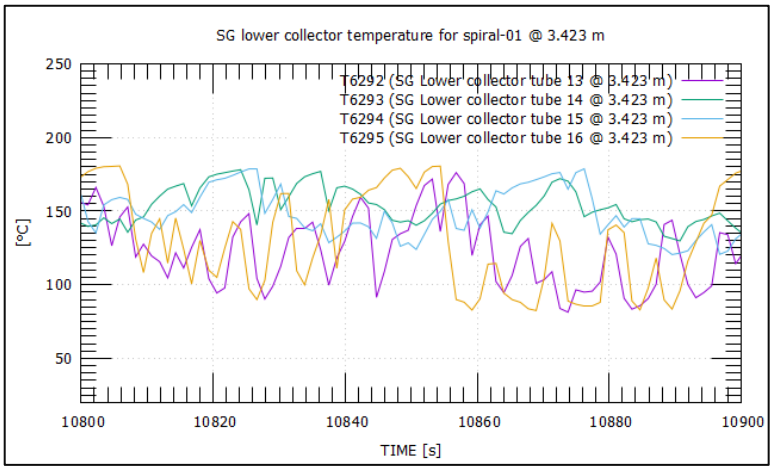

Figure 70: Tube temperature for Spiral-01 at 3.423 m for 10800-10900 sec (MS-SG02)

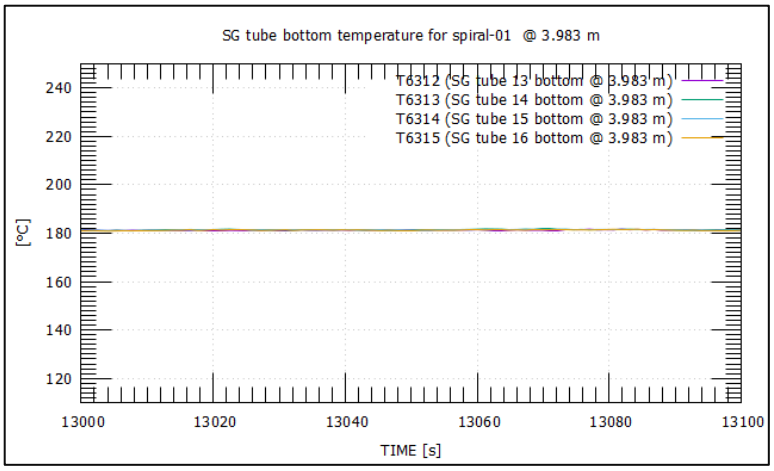

Figure 71: Tube temperature for Spiral-01 at 3.983 m for 13000-13100 sec (MS-SG02)

5.1.5 Study of MS-SG03 test results

Bundle-04

Tube Temperature is below 100ºC at 3.423 m before and after the power step 50 kW applied for 200-300 seconds and 300-400 seconds. This is because water does not vaporize into steam for low power and sufficient high mass flow. When the power step was increased to 100 kW, the temperature started to oscillate with high amplitude between 50º C and 150ºC, indicating the formation of the two-phase mixture. For 6700-6800 seconds, 9700-9800 seconds, and 12700-12800 seconds duration, high amplitude thermal oscillations converted to low amplitude and high-frequency oscillations. Temperature is above 100ºC, indicating pure steam inside the tube because of high heat transfer at an elevated height.

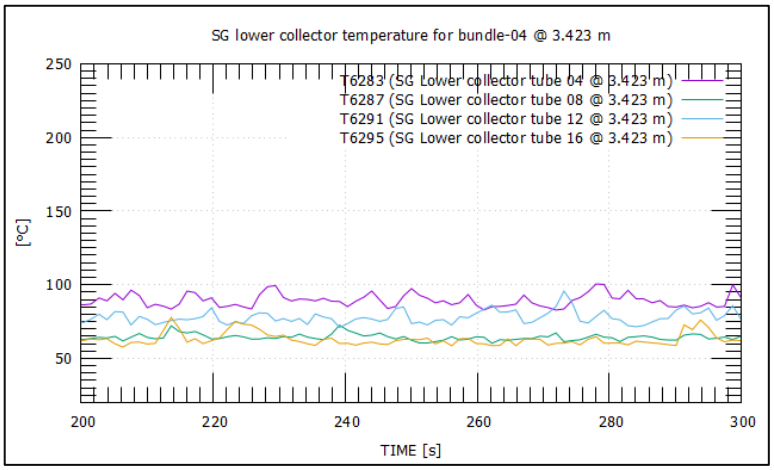

Figure 72: Tube temperature for bundle-04 at 3.423 m before power 50 kW

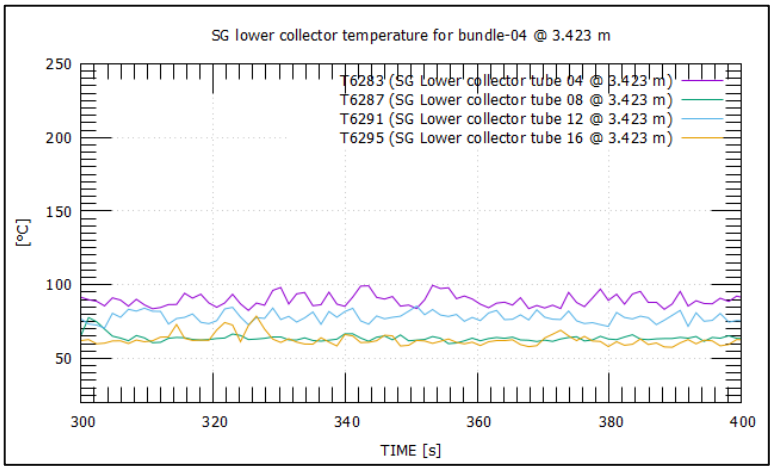

Figure 73: Tube temperature for bundle-04 at 3.423 m after power 50 kW

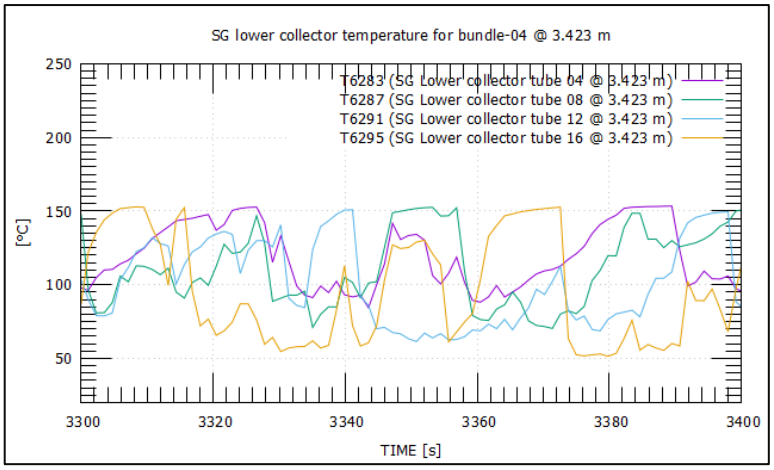

Figure 74: Tube temperature for bundle-04 at 3.423 m after power 100 kW

For the 3.983 m location, the tube temperature is almost constant (146ºC) due to low power, and no oscillations were observed. When the power step was increased to 100 kW at 5500-5600 seconds

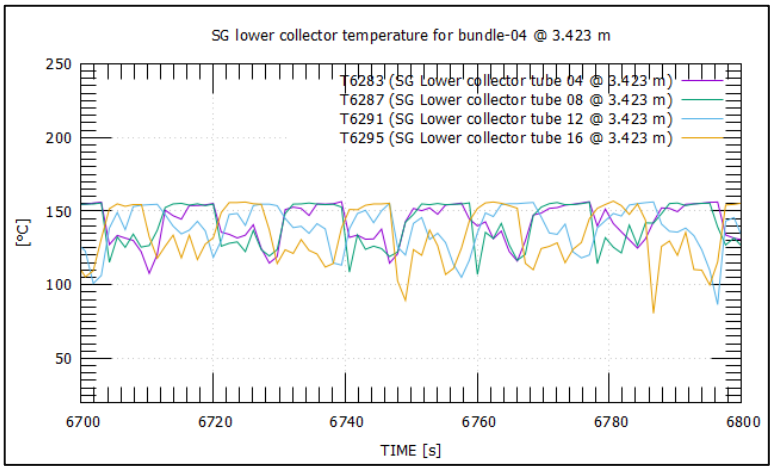

Figure 75: Tube temperature for bundle-04 at 3.423 m after 150 kW power step

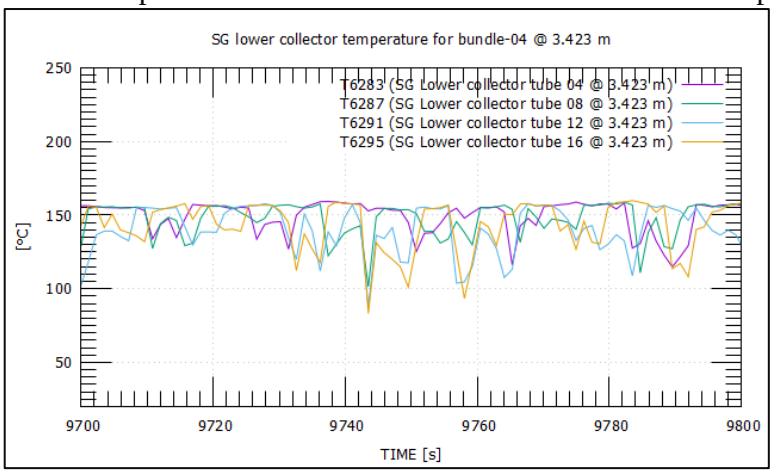

Figure 76: Tube temperature for bundle-04 at 3.423 m after 200 kW power step

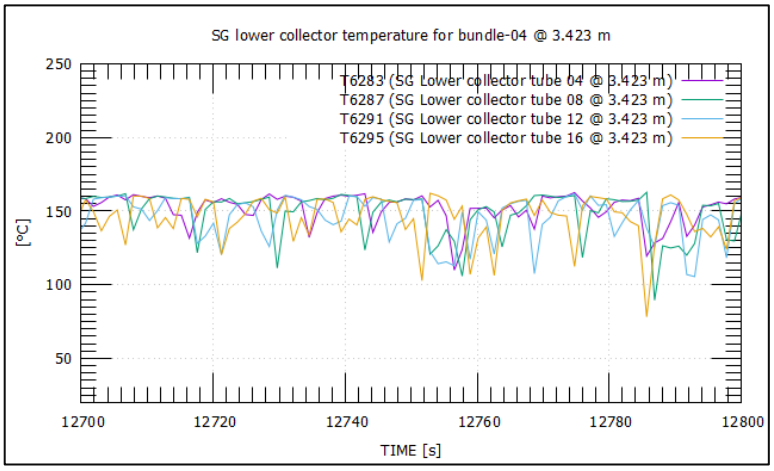

Figure 77: Tube temperature for bundle-04 at 3.423 m after 250 kW power step

Oscillations with small negative amplitude and a maximum temperature of around 156º were observed. When the power step was further increased to 150 kW, both the maximum temperature of oscillations (158ºC) and frequency were also increased.

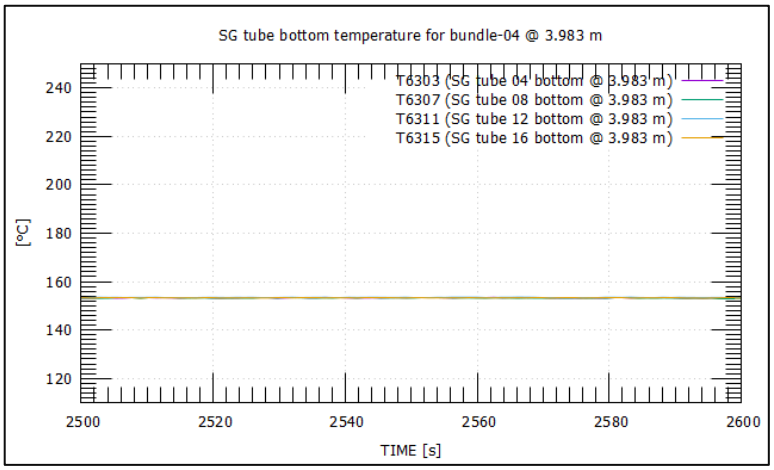

Figure 78: Tube temperature for bundle-04 at 3.983 m after 50 kW power step

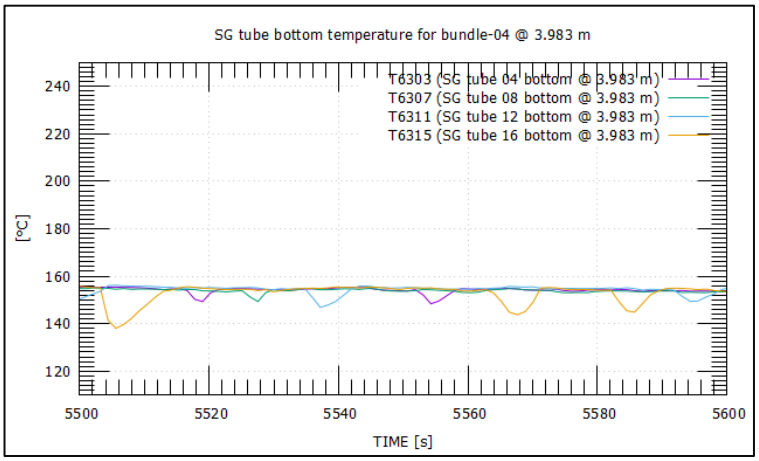

Figure 79: Tube temperature for bundle-04 at 3.983 m after 100 kW power step

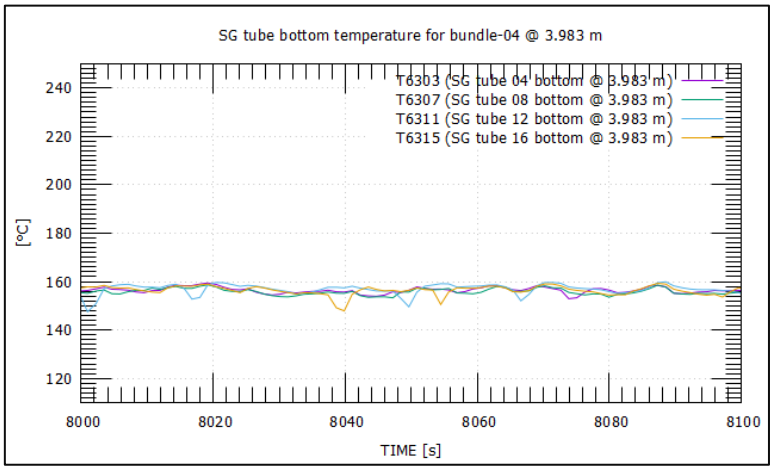

Figure 80: Tube temperature for bundle-04 at 3.983 m after 150 kW power step

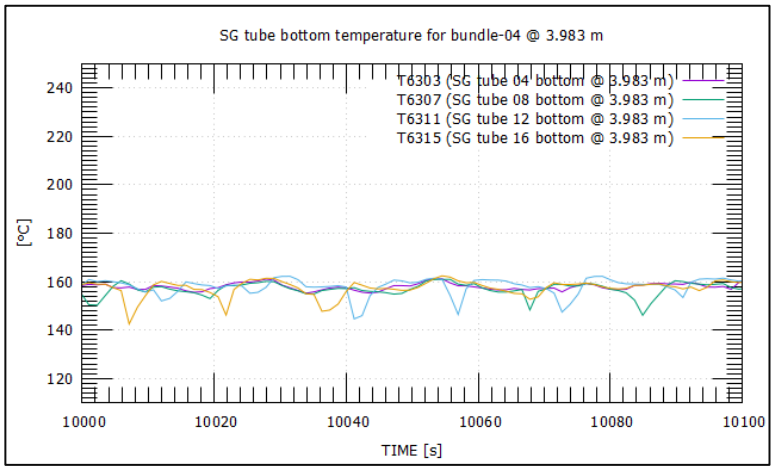

Figure 81: Tube temperature for bundle-04 at 3.983 m after 200 kW power step

For the 4.323 m location, an increase of power step results in oscillations in tube temperature but with minimal amplitude and high frequency. All tube temperature oscillates in the same manner. This incident can be due to the reason for operating only one bundle during operation. Higher flow inside one bundle makes the behaviour more stable and less oscillatory for the same power step compared to the previous experiment.

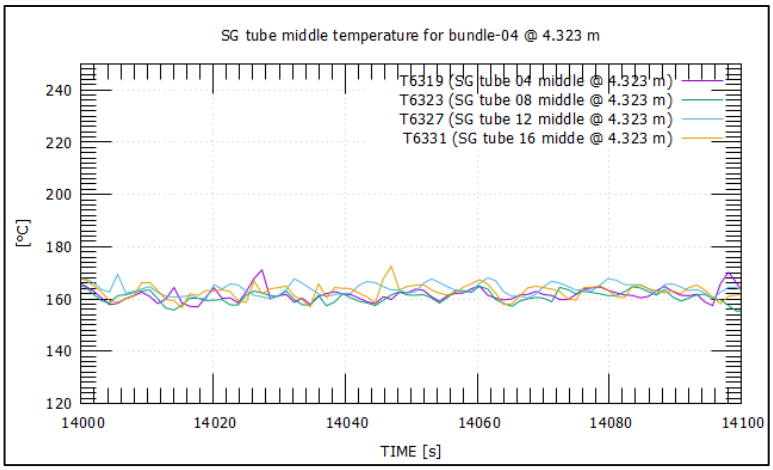

Figure 82: Tube temperature for bundle-04 at 4.323 m after 250 kW power step

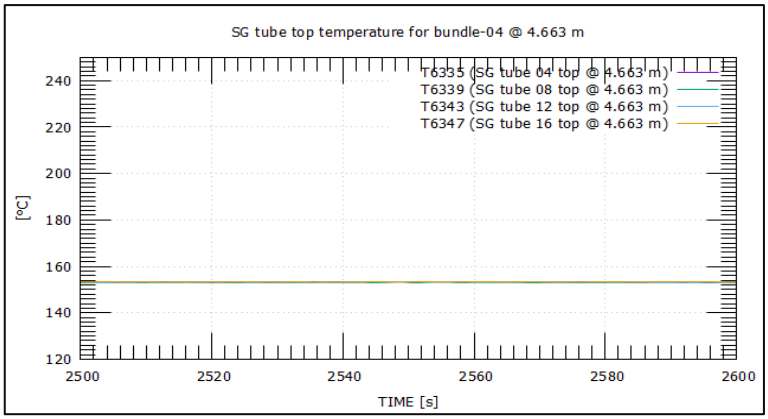

Figure 83: Tube temperature for bundle-04 at 4.663 m after 50 kW power step

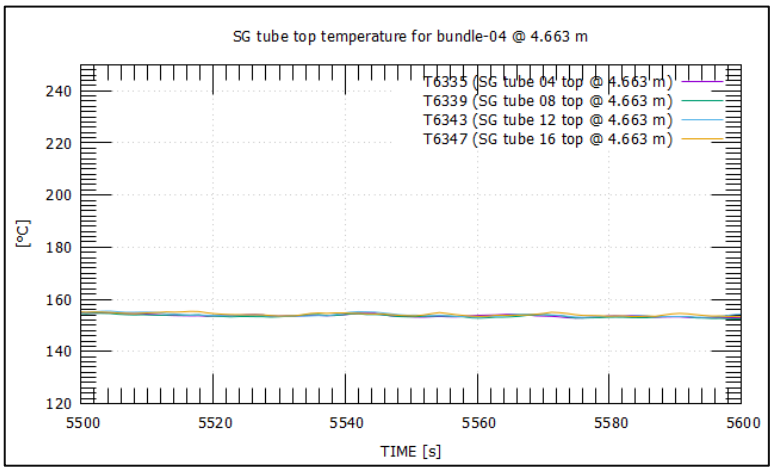

Figure 84: Tube temperature for bundle-04 at 4.663 m after 100 kW power step

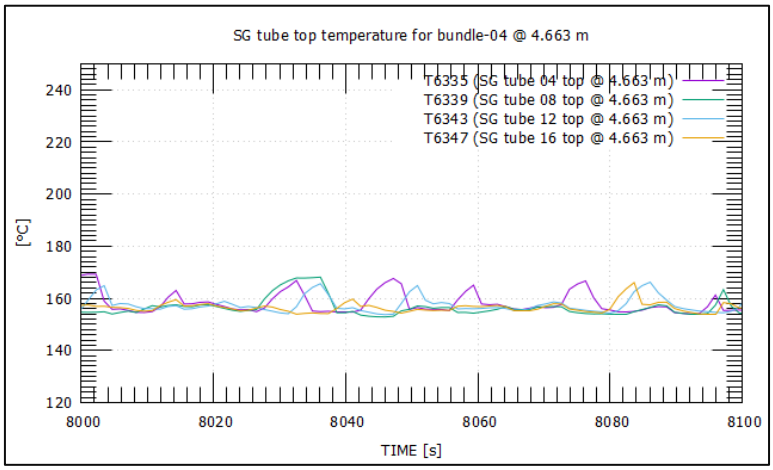

Figure 85: Tube temperature for bundle-04 at 4.663 m after 150 kW power step

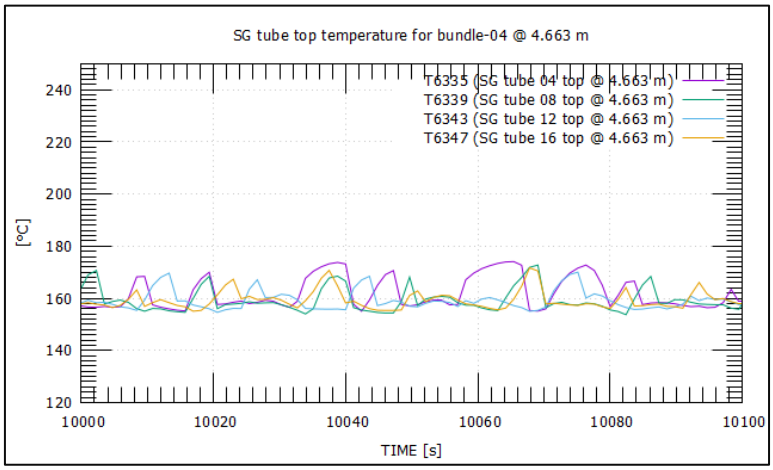

Figure 86: Tube temperature for bundle-04 at 4.663 m after 200 kW power step

For the 4.663 m location, even after the power step of 50 kW and 100 kW temperature is approximately the same (156ºC) and has no oscillations. For low power and higher mass flow rate, the temperature is stable. When the power step was increased to 200 kW & 250 kW temperature started to oscillate, but the oscillation amplitude was smaller compared to

previous tests where the same power step was also applied. As only bundle-04 was operating with a higher mass flow rate, it increased the stability.

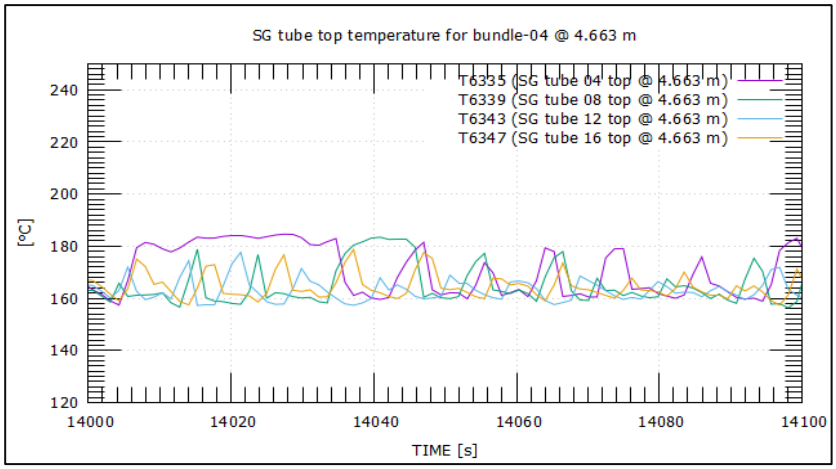

Figure 87: Tube temperature for bundle-04 at 4.663 m after 250 kW power step

For the 5.228 m location when the 50 kW power step was applied tube temperature did not change and was stable. When the power step was increased to 100 kW, oscillations of temperature started to happen inside the tube. Tube-04 showed oscillations with the highest amplitude compared to other tubes as it has a higher length, which ensures high superheating and less mass flow rate. Tube temperature at 5.228 m did not oscillate that much for tube-12 and tube-16 until the 250 kW power step was applied. During this power step, approximately 17~18 l/min mass flow rate was passed through bundle-04. A possible reason can be mass flow rate inside tube-12 and tube-16 can keep the tube temperature inside tube-12 & tube-16 at 200 kW. While the power step was increased to 250 kW but the total mass flow rate was decreased to 16~16.8 l/min, which caused the tube temperature of tube-12 & tube-16 to oscillate.

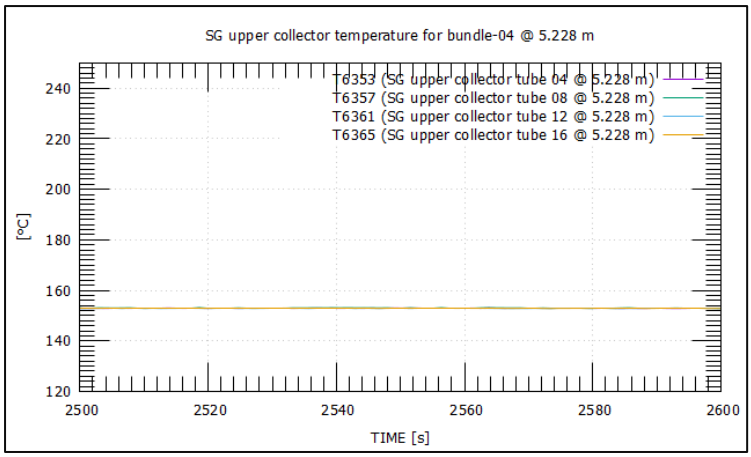

Figure 88:Tube temperature for bundle-04 at 5.228 m after 50 kW power step

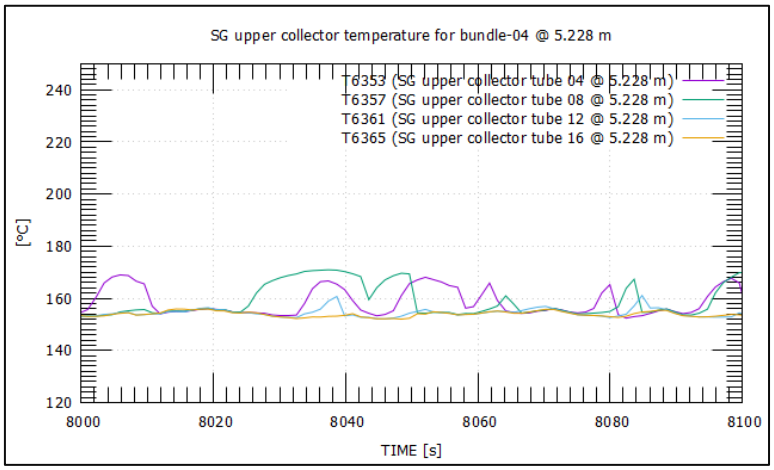

Figure 89: Tube temperature for bundle-04 at 5.228 m after 150 kW power step

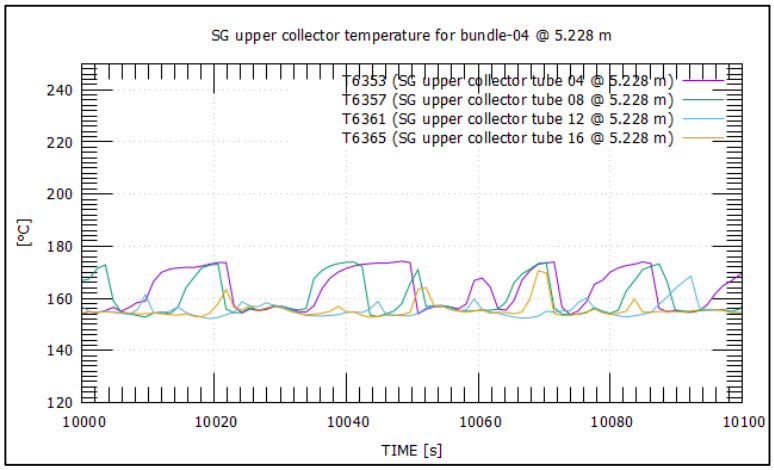

Figure 90: Tube temperature for bundle-04 at 5.228 m after 200 kW power step

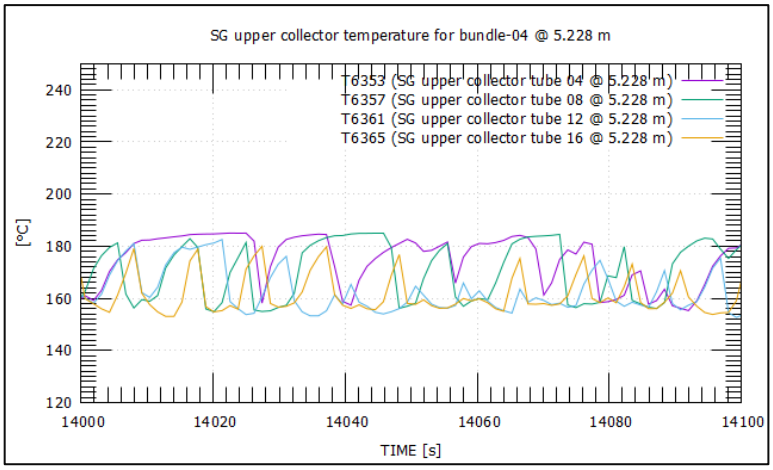

Figure 91: Tube temperature for bundle-04 at 5.228 m after 250 kW power step

5.2 COMPARISON OF CALCULATED AND EXPERIMENTAL OVERALL HEAT TRANSFER COEFFICIENT

In section 4.3.3 procedure to calculate the overall heat transfer coefficient both theoretically and experimentally is discussed. For the estimation of the tube side heat transfer coefficient, Chen, Scrock, and Grossman correlation is used, and the shell side heat transfer coefficient is calculated from wall temperature and primary side fluid temperature. As wall temperature data is missing and not recorded iterative procedure is adopted to calculate wall temperature. From the tube side and shell side heat transfer coefficient, the overall heat transfer coefficient can be calculated using the radial heat transfer formula. For calculating the overall heat transfer coefficient experimentally, primary side fluid temperature and bulk tube side temperature are used. The primary side temperature is calculated using the Average of all measured temperatures at the primary side.

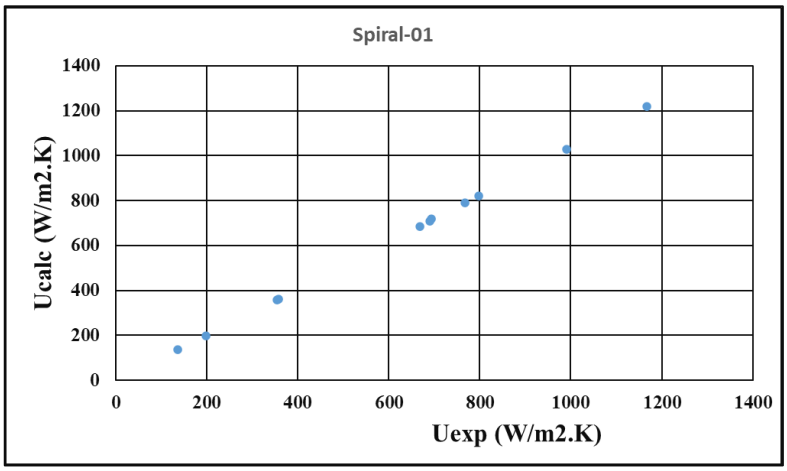

Figure 92: Calculated vs. Experimental overall heat transfer coefficient for Spiral-01

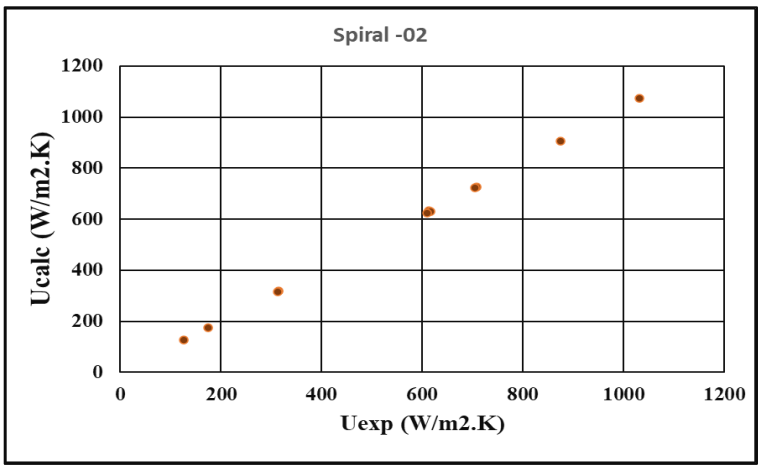

Figure 93: Calculated vs Experimental overall heat transfer coefficient for Spiral-02

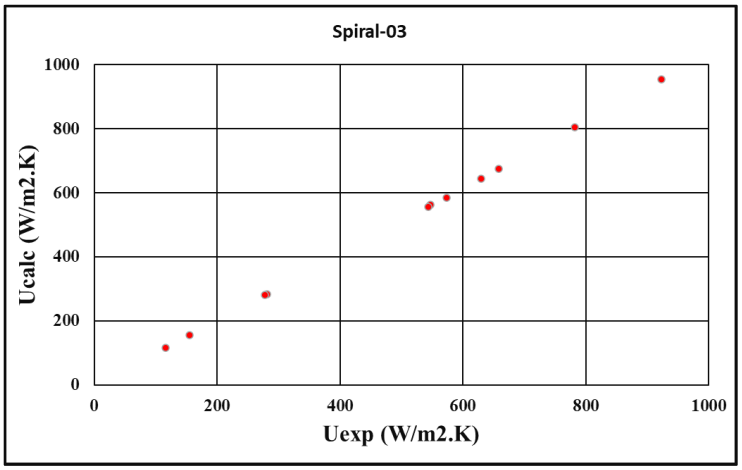

Figure 94: Calculated vs. Experimental overall heat transfer coefficient for Spiral-03

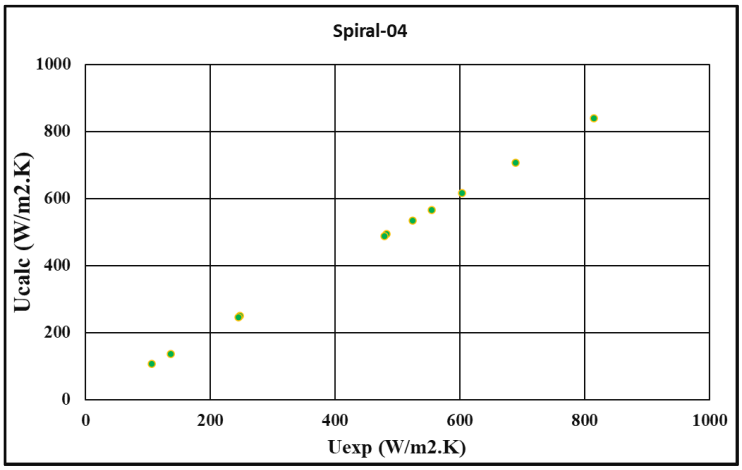

Figure 95: Calculated vs. Experimental overall heat transfer coefficient for Spiral-04

Calculated and experimental overall heat transfer coefficient is mentioned and compared in same graph is for different spiral groups. From the graph, it is evident that the maximum overall heat transfer coefficient for spiral group-01 is around 1200 W/m^2. K this tends to decrease with the increase of spiral group number. Normally heat transfer coefficient is inversely proportional to the heat transfer area, and the heat transfer area is a strong function of length. As spiral group-01 has a lower heat transfer area due to its shorter length, the overall heat transfer coefficient is higher than the rest of the spiral groups. From the graph, it is evident that the correlation used for calculating overall heat transfer coefficient can well predict experimental heat transfer coefficient.

5.3 CALCULATION OF DIMENSIONLESS PARAMETERS FOR FLOW INSIDE HELICAL COILED TUBE

Based on equations (4) & (5) mentioned above, different geometrical parameters for the estimation of dimensionless curvature and torsion are listed below in the tabular format

Table 4: Geometrical parameters for estimating dimensionless curvature and torsion

	Spiral Group-01	Spiral Group-02	Spiral Group-03	Spiral Group-04
Coiled diameter (m), D	0.52	0.56	0.61	0.65
Tube Length (m),L	20	21.70	23.40	25.10
Tube Outer Diameter (m), d	1.50E-02	1.50E-02	1.50E-02	1.50E-02
Tube-to-coil diameter ratio (d/D)	2.91E-02	2.68E-02	2.48E-02	2.31E-02
Number of turns (N)	12.36	12.33	12.31	12.29
Height of Coil (m), H	1.31	1.31	1.31	1.31
Pitch (m), Ps	9.11E-02	9.13E-02	9.15E-02	9.17E-02
Coil Curvature Radius, Rc	8.34E-03	8.28E-03	8.22E-03	8.17E-03

Different authors reported different correlations for the estimation of dimensionless curvature and torsion as expressed by equations (1), (2), and (3). The calculated value of dimensionless curvature and torsion according to different equations proposed by earlier authors are listed below

Table 5: Dimensionless torsion and curvature for different spiral groups

	Spiral Group-01	Spiral Group-02	Spiral Group-03	Spiral Group-04	Author Name
Dimensionless curvature, λ	0.24	0.27	0.29	0.31	Germano, 1982; Huttl and Friedrich, 2000
	0.03	0.01	0.01	0.01	Yamamoto et al.(1995):
	0.03	0.03	0.02	0.02	Di Piazza and Ciofalo (2010)
Dimensionless torsion, δ	0.33	0.31	0.29	0.27	Germano, 1982; Huttl and Friedrich, 2000
	0.01	0.01	0.01	0.01	Yamamoto et al.(1995):
	0.35	0.33	0.30	0.28	Di Piazza and Ciofalo (2010)

Table 6 Critical Reynold Number for different spiral groups

	Spiral Group-01	Spiral Group-02	Spiral Group-03	Spiral Group-04	Author Name
Critical Reynolds Number	6450.61	6279.99	6126.57	5987.52	Ito (1959)
	6276.03	6171.76	6077.09	5990.51	Kubair and Kuloor (1966)
	6328.60	6179.56	6046.95	5927.91	Schmidt (1967)
	6400.73	6224.32	6067.97	5928.15	Srinivasan et al. (1968)
	19486.57	19535.27	19577.32	19614.01	El-Genk and Schriener (2017)

5.4 SEMI-EMPIRICAL CORRELATION FOR PREDICTION OF DENSITY WAVE OSCILLATION ONSET INSIDE HELICAL COILED TUBE

Several authors previously studied two-phase density wave oscillation inside parallel channels both experimentally and analytically. Due to helically coiled steam generator application for small modular reactor study of two-phase boiling instabilities inside helically coiled tube recently has gained interest. Reyes (Reyes, 2019) studied the onset of density wave oscillation phenomena for NuScale Power helical coil steam generator using SIET Laboratories in Piacenza, Italy, and proposed a semi-empirical correlation that assumes liquid bridging inside the boiling length of the tube and is based on steady-state momentum balance performed on the density front using a separate cylinder model. They formed a stability map based on experimental data from the facility. They concluded that the best-fitted model clearly separated unstable and stable regions in the stability map. They proposed two correlations for all test points with vapor quality greater than 0.18.

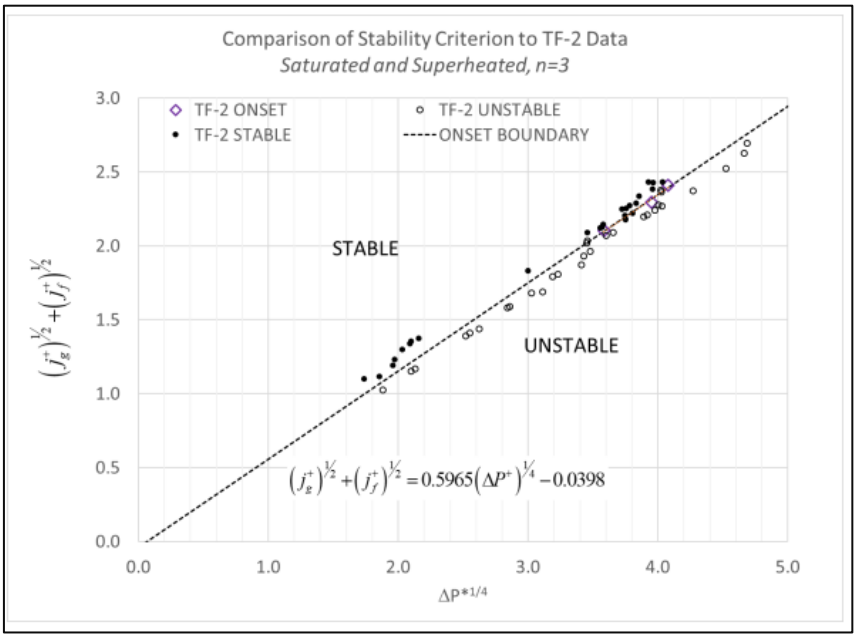

Figure 96: DWO Stability Map for SIET Facility, Italy (Reyes, 2019)

Summation of the square root of dimensionless volumetric flux for gas ($j_{g)}^+$ and liquid (j_l^+) vs. dimensionless pressure drop (ΔP^+) shows the separation of a stable and unstable region. Some experimental data that fall into line indicate the onset of density wave oscillations. To understand the flow condition inside the helically coiled tube for the MOTEL facility similar

type of plot is drawn using experimental data. For comparison purposes, data from the stability test, as reported by Reyes (Reyes, 2019) is also included in the graph.

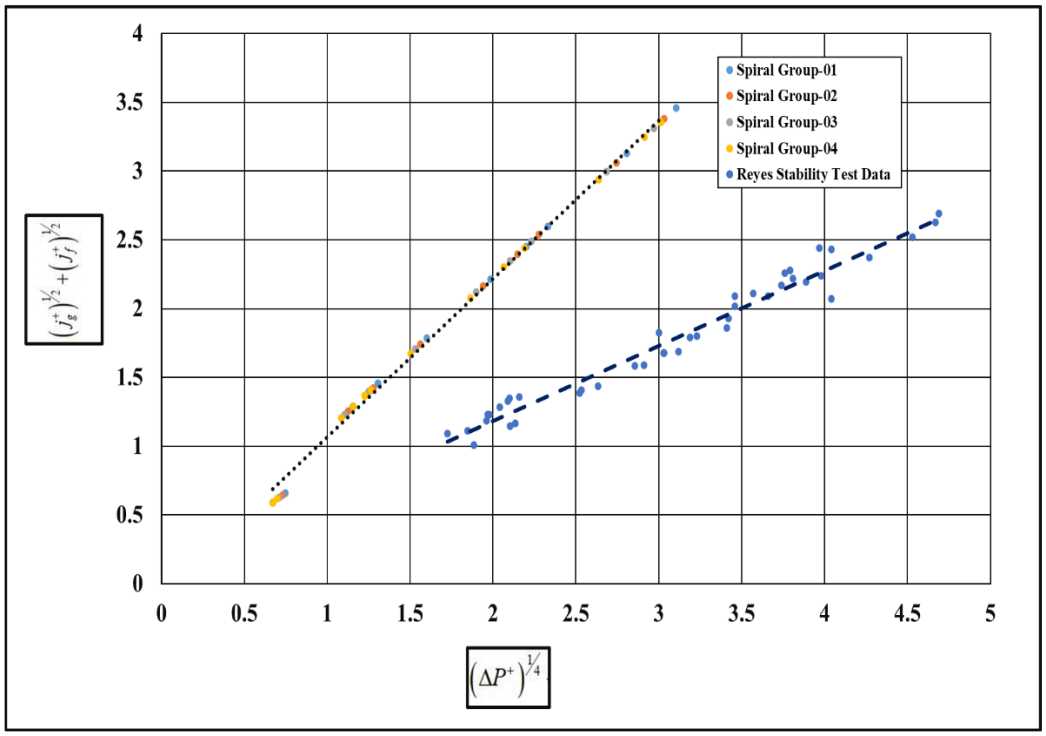

Figure 97: Stability Map for MOTEL Facility

From Figure-97, it is evident that all experimental data as recorded from MOTEL facility lies in the stable region of the graph if compared with Figure-96 though experimental data showed oscillatory behaviour. Reyes reported unstable conditions due to density wave oscillation inside helical coil tubes for their experiment, while other types of instabilities are present for MOTEL test data. For Reyes's experiment, they used a single helical coil tube with no presence of a pressurizer or electrically heated core, while MOTEL facility represents a much more complicated scenario happening inside the helical tube. Figure 97 clearly shows that only density wave oscillation cannot cause instability for MOTEL facility and hence needs further investigation. Based on experiments performed at MOTEL facility, a simple correlation can be developed, which is shown below

$$\left(j_g^+\right)^{1/2}+\left(j_f^+\right)^{1/2}=1.152\left(\Delta P^+\right)^{1/4}-0.0873 \qquad (37)$$

For MOTEL test facility, helical coil tubes with different lengths and coil diameters are used. Tube with the same length and coil diameter belongs to the same spiral group. From Figure 97, it is evident that all spiral group experimental data always lies in the stability region, as

mentioned by Reyes (Reyes, 2019). It can be concluded that to ensure stability, coil diameter and tube length do not play a major role in case only density wave oscillations are present inside the helical tube. But as discussed in the earlier section from MOTEL test data, it was found that oscillation amplitude is a strong function of tube length, and hence in the presence of other type instabilities, differences in tube length can play a major role.

6 CONCLUSIONS

6.1 SUMMARY

The main objective of this thesis is to study boiling instabilities inside the helical coil steam generator used in a small modular reactor. To study how boiling instability happens inside the steam generator tube, system temperature and pressure change due to thermal power are studied. The overall heat transfer coefficient is compared for both experimental and theoretical value.

The following summaries can be drawn from the experimental data analysis and associated research work under this thesis

1. To ensure stability inside the tube, it is important to consider the effect of both thermal energy and mass flow rate. Experimental data showed instability or thermal oscillation increases with the increase of power step. Oscillation amplitude is a strong function of the power step.
2. For tubes with the same diameter but different lengths under the same bundle, the thermal oscillation pattern is also different. The tube with the highest length showed oscillation with the highest amplitude compared to other tubes.
3. A higher mass flow rate tends to increase the stability of tube temperature. When the same power step but a higher mass flow rate was applied during the experiment, it made the system stable, and the oscillation amplitude decreased.
4. The temperature at the inlet region (near the cold collector at 3.423 m) showed the highest fluctuation for most cases in comparison to other regions.
5. The oscillation period is also a strong function of the power step. When a higher power step was applied during the experiment, it also increased the oscillation period for most of the cases.
6. The level inside the secondary tube bundle can also affect how thermal oscillation happens. When the level inside the tube fluctuates, thermal oscillation also seems to fluctuate in the same manner.

6.2 RECOMMENDATIONS FOR FUTURE WORK

The following recommendations can be provided to extend the research work of this thesis

1. Detailed numerical calculation for estimation of mass flow inside the different helical coiled tubes. Several earlier studies (both experimental and numerical) were carried out to calculate flow rate maldistribution inside parallel evaporating channels (Minzer, Barnea and Taitel, 2006; Baikin, Taitel, and Barnea, 2011; Ma, Li, and Wu, 2014; Zhang, Hu and Bi, 2022). Estimation of flow rate distribution accurately through numerical and experimental procedures can help to understand how two-phase mass flow inside parallel helical tubes can affect boiling instabilities.
2. A detailed test matrix with a combination of different mass fluxes, pressure, and inlet subcooling can help to form a more detailed stability map, as carried out in some earlier studies (Papini *et al.*, 2014).
3. Only one correlation is used to estimate the overall heat transfer coefficient theoretically. Moreover, the pressure drop is not estimated as part of this thesis study. Earlier studies (Chen, 1982; Santini *et al.*, 2008; Cioncolini and Santini, 2016; Ferraris and Marcel, 2020; Onal *et al.*, 2022) listed several pressure drop correlations for estimation of pressure drop inside helically coiled tubes. Several heat transfer and pressure drop correlations can be used to check the validity and suitability range of different correlations and hence find the best correlation which can be used as a guideline for any heat transfer and pressure drop study in the near future.

REFERENCES

Advances in Small Modular Reactor Technology Developments (2020), p. 354. Available at: https://aris.iaea.org/Publications/SMR_Book_2020.pdf.

Agency, I.E. (no date) *Executive summary – World Energy Outlook 2021 – Analysis*. Available at: https://www.iea.org/reports/world-energy-outlook-2021/executive-summary (Accessed: 29 August 2022).

Andrzejczyk, R. and Muszynski, T. (2017) 'Thermodynamic and geometrical characteristics of mixed convection heat transfer in the shell and coil tube heat exchanger with baffles', *Applied Thermal Engineering*, 121, pp. 115–125. Available at: https://doi.org/10.1016/j.applthermaleng.2017.04.053.

Baikin, M., Taitel, Y. and Barnea, D. (2011) 'Flow rate distribution in parallel heated pipes', *International Journal of Heat and Mass Transfer*, 54(19–20), pp. 4448–4457. Available at: https://doi.org/10.1016/j.ijheatmasstransfer.2011.04.034.

Bi, Q. *et al.* (1996) 'Frictional pressure drop of steam-water two-phase flow in helical coils with small helix diameter of HTR-10', *Chinese Journal of Nuclear Science and Engineering*, 16(3), pp. 208–213, 283.

Chen, J.C. (1966) 'Correlation for Boiling Heat Transfer to Saturated Fluids in Convective Flow', *Industrial & Engineering Chemistry Process Design and Development*, 5(3), pp. 322–329. Available at: https://doi.org/10.1021/i260019a023.

Chen, L. (1982) 'Steam-water two-phase flow frictional pressure drop in straight tubes', *Selected papers of multiphase flow and heat transfer, Paper*, 7, p. 7.1-7.6.

Chisholm, D. (1967) 'A theoretical basis for the Lockhart-Martinelli correlation for two-phase flow', *International Journal of Heat and Mass Transfer*, 10(12), pp. 1767–1778.

Chung, Y.-J. *et al.* (2014a) 'Boiling heat transfer and dryout in helically coiled tubes under different pressure conditions', *Annals of Nuclear Energy*, 71, pp. 298–303. Available at: https://doi.org/10.1016/j.anucene.2014.04.015.

Chung, Y.-J. *et al.* (2014b) 'Boiling heat transfer and dryout in helically coiled tubes under different pressure conditions', *Annals of Nuclear Energy*, 71, pp. 298–303. Available at: https://doi.org/10.1016/j.anucene.2014.04.015.

Cioncolini, A. and Santini, L. (2016) 'Two-phase pressure drop prediction in helically coiled steam generators for nuclear power applications', *International Journal of Heat and Mass Transfer*, 100, pp. 825–834. Available at: https://doi.org/10.1016/j.ijheatmasstransfer.2016.05.027.

Colombo, M. *et al.* (2011) *Experimental investigation of thermal hydraulic instabilities in Steam Generator helical coil tubes*. Milan, Italy: ENEA, p. 56.

Crain Jr, B. (1973) *FORCED CONVECTION HEAT TRANSFER TO A TWO-PHASE MIXTURE OF WATER AND STEAM IN A HELICAL COIL*. Oklahoma State University.

Ferraris, D.L. and Marcel, C.P. (2020) 'Two-phase flow frictional pressure drop prediction in helical coiled tubes', *International Journal of Heat and Mass Transfer*, 162, p. 120372. Available at: https://doi.org/10.1016/j.ijheatmasstransfer.2020.120372.

Fsadni, A.M. and Whitty, J.P.M. (2016a) 'A review on the two-phase heat transfer characteristics in helically coiled tube heat exchangers', *International Journal of Heat and Mass Transfer*, 95, pp. 551–565. Available at: https://doi.org/10.1016/j.ijheatmasstransfer.2015.12.034.

Fsadni, A.M. and Whitty, J.P.M. (2016b) 'A review on the two-phase pressure drop characteristics in helically coiled tubes', *Applied Thermal Engineering*, 103, pp. 616–638. Available at: https://doi.org/10.1016/j.applthermaleng.2016.04.125.

Genić, S.B. *et al.* (2012) 'Research on the shell-side thermal performances of heat exchangers with helical tube coils', *International Journal of Heat and Mass Transfer*, 55(15), pp. 4295–4300. Available at: https://doi.org/10.1016/j.ijheatmasstransfer.2012.03.074.

Ghasemian, S. *et al.* (2020) 'An overview of global energy scenarios by 2040: identifying the driving forces using cross-impact analysis method', *International Journal of Environmental Science and Technology* [Preprint]. Available at: https://doi.org/10.1007/s13762-020-02738-5.

Gou, J. *et al.* (2017) 'An assessment of heat transfer models of water flow in helically coiled tubes based on selected experimental datasets', *Annals of Nuclear Energy*, 110, pp. 648–667.

Guo, L., Feng, Z. and Chen, X. (2001) 'An experimental investigation of the frictional pressure drop of steam–water two-phase flow in helical coils', *International journal of heat and mass transfer*, 44(14), pp. 2601–2610.

Hwang, K.W. *et al.* (2014) 'Experimental study of flow boiling heat transfer and dryout characteristics at low mass flux in helically-coiled tubes', *Nuclear Engineering and Design*, 273, pp. 529–541. Available at: https://doi.org/10.1016/j.nucengdes.2014.03.046.

Hyvärinen, J., Telkkä, J. and Tielinen, K. (2022) 'MOTEL-SMR INTEGRAL PWR SYSTEM TEST FACILITY -DESIGN AND FIRST TEST RESULTS', in. *The 19th International Topical Meeting on Nuclear Reactor Thermal Hydraulics (NURETH-19)*, Brussels, Belgium.

IAEA PRIS (2022) *IAEA PRIS*. Available at: https://pris.iaea.org/PRIS/WorldStatistics/UnderConstructionReactorsByCountry.aspx (Accessed: 3 September 2022).

Kakac, S. and Bon, B. (2008) 'A Review of two-phase flow dynamic instabilities in tube boiling systems', *International Journal of Heat and Mass Transfer*, 51(3–4), pp. 399–433. Available at: https://doi.org/10.1016/j.ijheatmasstransfer.2007.09.026.

Kessides, I.N. and Kuznetsov, V. (2012) ‘Small Modular Reactors for Enhancing Energy Security in Developing Countries’, *Sustainability*, 4(8), pp. 1806–1832. Available at: https://doi.org/10.3390/su4081806.

Kozeki, M. *et al.* (1970) ‘A study of helically-coiled tube once-through steam generator’, *Bulletin of JSME*, 13(66), pp. 1485–1494.

Lee, S. and Hassan, Y.A. (2022) ‘Flow structures of the cross-flow over a five-layer helically coiled steam generator geometry’, *International Journal of Heat and Fluid Flow*, 95, p. 108950. Available at: https://doi.org/10.1016/j.ijheatfluidflow.2022.108950.

Ligrani, P.M. (1994) *A Study of Dean Vortex Development and Structure in a Curved Rectangular Channel with Aspect Ratio of 40 at Dean Numbers up to 430*. E-8918. Available at: https://ntrs.nasa.gov/citations/19950005258 (Accessed: 10 September 2022).

Lu, X. *et al.* (2014) ‘Shell-side thermal-hydraulic performances of multilayer spiral-wound heat exchangers under different wall thermal boundary conditions’, *Applied Thermal Engineering*, 70(2), pp. 1216–1227. Available at: https://doi.org/10.1016/j.applthermaleng.2014.02.053.

Ma, Y., Li, X. and Wu, X. (2014) ‘Thermal–hydraulic characteristics and flow instability analysis of an HTGR helical tube steam generator’, *Annals of Nuclear Energy*, 73, pp. 484–495. Available at: https://doi.org/10.1016/j.anucene.2014.07.031.

‘McKinsey & Company.pdf’ (no date).

Minzer, U., Barnea, D. and Taitel, Y. (2006) ‘Flow rate distribution in evaporating parallel pipes—modeling and experimental’, *Chemical Engineering Science*, 61(22), pp. 7249–7259. Available at: https://doi.org/10.1016/j.ces.2006.08.026.

Mirgolbabaei, H. (2018) ‘Numerical investigation of vertical helically coiled tube heat exchangers thermal performance’, *Applied Thermal Engineering*, 136, pp. 252–259. Available at: https://doi.org/10.1016/j.applthermaleng.2018.02.061.

Nariai, H., Kobayashi, M. and Matsuoka, T. (1982) ‘Friction Pressure Drop and Heat Transfer Coefficient of Two-Phase Flow in Helically Coiled Tube Once-Through Steam Generator for Integrated Type Marine Water Reactor’, *Journal of Nuclear Science and Technology*, 19(11), pp. 936–947. Available at: https://doi.org/10.1080/18811248.1982.9734239.

Niemi, M. (2017) *Simulation and Safety features of NuScale Small Modular Reac- tor*. Aalto University. Available at: https://aaltodoc.aalto.fi/handle/123456789/29299 (Accessed: 3 September 2022).

Nuclear Power in the World Today (2022) *World Nuclear Association*. Available at: https://www.world-nuclear.org/information-library/current-and-future-generation/nuclear-power-in-the-world-today.aspx#:~:text=Nuclear%20energy%20now%20provides%20about,in%20about%20220%20research%20reactors. (Accessed: 3 September 2022).

Onal, B.S. *et al.* (2022) 'Heat transfer and pressure drop characteristics of two phase flow in helical coils', *Thermal Science and Engineering Progress*, 27, p. 101143. Available at: https://doi.org/10.1016/j.tsep.2021.101143.

Owhadi, A., Bell, J. and Crain, B. (1968) 'FORCED CONVECTION BOILING INSIDE HELICALLY-COILED TUBES', *Int. J. Heat Mass Transfer*, 11, pp. 1779–1793.

Owhadi, A., Bell, K.J. and Crain Jr, B. (1968) 'Forced convection boiling inside helically-coiled tubes', *International Journal of Heat and Mass Transfer*, 11(12), pp. 1779–1793.

Papini, D. *et al.* (2014) 'Experimental and theoretical studies on density wave instabilities in helically coiled tubes', *International Journal of Heat and Mass Transfer*, 68, pp. 343–356. Available at: https://doi.org/10.1016/j.ijheatmasstransfer.2013.09.035.

Reyes, J.N. (2019) 'A SEMI-EMPIRICAL CORRELATION FOR THE ONSET OF DENSITY WAVE OSCILLATIONS IN A HELICAL COIL STEAM GENERATOR', in. *NURETH 2019*, p. 14.

Ricotti, M.E., Cammi, D.A. and Colombo, D.L. (2013) *Experimental Investigation and Numerical Simulation of the Two-Phase Flow in the Helical Coil Steam Generator*. Politecnico Di Milano.

Santini, L. *et al.* (2008) 'Two-phase pressure drops in a helically coiled steam generator', *International Journal of Heat and Mass Transfer*, 51(19), pp. 4926–4939. Available at: https://doi.org/10.1016/j.ijheatmasstransfer.2008.02.034.

Schrock, V.E. and Grossman, L.M. (1962) 'Forced Convection Boiling in Tubes', *Nuclear Science and Engineering*, 12(4), pp. 474–481. Available at: https://doi.org/10.13182/NSE62-A26094.

'SPECK TRIPLEX' (2022). SPECK TRIPLEX. Available at: https://www.speck-triplex.de/index.php?option=com_joodb&task=getFileFrom-Blob&joobase=9&id=39&field=pdf (Accessed: 15 September 2022).

Steiner, D. and Taborek, J. (1992) 'Flow Boiling Heat Transfer in Vertical Tubes Correlated by an Asymptotic Model', *Heat Transfer Engineering*, 13(2), pp. 43–69. Available at: https://doi.org/10.1080/01457639208939774.

Telkkä, J. and Karppinen, J. (2018) *Modular Test Loop (MOTEL)*. INFRAL 1/2018. Lappeenranta: LUT University, p. 18.

Tielinen, K. *et al.* (2021) *MOTEL facility description*. Lappeenranta: LUT University, p. 40.

Todreas, N.E. and Kazimi, M.S. (2001) *NUCLEAR SYSTEMS II Elements of Thermal Hydraulic Design*. Taylor and Francis.

Tuncer, A.D. *et al.* (2021) 'Upgrading the performance of a new shell and helically coiled heat exchanger by using longitudinal fins', *Applied Thermal Engineering*, 191, p. 116876. Available at: https://doi.org/10.1016/j.applthermaleng.2021.116876.

Ugueto, L. (2013) *Experimental study of density waves oscillations*. Norwegian University of Science and Technology (NTNU).

Vashisth, S., Kumar, V. and Nigam, K.D.P. (2008) 'A Review on the Potential Applications of Curved Geometries in Process Industry', *Industrial & Engineering Chemistry Research*, 47(10), pp. 3291–3337. Available at: https://doi.org/10.1021/ie701760h.

Vishvakarma, S., Kumbhare, S. and Thakur, K.K. (2016) 'A REVIEW ON HEAT TRANSFER THROUGH HELICAL COIL HEAT EXCHANGERS', *International Journal of Engineering Sciences*, p. 6. Available at: https://doi.org/10.5281/zenodo.60105.

Zhang, L., Hu, G. and Bi, X.T. (2022) 'Two-phase flow in parallel channels: Mal-distribution, hysteresis and mitigation strategies', *Chemical Engineering Science*, 247, p. 117044. Available at: https://doi.org/10.1016/j.ces.2021.117044.

Zhao, L. *et al.* (2003a) 'Convective boiling heat transfer and two-phase flow characteristics inside a small horizontal helically coiled tubing once-through steam generator', *International journal of heat and mass transfer*, 46(25), pp. 4779–4788.

Zhao, L. *et al.* (2003b) 'Convective boiling heat transfer and two-phase flow characteristics inside a small horizontal helically coiled tubing once-through steam generator', *International Journal of Heat and Mass Transfer*, 46(25), pp. 4779–4788. Available at: https://doi.org/10.1016/S0017-9310(03)00354-5.

APPENDIX-I

Table 7: MS-SG02 Power Level and Operation

Start time (s)	End time (s)	Power level/operation
0	3600	75 kW
3600	7200	100
7200	10800	125
10800	14400	150
14400	15000	150, secondary side flow reduction 10 kW
15000	15600	150, secondary side flow reduction 20 kW
15600	16000	150, secondary side flow reduction 30 kW
16000	16400	150, secondary side flow reduction 40 kW
16400	17400	150, secondary side flow reduction 30 kW
17400	17523	100, secondary side flow reduction 20 kW
17523	18400	100, secondary side flow reduction 15 kW

Table 8: MS-SG0R Power Level and Operation

Start time (s)	End time (s)	Power level/operation
0	-	Experiment begins
1500	2600	250 kW
2600	5100	Secondary feedwater flow adjustment
5100	8700	500 kW
-	8700	Experiment ends

Table 9: MS-SG01A Power Level and Operation

Start time (s)	End time (s)	Power level/operation
0	-	Experiment begins
100	1390	750 kW
1390	3700s	secondary side pressure control valve settings
-	3700	Experiment ends

Table 10: MS-SG01B Power Level and Operation

Start time (s)	End time (s)	Power level/operation
0	-	Experiment begins
0	400	Power adjusted to 1 MW in few steps
400	4000	1 MW reached
-	4000	Experiment ends

Table 11: MS-SG03 Power Level and Operation

Start time (s)	End time (s)	Power level/operation
300	3300	50 kW
3300	6300	100 kW
6300	6700	Primary level reduction
6700	9700	150 kW
9700	12700	200 kW
12700	16000	250 kW

Table 12:Temperature Measurement of steam generator cold collector

Measurement Code	Location	Spiral Group Number	Bundle Number
T6280	SG cold collector tube 01	04	01
T6281	SG cold collector tube 02		02
T6282	SG cold collector tube 03		03
T6283	SG cold collector tube 04		04
T6284	SG cold collector tube 05	03	01
T6285	SG cold collector tube 06		02
T6286	SG cold collector tube 07		03
T6287	SG cold collector tube 08		04
T6288	SG cold collector tube 09	02	01
T6289	SG cold collector tube 10		02
T6290	SG cold collector tube 11		03
T6291	SG cold collector tube 12		04
T6292	SG cold collector tube 13	01	01
T6293	SG cold collector tube 14		02
T6294	SG cold collector tube 15		03
T6295	SG cold collector tube 16		04

Table 13:Temperature Measurement of Steam Generator tube bottom

Measurement Code	Location	Spiral Group Number	Bundle Number
T6300	SG tube 01 bottom	04	01
T6301	SG tube 02 bottom		02
T6302	SG tube 03 bottom		03
T6303	SG tube 04 bottom		04
T6304	SG tube 05 bottom	03	01
T6305	SG tube 06 bottom		02
T6307	SG tube 08 bottom		04
T6308	SG tube 09 bottom	02	01
T6309	SG tube 10 bottom		02
T6310	SG tube 11 bottom		03
T6311	SG tube 12 bottom		04
T6312	SG tube 13 bottom	01	01
T6313	SG tube 14 bottom		02
T6314	SG tube 15 bottom		03
T6315	SG tube 16 bottom		04

Table 14:Temperature Measurement of Steam Generator tube middle

Measurement Code	Location	Spiral Group Number	Bundle Number
T6316	SG tube 01 middle	04	01
T6317	SG tube 02 middle		02
T6318	SG tube 03 middle		03
T6319	SG tube 04 middle		04
T6320	SG tube 05 middle	03	01
T6321	SG tube 06 middle		02
T6322	SG tube 07 middle		03
T6323	SG tube 08 middle		04
T6324	SG tube 09 middle	02	01
T6325	SG tube 10 middle		02
T6326	SG tube 11 middle		03
T6327	SG tube 12 middle		04
T6328	SG tube 13 middle	01	01
T6329	SG tube 14 middle		02
T6330	SG tube 15 middle		03
T6331	SG tube 16 midde		04

Table 15:Temperature Measurement of Steam Generator tube top

Measurement Code	Location	Spiral Group Number	Bundle Number
T6332	SG tube 01 top	04	01
T6333	SG tube 02 top		02
T6334	SG tube 03 top		03
T6335	SG tube 04 top		04
T6336	SG tube 05 top	03	01
T6337	SG tube 06 top		02
T6338	SG tube 07 top		03
T6339	SG tube 08 top		04
T6340	SG tube 09 top	02	01
T6341	SG tube 10 top		02
T6342	SG tube 11 top		03
T6343	SG tube 12 top		04
T6344	SG tube 13 top	01	01
T6345	SG tube 14 top		02
T6346	SG tube 15 top		03
T6347	SG tube 16 top		04

Table 16:Temperature Measurement of Steam Generator hot collector

Measurement Code	Location	Spiral Group Number	Bundle Number
T6350	SG hot collector tube 01	04	01
T6351	SG hot collector tube 02		02
T6352	SG hot collector tube 03		03
T6353	SG hot collector tube 04		04
T6354	SG hot collector tube 05	03	01
T6355	SG hot collector tube 06		02
T6356	SG hot collector tube 07		03
T6357	SG hot collector tube 08		04
T6358	SG hot collector tube 09	02	01
T6359	SG hot collector tube 10		02
T6360	SG hot collector tube 11		03
T6361	SG hot collector tube 12		04
T6362	SG hot collector tube 13	01	01
T6363	SG hot collector tube 14		02
T6364	SG hot collector tube 15		03
T6365	SG hot collector tube 16		04

Table 17:Temperature Measurement of Steam Generator primary side

Measurement Code	Location
T6004	Steam generator 205°, primary side
T6005	Steam generator 345°, primary side
T6006	Steam generator 205°, primary side
T6007	Steam generator 345°, primary side
T6008	Steam generator 205°, primary side
T6009	Steam generator 345°, primary side
T6010	Steam generator 205°, primary side
T6011	Steam generator 345°, primary side
T6012	Steam generator 205°, primary side
T6013	Steam generator 345°, primary side

Table 18:Pressure Measurement of Steam Generator

Measurement Code	Location
P6000	Primary side
P6001	Secondary side, steam manifold
P6002	Volume Control pump
P6003	Secondary Feedwater pump

Table 19: Flow Rate Measurement for Steam Generator

Measurement Code	Location
F6003	Secondary feedwater flow